THE UNIVERSITY *of* EDINBURGH

Novel droplet ripening behaviour in ternary oil-alcohol-water systems

Javier Otero Márquez

Doctor of Philosophy
The University of Edinburgh
May 2019

Abstract

An ever increasing interest in reducing costs and the energy impact of different manufacturing processes is one of the main drives in industrial fields such as the food and pharmaceutical sectors. In these fields, often at least one of the manufacturing stages will be some form of emulsification, thus the interest in researching into spontaneous emulsification, where emulsions can be formed without adding external energy. In this thesis three different systems in which spontaneous emulsification occurs have been studied, focusing on some of the special features each one presents.

The first system we have studied is composed of a bath, made of toluene and ethanol with added silica particles, into which two aqueous droplets are injected. If there is an alcohol concentration difference between the drops, spontaneous formation of small droplets, from the the less alcohol-rich drop all along the path towards the ethanol-enriched drop, will occur until a complete "bridge" is formed. This behaviour has been related graphically to the diffusion paths on the underlying three-fluid phase diagram, arguing that compositional ripening is the reason for the mass transfer. Different experimental techniques were employed to characterize the spontaneously formed droplets.

By switching the alcohol present in the previous system to methanol we have obtained a more dynamic system with more extensive emulsification. In this system, experiments used only one injected drop and its diffusion behaviour was studied. Several quantitative parameters, such as the relative growth of the drop, how long it takes before it starts to redissolve and when do the spontaneously formed droplets redissolve, have been related to the initial alcohol content inside the drop, using its own ternary phase diagram. Solvatochromic dyes were used on systems with no particles to follow the different diffusion flows, confirming our hypothesis visually.

The last system we have studied is composed of 2,3-dimethylpenthane, 1-propanol, water and Poly(methyl methacrylate) (PMMA) particles. Although its phase diagram is very similar to those of our previous systems, we found that its behaviour is not. Spontaneous emulsification is still present, however, at the surface of the injected Pickering water drop. Additional droplets were found to emerge from these spontaneously formed droplets sitting at the drop's interface. These droplets, although partially covered by particles, and therefore stabilized, evolve over time increasing their size and exhibit coalescence. We have explored its ternary diagram and found that alcohol, even though increased amounts of alcohol destabilize the drops by increasing its miscibility, a small amount is needed for this effect for the same reason. However, if no alcohol is present in the system, fractal dewetting was observed both at the bottom and top of the cuvette where the drop is located. Varying the size of the particles in this system modified the observed patterns, which were characterized by its fractal dimension, obtained through image analysis.

Lay Summary

A lot of everyday foods, such as mayonnaise, salad dressings or butter, are made of small droplets dispersed in a continuous liquid phase. They are called emulsions, and we know from experience that a lot of energy needs to be transmitted, for example via stirring it, to create them. But even then we will notice how they demix after some time. When contacting oil and water, we know that they don't mix unless we shake them vigorously, and even then they demix shortly after. To avoid this, it is common practice in industry to add surfactants, which are molecules that will be situated around the droplets, or tiny particles, such as sand grains, to stabilize the mixture. The more stable the emulsion is, the longer its shelf life will be, making it more desirable for companies.

The manufacturing process to create emulsions requires a large amounts of energy, and a lot of research has been done to improve the efficiency. Spontaneous emulsification is the name of the phenomenon that occurs when emulsions are formed without adding energy (no heating or stirring). In this thesis we have studied systems where this occurs and forms different structures. In Chapter 3 the emulsion formed a structure resembling a bridge connecting two drops, whereas in Chapter 4 the emulsion formed a "cloud" around our drop and even made twirls. More surprisingly, in Chapter 5 we observed the formation of droplets on top of droplets all along the surface of our injected drop. The objective in this thesis has been to understand why all these phenomena occured, and relate them with theory to be able to predict them.

Declaration

I declare that this thesis was composed by myself, that the work contained herein is my own except where explicitly stated otherwise in the text, and that this work has not been submitted for any other degree or professional qualification except as specified.

Parts of the work presented in Chapter 3, where the candidate performed all the experiments and wrote the draft paper, have been published in [1].

(*Javier Otero Márquez, May 2019*)

Acknowledgements

First and foremost, I'd like to thank my supervisor, Paul Clegg, for helping me pull through my doctorate. I'd also like to thank Andrew Schofield for always being available to answer any type of lab question, no matter how dumb they were, and Elena Blanco for helping me with the rheology experiments. I'd also like to acknowledge the help provided by Steven Meeker from Solvay for allowing me to do my secondment with them and obtain valuable results for my research.

Most importantly, I wouldn't be who I am now without my family, which has supported me inconditionally and offered some very needed breaks from the day to day routine.

So long, and thanks for all the fish.

Contents

List of Figures

List of Tables

Chapter 1

Introduction

The work presented in this thesis belongs to the soft matter field, which comprises all those materials (including those called "complex fluids") deformed by thermal fluctuations or mechanical forces with a mesoscopic structural scale. The materials we are interested in are colloids, mixtures of at least two components where one phase is finely dispersed into the other. Each component may be a solid, liquid or gas, except for gas-gas mixtures where they would mix completely. The name for all these possible combinations have been included in Figure 1.1.

If those phases are immiscible liquids, we have an emulsion. Emulsions are thermodynamically unstable, as the interactions between the same type of molecules are energetically preferred over those between different molecules. However, if their interface is stabilized, either by surfactants or particles (which create the so called Pickering emulsions), we can obtain long-lived emulsions.

Scottish botanist Robert Brown [3] observed, although he was unable to explain convincingly, the random movement of pollen grains in suspension. Albert Einstein [4] explained how the pollen was pushed around by the solvent (water) molecules. According to the kinetic theory of gases (Maxwell, Boltzman and Clausius), the temperature is proportional to the average kinetic energy of the molecules, which are always moving or vibrating, and this movement can be transferred to larger particles when they are constantly being "bombarded" by molecules from all sides. An increase in temperature, the number of particles, or a reduction in size or viscosity produce a more lively motion. This type of movement is usually observable in colloids, such as emulsions where its drop size is very small. Those drops would have a low mass, resulting in significant

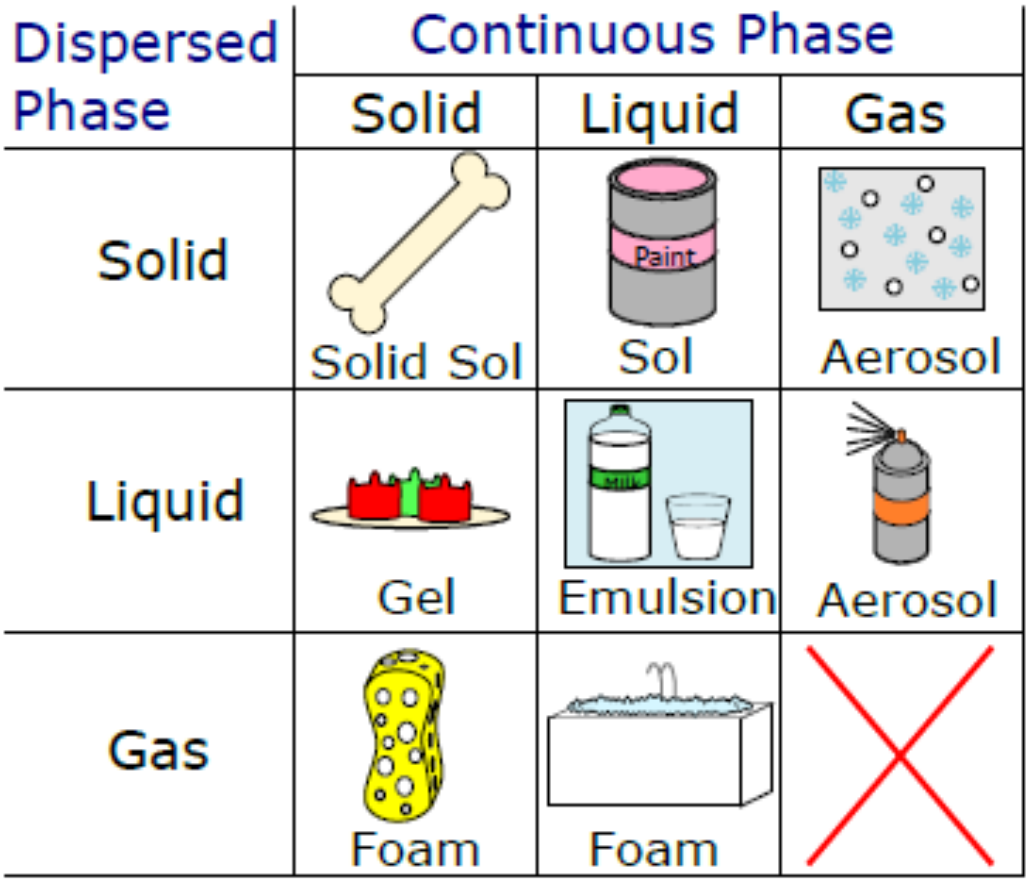

Figure 1.1 *Types of colloids according to the phase of each component. Image taken from [2].*

movement induced by collisions with the solvent's molecules.

It is natural to assume that the random walk a particle does due to the collisions with solvent molecules could change if there is a gradient in the amount, or type, of solvent molecules. This process, called diffusion, can be considered a macroscopic manifestation of Brownian motion. Generally, diffusion is a transport process that occurs from high concentration to low concentration regions due to a gradient in the chemical potential of the diffusing species. Therefore, if we have a non-homogeneous mixture, the different diffusing molecules will move differently according to their environment until an equilibrium is reached, usually when homogeneity is achieved.

Most of the work in the literature, specially last century's, regarding emulsions are based on binary mixtures. The addition of a third component makes it extremely difficult to determine each components' contribution. This is one example where

the huge increase in computational power and the advancement of simulation techniques results in quantitative data difficult to test experimentally. We have tried to relate our experimental observations with the predictions obtained through calculations by the use of diffusion paths plotted in ternary diagrams. Our objective is to be able to make predictions of the diffusion dynamics of ternary systems based on experimental ternary diagrams.

One of the key phenomenon in our systems is spontaneous emulsification, which creates emulsions without using any external energy (such as mechanical agitation or heat transfer). The Ouzo effect is an example of this, where the addition of water to an alcohol/oil mixture changes its appearance, evolving from a clear solution to a cloudy one. This is due to the formation of an emulsion (composed by thousands of tiny droplets) that scatters the light, producing a milky appearance. Figure 1.2 (a) shows the pure Ouzo drink (which is mainly trans-anethol oil) in the left glass, and its change in appearance after being mixed with water (the glass on the right). Figure 1.2 (b) includes the size (black circles) over time of the emulsion droplets, which allows to distinguish between a growth and a stable regime (Fig. 1.2 (b))

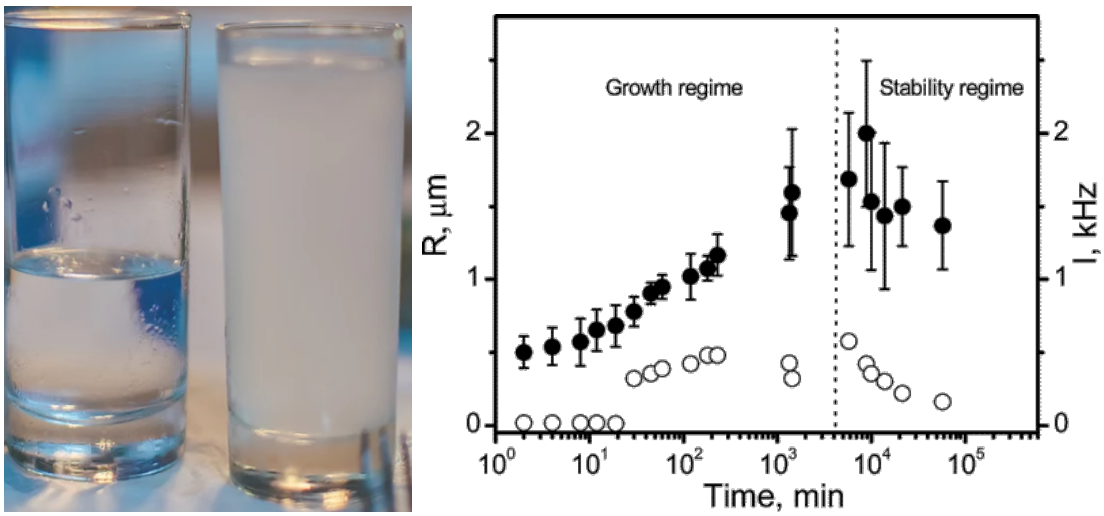

Figure 1.2 *(a) Glass with Ouzo drink before (left) and after (right) mixing it with water. (b) Size (black circles) versus time for emulsion droplets made of 0.04 wt % oil on an ethanol/water mixture of 0.05/0.95 wt %, obtained from [5].*

This effect has created some curious phenomenon that we have tried to understand as thoroughly as possible using a variety of experimental techniques. In Chapter 3 we focused in the bridging phenomenon produced by spontaneously formed water-rich droplets trapped in the bath, whereas Chapter 4 had spontaneously formed droplets as "clouds" around the single-injected drop. These droplets were seen

forming twirls following the Marangoni flow present at the interface when no particles were included. Lastly, Chapter 5 presents spontaneous formation of droplets all across the injected drop interface, with those droplets having spawned droplets on themselves.

Chapter 2

Theoretical background

In order to have a better understanding of the described phenomena in the following chapters, it is necessary to review some concepts. First, we define an emulsion, and how they evolve over time with different types of ripening. Then, we will discuss the effect that particles have when added to an emulsion with the objective of stabilizing it. After this, the main part of this chapter focuses on the most important effect affecting our system, which is also responsible for most of the subsidiary phenomena - spontaneous emulsification. Here we present the most relevant information found and how it will be linked with our experimental findings. Because our hypothesis rely on reading and understanding ternary diagrams and diffusion pathways, we have also included a comprehensive review on their definition and how to read and interpret them. Lastly, some brief remarks about particles at interfaces, compositional and Ostwald ripening, and solvatochromism are also included as they will play a role in this work.

2.1 Emulsions

Emulsions are a type of two-phase systems formed by a dispersed phase and a continuous phase, both in the liquid state. Many fluid pairs that remain miscible at high temperatures form emulsions when quenched. As a rule of thumb, if the phase volume $\Phi_{A,B}$ in a binary mixture of A and B e is $0.3 < \Phi_A < 0.7$ we would observe a bicontinuous structure. If not, we will obtain droplets dispersed in a continuous phase. These droplets will move under Brownian motion and may

collide with other droplets, increasing their mean droplet radius by coalescence. This time evolution of the droplet size may either follow Ostwald ripening if there are size differences in the ensemble, or compositional ripening if there is a chemical imbalance of species.

2.1.1 Ostwald ripening

It has been thoroughly studied and can be observed in almost all phase separation processes at late stages [6–8]. Its driving force is the chemical potential differences induced by pressure differences, related through the Laplace pressure with their size. Therefore, the smaller droplets have a higher pressure than the bigger ones, so they can either redissolve into the bath or fuse with other droplets. Ostwald ripening's rate is dependent on the concentration around droplets, which is also size related as indicated by the Gibbs-Thomson relation.

Ripening inhibitors are substances with high solubility on the dispersed phase (droplets) but insoluble in the continuous phase (bath) that will create an osmotic pressure opposing Ostwald ripening. Experimentally, it has been shown that growth in amorphous drug nanosuspensions, which can multiply its size by 5 in less than an hour due to Ostwald ripening, can be suppressed by adding 10% (w/w) of a mixture of glycerides to the drug [9].

The growth rate follows a different equation depending on whether the limiting process is the diffusion or the attachment/detachment of molecules. In the first case, the volume of large droplets grows linearly with time and in the second case the surface area of the large droplets grows linearly with time. This phenomenon does not create a metastable state, so ultimately it leads to phase separation unless stabilized in some other way, e.g surfactants or particles. In emulsions with surfactants, Ostwald ripening has been proved to be a micelle transport mediated phenomenom, as its rate is linear with the micelle concentration above the critical micelle concentration (cmc), which is the minimum concentration needed to form micelles [10].

To summarize, factors intervening in Ostwald ripening are the droplet size and composition, solubility (inversely proportional to size) and interfacial tension.

2.1.2 Compositional ripening

In this case, its driving force is the gradient in chemical potential due to compositional differences between droplets, which causes the movement of molecules from one to another through a media in which they can dissolve. Concentration differences provoke chemical potential gradients that are much more important than those that originate from Laplace pressure differences. This makes possible to neglect Ostwald ripening in systems with significant compositional ripening [11].

Particles have been used to stabilise emulsions in an effort to suppress compositional ripening [12]. On a system formed by lightly soluble drops (β ionone, which will shrink) and water-insoluble drops (squalane, an immobile oil that will swell) at 4.2% concentration in water, different amounts of fumed silica nanoparticle were added. When the particle concentration is low, coalescence occurs and the squalane droplet radius is proportional to the swelling ratio. However, the behaviour of the system switches to a surfactant-like when there is an excess of particles: no coalescence is observed and the droplet radius becomes proportional to the swelling ratio to the power of 1/3.

A balance between compositional and Ostwald ripening can be attained, allowing droplet sizes to remain stable. In Figure 2.1, a schematic for Ostwald and compositional ripening has been included. Yellow spheres represent droplets, where the small circles represent oil molecules. Ostwald ripening can be observed in Fig. 2.1(a), the difference on size between the two droplets is what drives oil molecules from the left to the right droplet, whereas in Fig. 2.1(b) we observe compositional ripening, where two different type of oils, given by black and white points, modify the chemical potential of the droplet. This difference will induce the movement of molecules in order to make the concentration (chemical potential) in both droplets the same.

2.1.3 Marangoni instability

It is commonly known as the responsible for the everyday phenomenon occurring with drops of wine in a glass. Briefly, what happens in a glass of wine is that alcohol evaporates faster than the aqueous phase, thus creating a higher surface tension area that will pull liquid from the bulk against gravity, creating the so

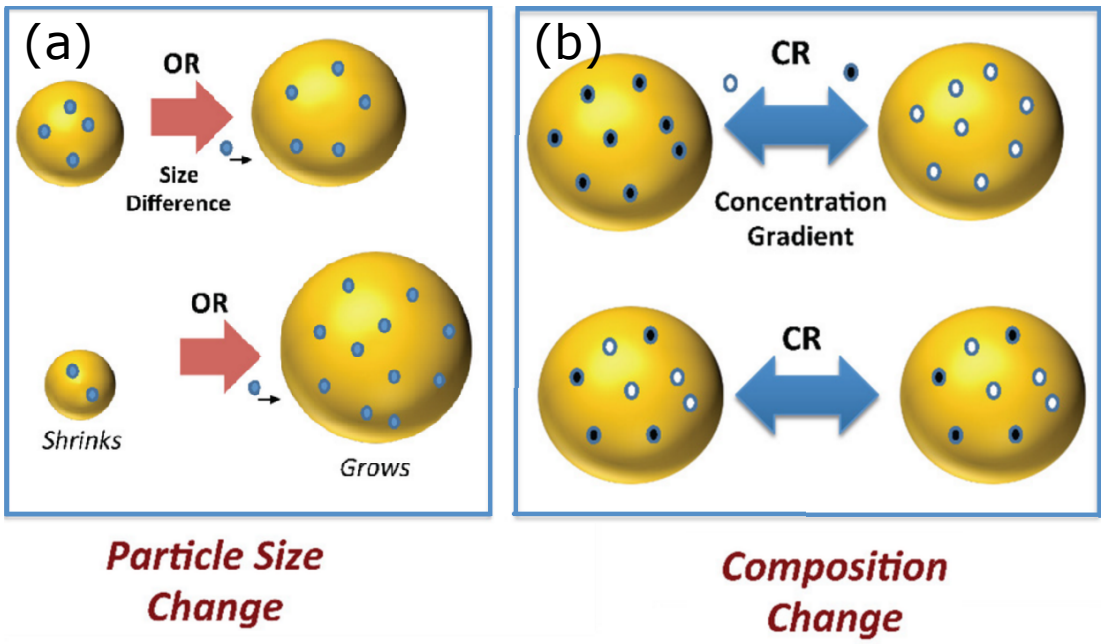

Figure 2.1 *Schematic for Ostwald ripening (OR) and compositional ripening (CR). Image taken from [13].*

called "tears of wine". A variety of very visual experiments can be designed using dyes employing Marangoni instability, as shown in Figure 2.2.

The Marangoni effect is a mass transport phenomenon that occurs along a liquid-liquid interface, with the surface tension gradient being its driving force. Therefore, compositional or temperature gradients in drops will change the surface tension value, producing Marangoni instabilities.

Figure 2.2 *Series of frames showing Marangoni effect when applying dish soap to dyed milk. Taken from [14].*

Toluene, ethanol and water is a classic combination for demonstrating the Marangoni instability because a concentration and surface tension gradient will be created when ethanol transfers from one phase to the other. A "dancing" movement can be observed as ethanol partitions inside the droplet, lowering the interfacial tension between the droplet and the bath. In this system, small variations in the amount of ethanol around the water droplet induces local differences at the interfacial tension values, making the droplet shuffle. [15]

In recent research using computer simulations, a compositional Marangoni force has been proposed as the coarsening mechanism for droplets in immiscible fluid mixtures [16]. They believe this force induces the motion of droplets, contrary to the traditional Brownian-coagulation mechanism where thermal fluctuations provoke collisions between droplets leading to coalescence. The different growth mechanisms possible for a binary liquid mixture are indicated in Figure 2.3. The authors believe it is in the droplet spinodal decomposition regime, green-colored, where the droplets' motion is hydrodynamically driven. This flow is possible due to an interfacial force normal to the interface due to inhomogeneities in the interfacial tension along the droplet interface.

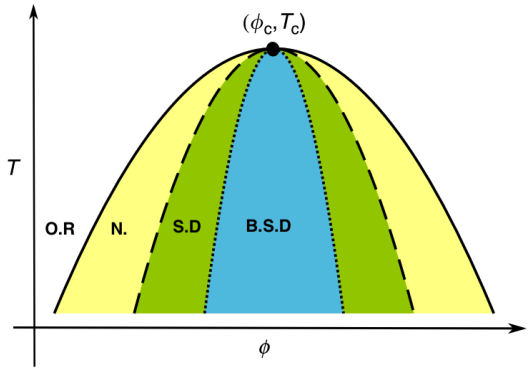

Figure 2.3 *Symmetric schematic phase diagram for a binary liquid mixture with the same viscosity η. Growth type is indicated by O.R for Ostwald ripening, N for nucleation, S.D for spinodal decomposition and B.S.D for bicontinuous spinodal decomposition. Image taken from [16].*

Intuitively, this can be explained in a similar fashion to Ostwald ripening. Transport processes are different, being translational diffusion of molecules for Ostwald ripening whereas in this novel explanation it is the hydrodynamic translational motion due to the Marangoni instability. The interfacial tension gradient gives rise to a flow which will create movement from a larger droplet with a lower interface tension towards a smaller droplet which has a higher interface tension.

2.2 Colloids at interfaces

Colloids are discrete pieces of a substance, with their size between 1-1000 nanometers, suspended in another substance, where they typically don't dissolve.

Some of their properties are Brownian motion (due to their small size), a very high surface to volume ratio and the fact that they experience attractive interactions due to Van der Waals forces and other effects make repulsive interactions necessary to prevent aggregation. Commonly, surfactants have been extensively used to stabilize emulsions via steric or electrostatic effects which suppress coalescence. However, they differ from colloids in the ability to form micelles, whilst there is a broader range of sizes available for particles, especially extending to larger sizes [17]. Surfactants usually adsorb and desorb easily from the interface in a reversible manner. Depending on their size, colloids become usually irreversibly attached to the liquid-liquid interface. The energy required to remove them may be around five orders of magnitude or higher than the thermal energy at room temperature, hence creating an extremely high energy barrier.

Interactions between colloids forming a monolayer is an important issue that can modify the properties of the interface. That is the same mechanism by which Pickering emulsions are stabilized, with particles adsorbed at the interface between the phases impeding coalescence between droplets. An important parameter for the success of the stabilization is the wettability of the colloids, defined by the contact angle (see Figure 2.4). In oil/water emulsions, amphiphile Janus particles, which have a hydrophilic and lipophilic behaviour at the same time, would be the best option. At a contact angle near 90°, known as neutral wetting, the particle has no preference for either phase, and would rest at the interface with the three-phase contact line at their equator.

Bicontinuous interfacially jammed emulsion gels, named bijels, are another example of how particles can be employed to stabilize an emulsion. Particles at the interface will arrest the spinodal decomposition created by quenching a liquid binary mixture [18]. Work has been done to create assymetrical and hierarchical bijels employing solvent-transfer-induced phase separation. This is done by injecting into a continuous phase a homogeneous mixture of three liquids, one of which is the solvent that makes the other two miscible. Then, by extracting the solvent the mixture becomes immiscibile, leading to phase separation [19]. The authors claim that these kind of bijels can be created by a wider range of liquids and particles, creating submicrometer domain sizes that increase the interfacial area, improving mass transfer rates between phases.

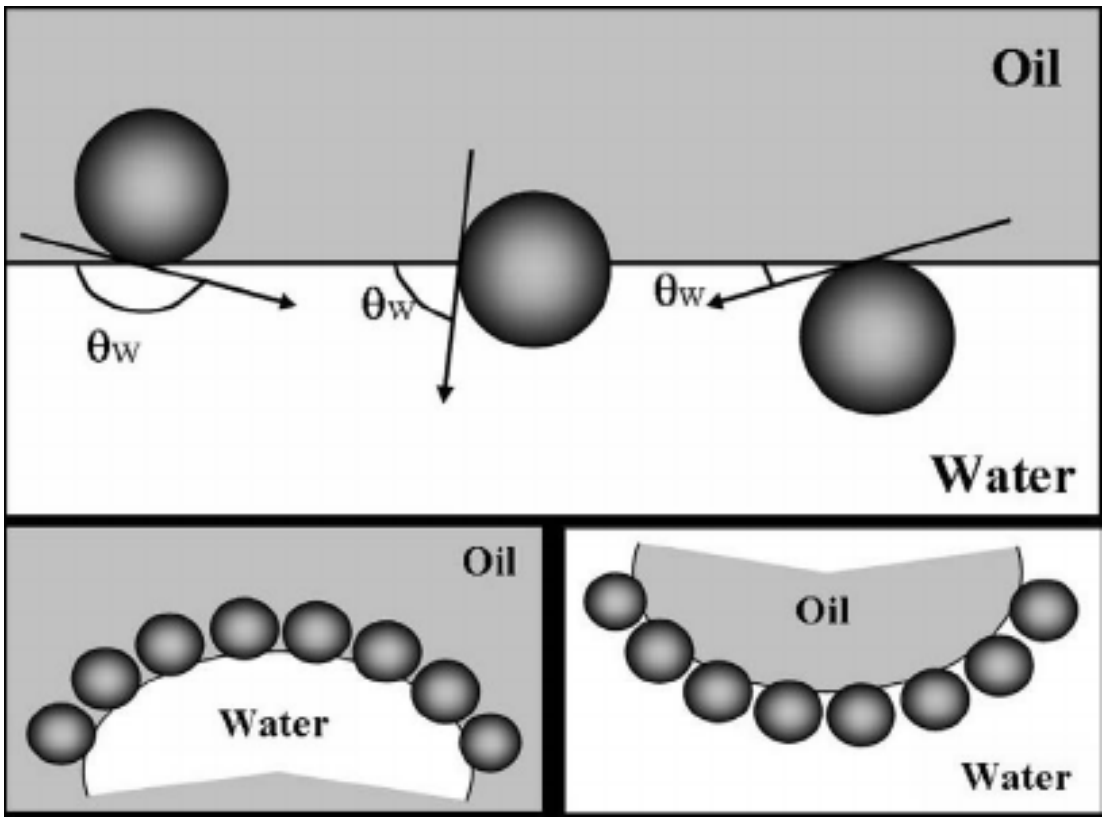

Figure 2.4 *Contact angle diagram for particles at air/oil-water interfaces. In (a) we can observe a hydrophobic, neutral or hydrophilic behaviour. (b) shows solid-stabilised aerosols or water in oil emulsions whereas (c) represents solid-stabilised aqueous foams or oil in water emulsions. Image taken from [17].*

2.3 Ternary systems

Experimental systems in which material is transferred in significant quantities is very useful in the study of spontaneous emulsification, as the rate and the amount of emulsification is greatly increased. This can be achieved using partially miscible liquids: ternary mixtures composed of an oil, an alcohol and water often have a standard and relatively simple phase diagram, like the one in Figure 2.5, with A being the miscible component, and B and C immiscible between them. These diagrams are represented by Gibbs triangles, where the vertices indicate pure components. Each side between two vertices represent a binary mixture made of those components, where its composition can easily be determined by use of the lever rule. This rule states that if you trace straight lines from each corner to the unknown point, the concentration for each component is given by the line length between the unknown point to the opposite side of the vertex divided by

the total length of the tracer line (in a binary system, or along any side of a ternary diagram). This has been graphically explained in Figure 2.5.

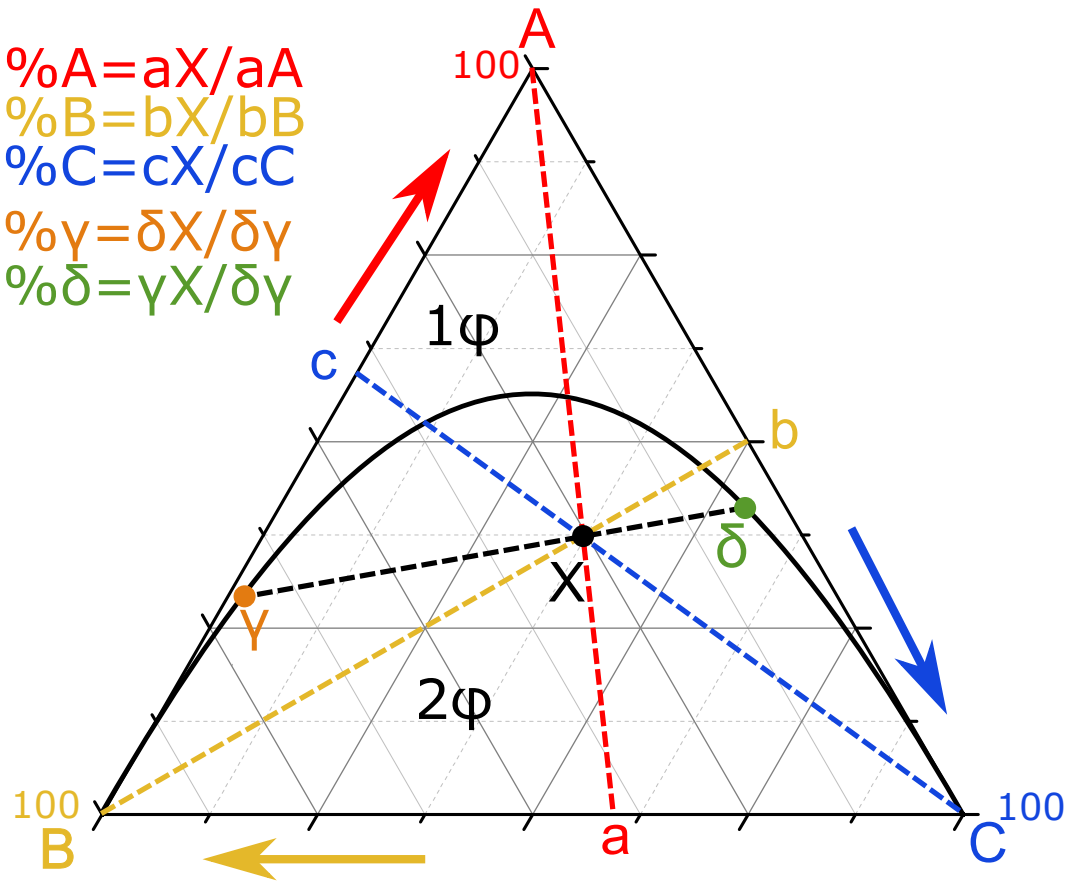

Figure 2.5 *Example of a Gibbs triangle and how to use the lever-rule to obtain the composition of an unknown point X. This can also be used to obtain the amount of each phase (γ or δ in a two-phase region (indicated by 2ϕ) under the binodal line*

In alcohol-oil-water systems, oil and water are typically immiscible. The addition of alcohol to the system improves miscibility leading to a binodal line which separates an alcohol-rich single-fluid phase from a two-phase region. In a sense, the alcohol in this system acts in a similar way to increasing temperature for binary phase diagrams, with a certain alcohol composition threshold above which it is a fully mixed, single-phase system. [20] The slope of the tie-line is also an important parameter in these systems, as it may alter completely the behaviour of the system. For example, an increasing slope will boost the partitioning speed of alcohol from one phase into another, or a change in the sign of the slope (positive or negative) is indicative of a crossover in the preference of the alcohol into one or another phase.

These systems become more complicated with the addition of surfactants, where

longer tails and/or more polar or charged heads are able to form new structures (micellar solutions, microemulsions and lyotropic liquid crystals) that modify the phase diagram, introducing new and diverse phases, sometimes simultaneously (see the ternary phase diagram of such a system in Figure 2.6). The emulsions in those systems will be more stable than in the alcohol-water-oil cases, as the surfactants stabilize the droplets' interfaces. The phase inversion temperature (PIT) and the phase inversion composition (PIC) methods, introduced by Shinoda [21], are the most used in surfactant systems.

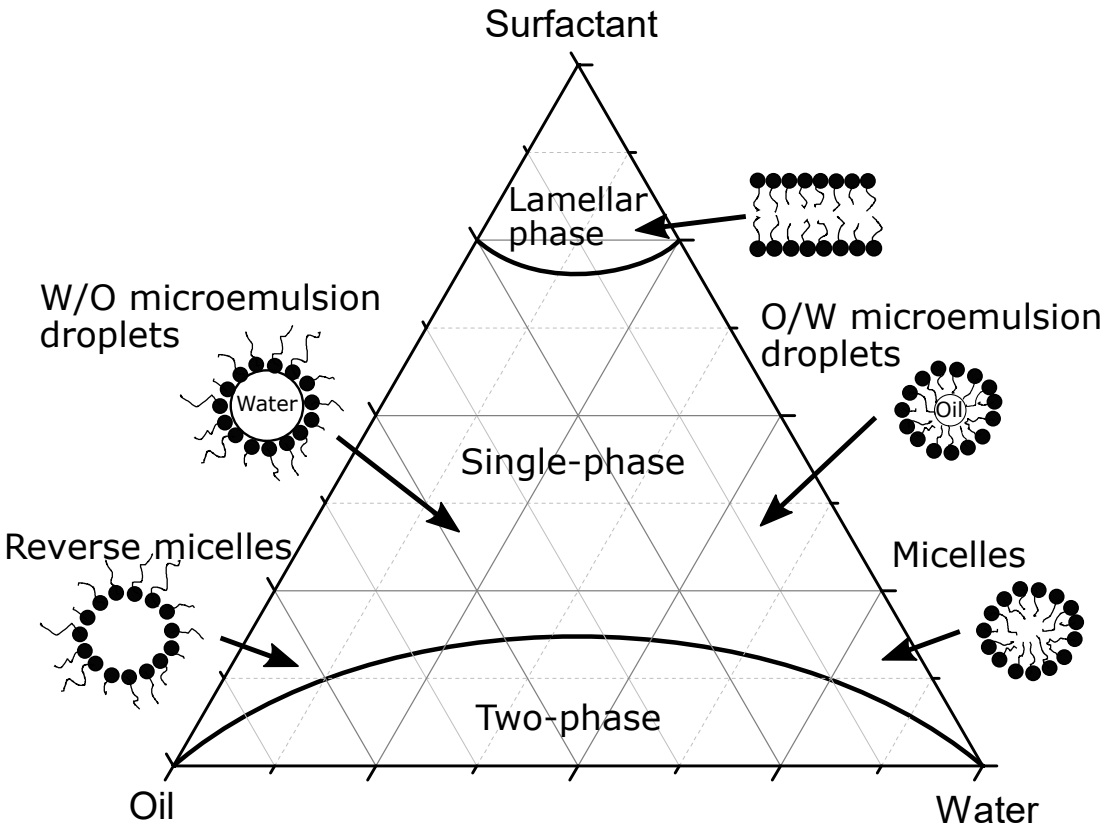

Figure 2.6 *Example of a ternary phase diagram for an surfactant-oil-water system. Depending on which region lies our composition, we can find several different structures formed by the aggregation of the surfactant molecules, such as micelles, microemulsions and lamellar phases. Adapted from [22].*

Ternary diagrams may be used to explain spontaneous emulsification if it is due to the "diffusion and stranding" or the "spontaneous change in curvature" of surfactant layers mechanisms. Because interfacial turbulence or negative transient interfacial tensions are phenomena related with dynamic behaviours rather than thermodynamic conditions, phase diagrams will not be helpful.

2.4 Spontaneous emulsification - Ouzo effect

An emulsion is a thermodynamically unstable system formed by two immiscible liquid phases, one dispersed in the other. To create them from liquid phases initially at equilibrium, energy, usually by mechanical means, must be supplied to create and expand the interface. However, the actual cost of producing an emulsion may be about a thousand times larger than the energy cost of the interface . For example, for an emulsion of oil in water with the following parameters; radius 1 μm, phase volume fraction 0.1 and interfacial tension 10 mN/m, the surface free energy would be ≈ 3 kJ/m^3 whereas the actual cost is at least 3 MJ/m^3. Most of the energy is lost by viscous dissipation. [23]

It is important to distinguish between self-emulsification and spontaneous emulsification. Self-emulsification is a term, usually related to the industrial applications, used to refer to systems containing surfactants which employ mechanical work to some extend to aid in the emulsification process. Spontaneous emulsification is a droplet creation process that occurs either when two immiscible liquids, not in equilibrium, are contacted with no external energy being supplied, e.g by thermal or mechanical agitation [24], or when an L3 phase undergoes a temperature-induced phase-inversion. [25] Spontaneous emulsification has importance for a variety of application areas, such as enhanced oil recovery, the production of nanoparticles and the creation of food-grade emulsions. [25–27] It may be produced by three mechanisms, which are: interfacial turbulence, low-tension interfaces, or diffusion and stranding. [28]

- Interfacial turbulence: Originally proposed by Quincke in 1888, he believed that interfacial tension gradients due to a non-uniform distribution of surfactant molecules or to local convection currents caused mechanical instabilities in the interface, tearing small drops away.[29] However, it has been proved that the addition of surfactants, electrolytes or a protein film will stop the turbulence without affecting the emulsification from happening. Nevertheless, the rate of emulsification its affected, as the interface material is now not renewed as frequently as it did in a turbulent regime. Therefore, this mechanism is incapable of explaining spontaneous emulsification in systems without turbulence. [30].

- Low-tension interfaces: If the interfacial tension is very low, it may become temporarily negative due to fluctuations, leading to an spontaneous growth

of the interface. This instability may break the interface and produce small droplets. A negative interfacial tension would mean a rapid increase in the interfacial area spontaneously [28], which can occur if an increase in the interfacial area decreases the entropy of the system. Although zero or negative interfacial tension in binary systems would indicate miscibility, it's been shown that for solutions with a strong repulsion between components it is possible to obtain such negative values on miscibility gaps. [31] For example, when contacting two immiscible liquids reacting at the interface to produce surfactants. The chemical reaction may overpopulate the interface resulting in a effective interfacial tension that is negative, thus expanding the interface. This results in a catalytic reaction that speeds up the reaction as the interfacial area increases. [32] There are some old experimental cases where the extrapolation of the interfacial tension curves (e.g, versus applied voltage, or pH range) into negative values results in spontaneous emulsification. For example, an applied potential to a drop of mercury immersed in an aqueous solution containing quarternary ammonium cations results in a parabolic electrocapillarity curve that would yield negative interfacial values over -2 volts. [33] Another example is obtained when long chain salts are contacted with fatty alcohols and the spontaneous emulsification occurs at concentrations where the extrapolated interfacial tension is negative. [34] This mechanism also explains how an oil, with a fatty acid (like oleic acid) content between 5 to 20 %, carefully contacted with an aqueous alkali presents spontaneous emulsification only in the pH range (9 to 12) where the interfacial tension appears to be negative.[35] A mathematical treatment of this explanation has been carried out by Granek et al. [36], whose model assumes a single spherical oil drop in bulk water (or vice versa). When the surfactants adsorb, the interfacial tension decreases and may become transiently negative. This can create undulations that grow, reducing the interfacial concentration of surfactant. Where these fluctuations become highly corrugated, small droplets may detach.

- Diffusion and stranding: It is based on the fact that local supersaturation regions produced by the diffusion of species driven by chemical gradients can lead to the formation of emulsion droplets. Nowadays it is thought of as the main mechanism for spontaneous emulsification. It has been proved [30, 37] that many systems will still experience spontaneous emulsification after the addition of surfactants, which suppress interfacial turbulence (therefore ruling out the first mechanism), or in systems whose interfacial tension

is higher than 0.001 N/m (which should exclude the second mechanism). However, the rate of emulsification is reduced if the turbulence is suppressed.

This mechanism is likely whenever the third component increases considerably the mutual solubility of the oil and the water, and will work independently of the interfacial tension values. For example, when contacting water with an oil-alcohol phase, the alcohol can diffuse towards the aqueous phase leaving some oil stranded, which may nucleate into droplets if it is supersaturated enough. Emulsification may be found in the other phase too, as the alcohol deficit in the oil phase may create water droplets as water becomes saturated. When contacting a 65/35 % n-propanol/2,3-dimethylpentane phase with a pure water phase at 35° C (see Figure 2.7), droplets in the water phase are created close to the interface, where supersaturation should be greatest. This indicates that the droplets were formed as a result of local super-saturation, not by deformation of the interface leading to droplet break-off.

The diffusion and stranding mechanism is generally accepted as the main cause for spontaneous emulsification, with the other two playing a secondary role. [26]

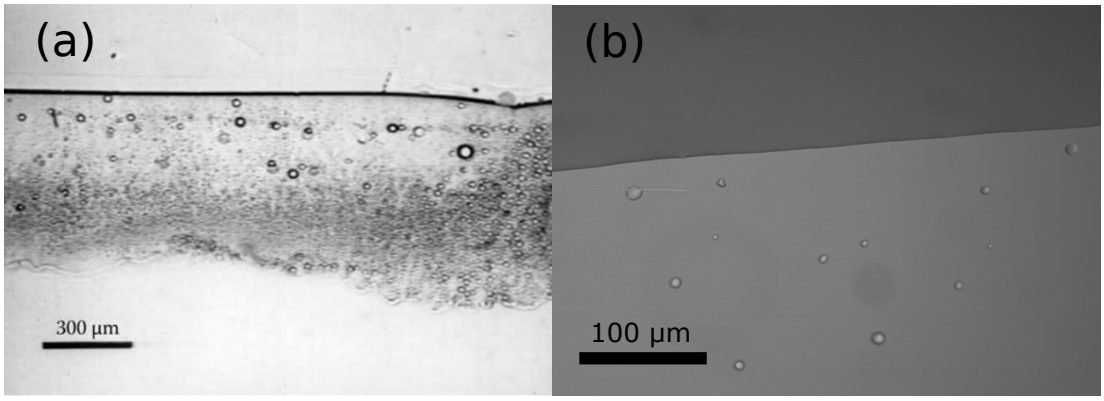

Figure 2.7 *Microscope pictures showing spontaneous emulsification, formed by the "diffusion and stranding" mechanism, after contacting water (at the top) with (a) 65/35 % n-propanol/2,3-dimethylpenthane and (b) 65/35 % ethanol/toluene (at the bottom). Image (a) taken from [38].*

This same mechanism is believed to explain the Ouzo effect too. This term was first used by Vitale and Katz [39], naming it after the Greek aniseed beverage, Ouzo. This drink is prepared by adding water to a mixture of ethanol and a flavor oil, which provokes an striking change in appearance as it becomes milky. This is because the emulsification droplets are microscopic, scattering all the colors equally to form a white suspension. As the ethanol partitions into the water it

takes oil molecules with it rapidly leading to the supersaturation of the oil in the aqueous phase. Nucleation and growth of oil droplets follows; this phenomena and associated self assembly are currently the subject of intense research. [40–42] The late stage coarsening of the oil droplets is driven by Ostwald ripening which might be expected to lead to macroscopic phase separation. However, the 'Ouzo effect' occurs in a narrow region in between the binodal and spinodal lines in which metastability is possible. According to the IUPAC's Goldbook [43], the coexistence (binodal) curve is the "*boundary of stable phase separation (limits of solubility)*" [...], whereas the spinodal curve is the "*boundary of separation between metastable and unstable phases*"[...]. Therefore, when represented on a ternary phase diagram, the area between those curves indicates metastability (see Figure 2.8). These curves vary with temperature and pressure, and due to fluctuations, it is not a well-defined area in real systems. The stability in Ouzo systems improves the lower the mutual solubility between the water and the oil is, whereas the droplet size is dependent on composition variables, densities, solubilities and temperatures. [26] For example, it has been proved [5] that the trans-Anethol/Water/Ethanol system (the classic Ouzo system) undergoes Ostwald ripening on its spontaneously formed droplets. However, although the rate of ripening increases with increasing oil concentration for low ethanol compositions, it is the opposite for high ethanol compositions (over 30%). The authors mention as possible causes the formation of a strong alcohol/water monolayer, which opposes the Ostwald ripening by reducing the surface tension, which is a factor directly correlated with the Ostwald ripening rate. The Ouzo effect has also been reported in multi-component drops, where the evaporation of ethanol pushes the composition into the Ouzo zone. Four different stages were found on a sessile Ouzo drop (made of water, ethanol and a tiny amount of anise oil) sitting in a hydrophobic substrate. First, ethanol starts evaporating, preferentially at the rim, which leads to oil droplet nucleation due to a deficit in the alcohol. Then, the drop becomes clouded as the oil droplets cover the whole drop. When all the ethanol has evaporated, a water drop will be sitting on a oil-ring, losing its spherical cap. At later times water will evaporate, leaving only the oil. [44, 45] This is a similar phenomenon to the coffee-ring effect, when a preferential evaporation at the rim of the drop, which is replenished constantly, leaves a ring-shaped stain. [46] If such drop is sitting in a superamphiphobic substrate, the oil droplets will start to nucleate at the apex of the drop, where the ethanol evaporation rate is larger. [47] Instead of having an oil rim, the oil wraps around the drop at the final stages. [44]

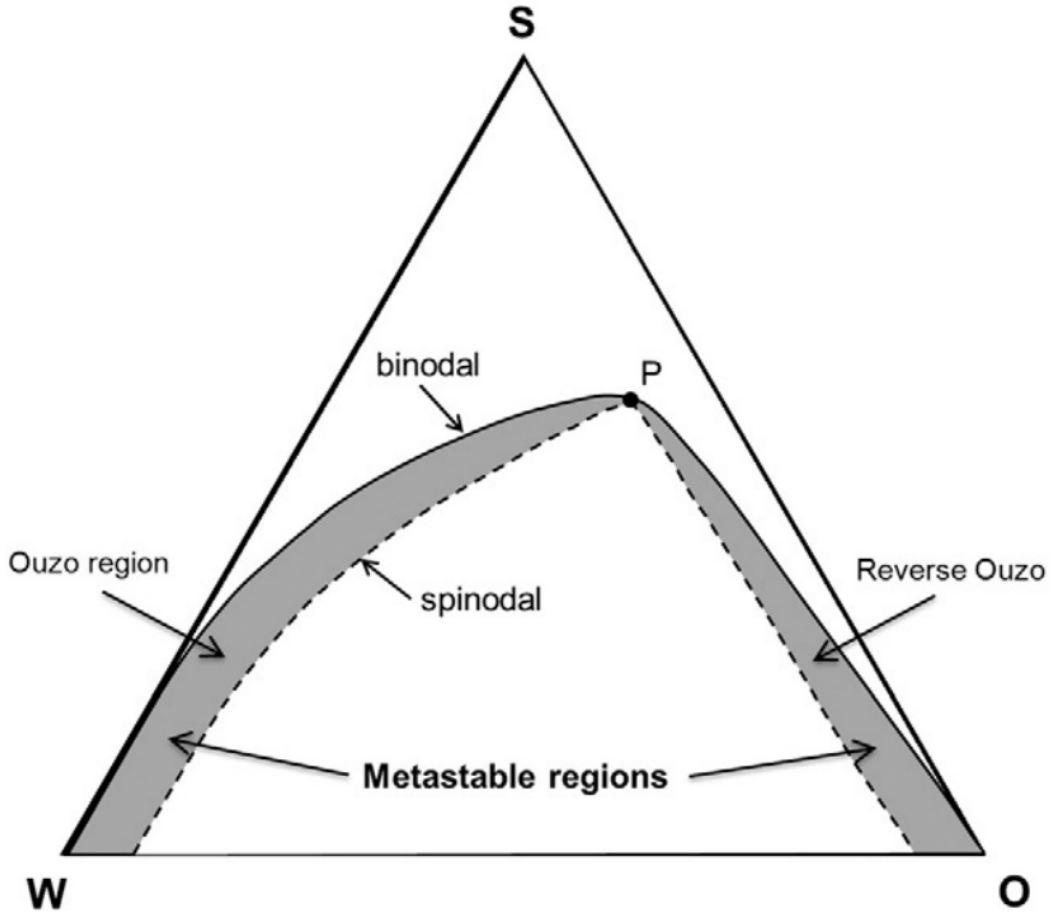

Figure 2.8 *Ternary diagram which shows where the Ouzo (and reverse) effect takes places. This occurs between the binodal and spinodal curves, which converge at the critical point (P). Taken from [26]*

More mechanisms of spontaneous emulsification have been proposed, although they are restricted to systems with very specific conditions, such as: [25]

1. Incorporation of oil into aqueous vesicular phases containing AOT solution creates oil films into the surfactant bilayers, destabilizing the vesicles and "exploding". [48]

2. Changes in the spontaneous curvature of the surfactant layer due to a temperature or concentration gradient. [49–51]

3. Diffusion of water due to osmotic pressure into fixed inverted micelles that grow, interconnect and invert to form O/W emulsions when contacting a highly viscous W/O microemulsion with water. [52]

4. Explosion of liquid-crystal phases when contacting a slightly polar com-

pound (long-chain alcohols or a surfactant in a hydrocarbon) with an aqueous solution. A liquid crystal, or intermediate liquid crystalline phase, in a myelinic form grows quickly and "explodes" into a large amount of droplets. [53, 54]

For the "diffusion and stranding" mechanism, a diffusion path theory coupled with the phase diagram of the system can foretell its behaviour at the early stages, predicting if, and in which phase, the emulsification will take place. This has been experimentally verified by Ruschak and Miller in 1972. [55]. This theory was extended to liquid systems based on the work done in isolated precipitation in multiphase solid systems by Kirkaldy and Brown. [56] The criterion they found was that only if the diffusion pathways connecting the phase compositions cross the binodal line on the ternary diagram will emulsification take place.

Ruschak and Miller's diffusion path theory relies in some simplifications. The analytical model employed, which uses the diffusion equation, assumes the following; no convection, transport of each species dependent only on its own concentration gradient in radial direction (Fick's diffusion laws), the diffusion coefficient of each species in each phase being independent of composition, maintained equilibrium between phases at the interface and uniform mass density of the system throughout. If intermediate phases with different density values than the initial phases are created during the experiment that may invalidate the theory results, as large-scale convection between phases may occur. Also, it does not allow for coalescence, and shall be limited to initial times only, when at least a part of each bulk phase retains its initial composition.

We have included a reduced version of the mathematical approach presented in [55] for the diffusion path theory needed to explain the existence of spontaneous emulsification: initially, two semi-infinite (which allows to use the similarity solution to the diffusion equations) phases (with compositions ω_i, i for each component, and primed or unprimed to distinguish between phases) are contacted, producing a moving interface whose position is given by $\epsilon(t) = k\sqrt{t}$, where k is a constant. This has been schematized in Figure 2.9. This moving interface is the link between our two phases, which later on the experiments would be the bath and drop solutions, and couple the equations for each phase together to produce a satisfactory prediction of the system evolution. This can also be seen as the requirement that both compositions (bath-drop) must be joined by tie-lines on a ternary diagram, thus connecting and coupling their compositions.

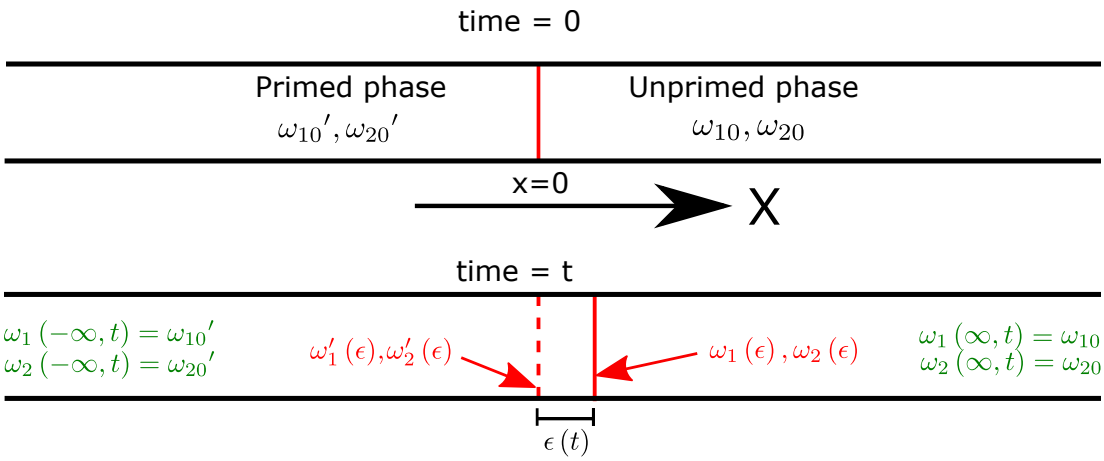

Figure 2.9 *Diagram used to explain the diffusion path theory when contacting two semi-infinite phases. Its initial compositions (top picture) are* $[\omega_{10}{}', \omega_{20}{}']$ *and* $[\omega_{10}, \omega_{20}]$*, with an interface (shown as a red line) between them at* $x = 0$*. Said interface has moved by* $\epsilon(t)$ *after a time t (bottom picture), indicating the old interface as a dashed red line. The compositions at the left and right hand side of the interface (shown as a red straight line) are, respectively,* $[\omega_1{}'(\epsilon), \omega_2{}'(\epsilon)]$ *and* $[\omega_1(\epsilon), \omega_2(\epsilon)]$*. Boundary conditions are included in the bottom picture in green color. Adapted from [55].*

Only two components need to be known, as the third can be obtained from $\omega_3 = 1 - \omega_1 - \omega_2$ for both phases. The boundary conditions, if the primed phase is situated at the left (negative) of the origin (where the initial interface is located) and the unprimed phase at the right (as shown in Figure 2.9), are:

$$\begin{aligned} \omega_i(x \geq 0, 0) &= \omega_i(x = +\infty, t) = \omega_{i0} \\ \omega_i{}'(x \leq 0, 0) &= \omega_i{}'(x = -\infty, t) = \omega_{i0}{}' \end{aligned} \tag{2.1}$$

For a situation such as the one described above, the transport equations are:

$$\begin{aligned} \frac{\partial \omega_i}{\partial t} &= D_i \frac{\partial^2 \omega_i}{\partial x^2} \\ \frac{\partial \omega_i{}'}{\partial t} &= D_i' \frac{\partial^2 \omega_i{}'}{\partial x^2} \end{aligned} \quad (i = 1, 2) \tag{2.2}$$

where ω_i is the composition of the i^{th} component, D the diffusion coefficient, t the time and x the position.

If we expand one of the previous equations into each component i and add them together, along with the composition constraint in ternary diagrams (the sum of the components in each phase must be equal to 1), we obtain that the

diffusion coefficient (at both phases, primed and unprimed) for each component must be equal, i.e, $D_1 = D_2 = D_3 = D$. The main advantage of using equal and concentration-independent diffusion coefficients is that diffusion paths draw on ternary diagrams turn into straight lines, resulting into much easier interpretations later on when used to predict spontaneous emulsification.

Component mass balances at the interface must satisfy:

$$D_i \frac{\partial \omega_i}{\partial x}\bigg|_{\epsilon} - D_i{}' \frac{\partial \omega_i{}'}{\partial x}\bigg|_{\epsilon} = \left[\omega_i{}'\left(\epsilon\right) - \omega_i\left(\epsilon\right)\right] \frac{\mathrm{d}\epsilon}{\mathrm{d}t} \tag{2.3}$$

We have used the approximation $D_i = D_i{}'$, which allow us to avoid the determination (which is rather difficult task) or calculation (based on model predictions) of diffusion coefficients, although it limits our model to systems where those values are similar.

Once all the previously mentioned simplifications and approximations are applied, we are able to obtain an analytical solution to our problem. Without this treatment, solving the diffusion equations (Equation 2.2) needs to be done numerically in most of the situations. Using our approximations restrict us to solutions only for a short time after contacting the phases, with no influence of different diffusion coefficients.

From Equation 2.3 we obtain a solution that coupled with the ternary equilibrium diagram determines the values for the compositions at the interface and various constants of the system. Once those values are known, the solution from Equation 2.2 is determined, and the diffusion path can be constructed. It is important to note that the solutions to Equation 2.2 may not be unique in ternary systems.

A typical diffusion path is formed by three elements: a curved segment connecting the initial composition ($[\omega_{10}, \omega_{20}]$) of one phase to its interface composition ($[\omega_1\left(\epsilon\right), \omega_2\left(\epsilon\right)]$), a tie-line connecting the interface compositions of both phases (because local equilibrium at the interface is assumed) , and another curved segment towards the initial composition of the other phase (see Figure 2.10). The diffusion path must cross at least once the straight line between the initial compositions due to mass conservation. This may be used as a first criterion to discard some spurious solutions. If the diffusion coefficients for all the components in both phases are the same, these curves degenerate to straight lines. An example

of these can be seen in Figure 2.10, with the initial contacted compositions as points A and D, and the tie-line shown in red as the dashed line B-C. The interface compositions are given by B and C. The nomenclature used agrees with that previously explained and employed in Figure 2.9. Spontaneous emulsification will occur if the diffusion paths create regions of local supersaturation by crossing the binodal. For example, in Figure 2.10 the segment A-B creates such a region, shadowed in gray.

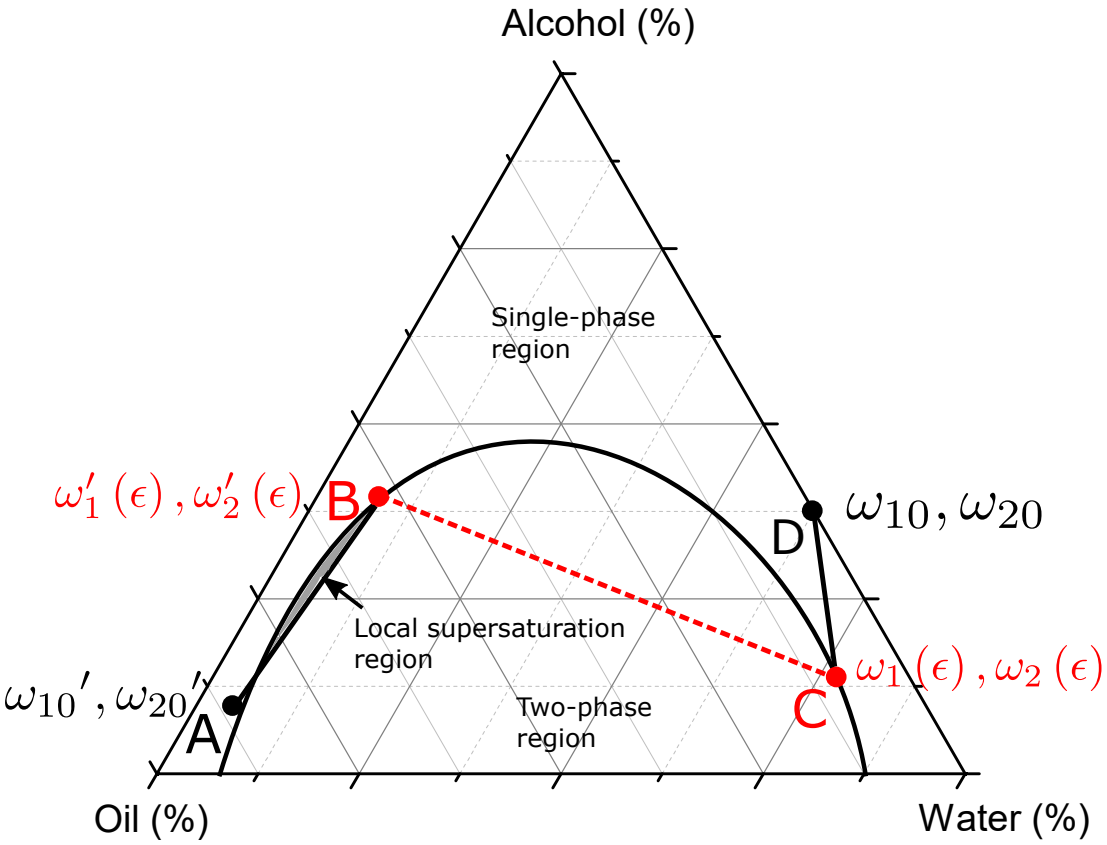

Figure 2.10 *Schematic ternary phase diagram for an alcohol-oil-water system. When contacting A and D compositions, the diffusion path is ABCD, with the tie-line and interface compositions shown in red color. Nomenclature agrees with the system presented in Figure 2.9. Adapted from [55].*

The term spontaneity is not well defined, being used variously to refer to either the rate or the amount of emulsification. In industry, the Collaborative Pesticide Analytical Committee of Europe test is used as a very simple tool. It consists of letting free-fall a 1 ml drop of the oil contained in a pipette into a 100 ml container of water from a height of 4 centimeters, evaluating the resulting emulsion as good, moderate or bad. A new approach using light scattering to measure the time it takes an emulsion to reach a constant average drop size may give more meaningful

and comparable results.

Studies on a system composed of water/ethanol/benzene showed that for compositions near the plait point contacted with water, spontaneous emulsification appeared to occur in two different stages: first, a very fast and large-scale emulsification followed by a slower diffusive process with little emulsification. [57, 58] Bimodal distributions were also observed in different systems [59, 60], with nanometric (measured with NMR) and micrometric (measured with light scattering) droplets. As the ternary compositions reach the metastable regions, diffusional coupling effects become increasingly significant. They are able to modify the diffusion paths into serpentine trajectories, which allows spontaneous emulsification even in systems where the diffusion path analysis should forbid it. [61]

2.4.1 Applications

- **Pesticides** [62] : Makes it possible to carry out on-farm emulsification, despite water hardness. This means that transporting water-diluted products to farms can be avoided, saving costs and logistical issues.

- **Detergency** [63] : To enhance the cleaning power of a liquid by a number of means: (a) Adsorption at interfaces, (b) lowering of interfacial tension, (c) solubilization, (d) emulsification, and (e) formation and dissipation of interfacial charges. Solubilization, which plays an important part in removing and keeping the oily soil in the bath, usually becomes significant when surfactants are present at concentrations over several critical micelle concentrations. For important macro emulsification low interfacial tension or a spontaneous emulsification mechanism is vital.

- **Skin care products** [64]: Hand and face lotions are made of the following ingredients, in decreasing order: water, acting as the transport medium and shortly hydrating the skin before evaporating; emollients, which are the softeners of the skin, such as lanolin or mineral oil; humectants like glycerin to preserve the moisture level and emulsifiers to keep the emulsion stable; high molecular weight polymers to increase the viscosity and achieve the desired consistency. Some minor ingredients such as fragrances, preservatives and skin-care additives are also included. Products will either be W/O and O/W emulsions, the latter being the more common,

mainly because of the feeling that an W/O emulsion will have and cost-related reasons. The oil products (emollients and fragrance) are dispersed into an aqueous phase made of water and all the soluble ingredients (like humectants). More complex systems such as W/O/W emulsions have been used when some ingredients need to be protected inside the oil phase.

- **Cutting fluids** [62, 65]: They are designed to dissipate heat created by the cutting action and to lubricate. Usually sold in a concentrated form made of a mineral oil, anionic and nonanionic surfactants, they are self-emulsified to make O/W emulsions when mixed with water in large tanks. The oil will be the lubricant agent, whereas the water is a good cooling agent because of its high specific heat. These emulsions will become unstable under shear and heat, cooling the tool by water evaporation and depositing the oil as a lubricant.

- **Enhanced oil recovery** [62, 66, 67]: After the primary and secondary oil recovery methods, only about 30% of the oil is recovered, the rest being trapped in pores. The tertiary enhanced oil recovery tries to recover further oil by increasing the capillary number. This may be done by pumping a surfactant-polymer mixture to decrease the interfacial tension. Spontaneous emulsification also helps by washing the oil from the rocks as the surfactant gets into the oil phase, which also increases the size of the oil droplets. A synergistic effect takes place when using small amounts of surfactant with an alkaline additive, in order to create an ultralow interfacial tension.

- **Formation of nano emulsions and nanoparticles** [68, 69]: Minehan and Messing produced SiO2 nanoparticles using tetraethoxysilane, water and ethanol by spontaneous emulsification. Emulsification was produced by the "diffusion and stranding" mechanism, whereas coalescence is the cause for the droplet growth, which is affected by the interfacial tensions, initial droplet size and rate of gellation. PMMA particles were obtained by solvent displacement by adding large amounts of water to an initial polymer solution.

2.5 Solvatochromism

Solvatochromism is the phenomenon occurring when there is a shift in position of the ultraviolet (UV)/visible/near-infrared (IR) spectrum of a chemical compound

related with a change in the polarity of its surrounding medium. Its origin arises from intermolecular solute-solvent interactions, either nonspecific, such as electrostatic or polarization forces, or specific, like hydrogen bonding or electron-pair donor/acceptor forces.

Differential solvation of the ground and first excited state of the solute can cause two different types of solvatochromism: positive if there is a bathcromic (red) shift, or negative if the shift is hypsochromic (blue) when increasing the solvent polarity. A better stabilization of the ground state yields positive solvatochromism, whereas if the dipole moment for the ground state evolves towards higher values than the excited state does ($u_g > u_e$), we would have negative solvatochromism (see Figure 2.11 (b)). The intensity and sign of the solvatochromism is not only dependent on changes in the dipole moment, but on the ability of the solute to form hydrogen bonds with the solvent.

Reichardt's dye (2,6-Diphenyl-4-(2,4,6-triphenylpyridin-1-ium-1-yl)phenolate), whose structure has been included in Fig. 2.11 (c), is one of the dyes with the strongest solvatochromism observed. Also called Betaine 30, it is a zwitterion, having both a positive and negative charge separated, albeit being neutral. When it absorbs light, an electron is promoted from the HOMO (Highest Occupied Molecular Orbital), corresponding to the phenoxide group, to the LUMO (Lowest Unoccupied Molecular Orbital) molecular orbital, situated in the pyridinium group. This charge transfer converts the molecule from polar to nonpolar, therefore transitioning from being able to better stabilizer the ground state to better stabilize the excited state. Just briefly remark that when one color (wavelength, or frequency band) is absorbed, we are able to see its complementary color, i.e if our dye absorbs red, we will see the solution as green. Using Reichardt's dye, this is the case for acetone, for example, whereas a more polar solvent such as methanol will display a red color (see Fig. 2.11 (d). That is, in acetone we are absorbing red light, whereas in methanol we are absorbing green light, which has higher energy.

The polarity of a solvent can be defined as "the overall solvation capability (or solvation power) of solvents", which depends on "all possible intermolecular interactions between solute and solvent molecules, excluding interactions leading to definite chemical changes of the solute [...]" [72] Several solvatochromically derived polarity scales and their practicality have been collected in [73]. We would like to note the simplicity of using the dielectric constant value, and the usefulness of the $E_T(30)$ scale, based on Reichardt's dye.

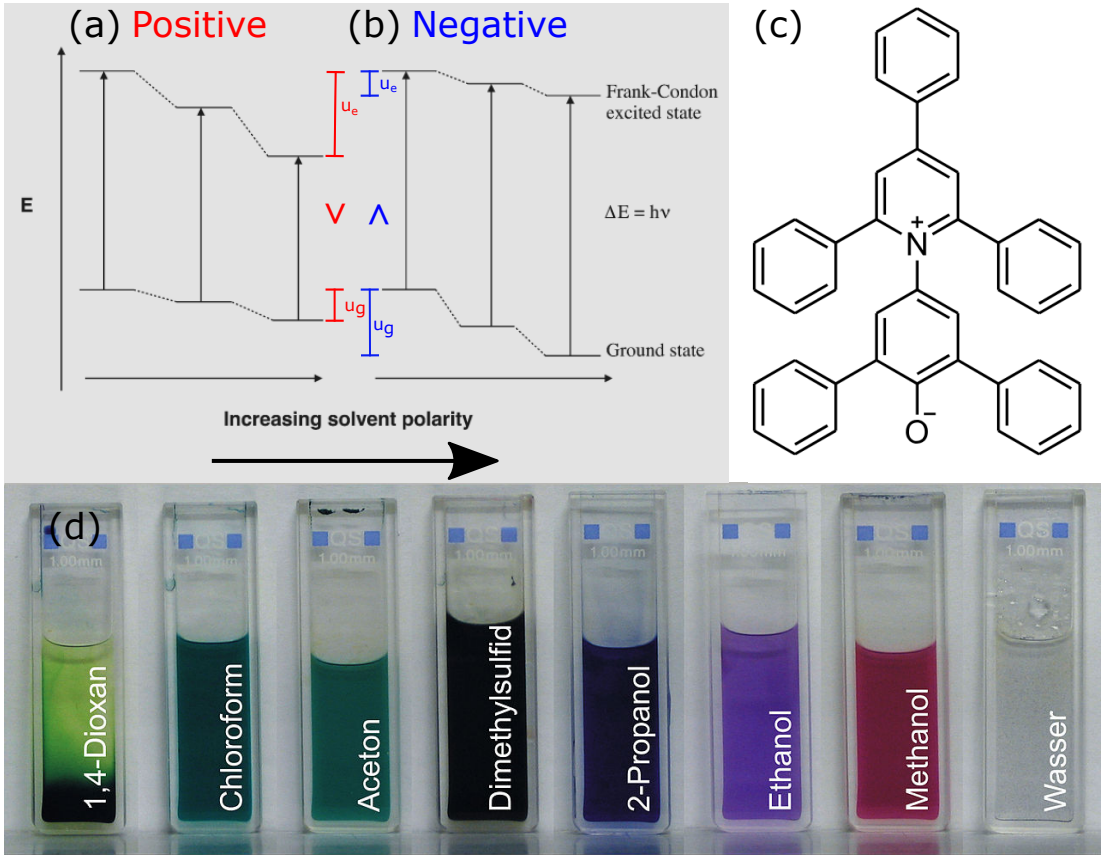

Figure 2.11 *Schematic representation of the energy levels of dipolar solutes when increasing the polarity of the solvent. (a) shows positive solvatochromism, with decreasing transition energy as the dipole moment of the ground state is smaller than the dipole moment in the excited state. (b) represents negative solvatochromism where the energy shifts to the red due to a higher dipole moment in the ground state than in the excited state. (c) structure of Reichardt's dye. (d) example of color changes when using Reichardt's dye, which exhibits negative solvatochromism, with different solvents ordered from left to right with increasing polarity. (a,b) adapted from [70] and (d) from [71].*

Lastly, mention that electronic transitions may be confirmed by searching for solvent induced spectral shifts, whilst the polarity of a solvent can also be determined by measuring the magnitude of the shift. Solvatochromism can be used to check the purity of solvents due to their sensitivity, but also fluorescent molecules have been used in biochemical and biological systems.

2.6 Fractals

Fractals are geometric shapes which are self-similar at different scales, that is, they look the same at different scales. They may be linear, if they are exactly self-similar (they look exactly the same at different scales) and originate from a "seed" that is duplicated and replaces the original line segments, or nonlinear, if they are derived from non-linear equations. These non-linear fractals share some features at different scales, but there is some variation. Some "famous" linear fractals were the ones produced by Koch ("snowflake"), Cantor ("dust"), Sierpinski ("triangle") or Hilbert ("curve"), whereas the most famous non-linear fractal is the one originated from the Mandelbrot set. These images can be seen in Figure 2.12 The interest in fractals, aside from a mathematical point of view, lies in its ability to model natural processes (such as percolation, or diffusion) and objects. In the human body for example, we can find examples in the cardiovascular system (arteries, veins and capillaries), respiratory system (alveoli) and in the nervous system at both microscopic (dendritic cells) and macroscopic (cerebellum) levels.

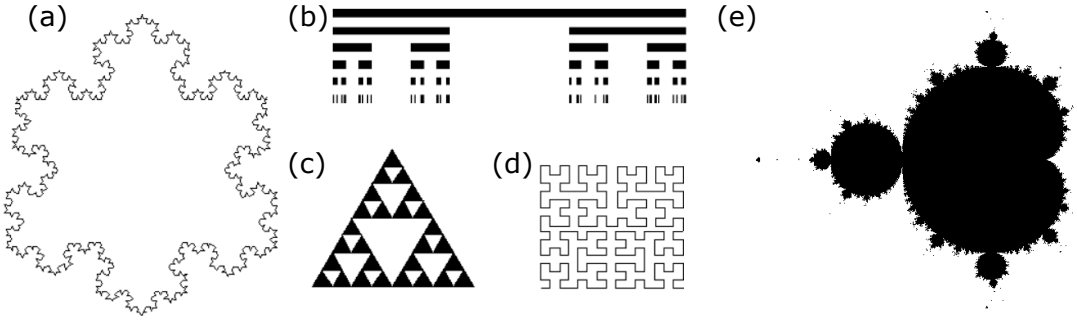

Figure 2.12 *Examples of well-known fractals, including the Koch snowflake (a), the Cantor dust (b), the Sierpinski triangle (c), the Hilbert curve (d) and the Mandelbrot set (e). Images adapted from [74].*

Euclidean geometry, where shapes have an integer dimension (0 for points, 1 for lines, 2 for areas and 3 for volumes), cannot be used to explain fractals, whose dimension is a non-integer value. Fractal dimensions were first introduced by Hausdorff and Besicovitch to demonstrate the existence of many curves whose dimensions lie between 1 and 2, with different dimensions according to the amount of information they present. These dimensions may be obtained exactly for those fractals with a mathematically predetermined structure according to the following relationship:

$$n = s^{-D} \tag{2.4}$$

where n is the number of line segments, s the "scale" and D the dimension.

However, for "real" objects which are not perfectly self-similar we need to use a numerical approach, such as the Richardson method, which allow us to obtain the perimeter fractal dimension. This method uses different measuring "scales" or "rules" to produce different measured lengths, with more precise (and usually longer) measurements when reducing the "scale" used. Therefore, the fractal dimension is effectively a measure of how detailed a pattern gets at smaller scales.

By plotting the measured length versus the scale in a logarithmic scale, the slope gives us a value for the fractal dimension, according to Equation 2.4. This method is readily extrapolated to two-dimensional objects by using measuring "tiles", or three-dimensional objects by using measuring "boxes". Other geometric objects may be used too (see Figure 2.13 (c)). One limitation of these methods is that the calculated dimension cannot be higher than the dimension of the measuring "objects". That is, our determined dimensions cannot be higher than 2 if using "tiles", or 3 for "boxes".

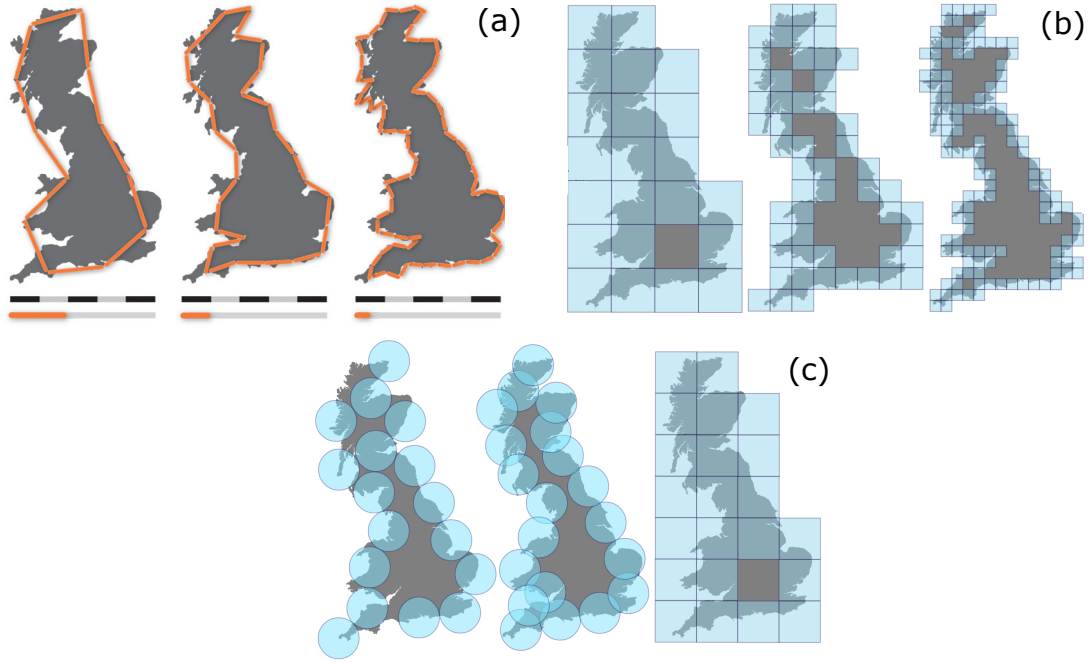

Figure 2.13 *A measurement of the UK's coastline may yield different results depending on the measurement unit. (a) shows three different "lengths" used, from larger to smaller values, where (b) use different "tiles" sizes, and (c) different measuring "objects" to obtain the same fractal dimension. (a) adapted from [75] and (b,c) from [76].*

In connection with our experiments, we are interested in the patterns generated

when diffusion is the main transport phenomenon, neglecting convection effects. One of the most commonly used models in this case is the diffusion-limited aggregation (DLA) model, developed by Witten and Sander [77]. This model was first used to explain colloidal aggregation by using particles undergoing Brownian motion dissolved in a fluid. These particles get irreversibly attached if they contact another particle, yet using a low particles' density value aggregation can be slowed until this phenomenon occurs only one particle at a time. Introducing first one particle at the centre, and subsequent particles far from it, those particles will either random walk until they collide or escape. The structures formed this way will be highly branched, with the fastest growing fingers shielding the inner parts of the structure.

The same type of patterns are observed in Hele-Shaw cells (see Fig. 2.14, where a high viscosity fluid confined in a thin cell is displaced by a different immiscible low viscosity fluid. The fractal dimension D in DLA relates the number of particles n with the radius of the cluster r as $n = r^D$. It has been found that in two-dimensions D=1.71, with a lower bound value of D=3/2. [78]

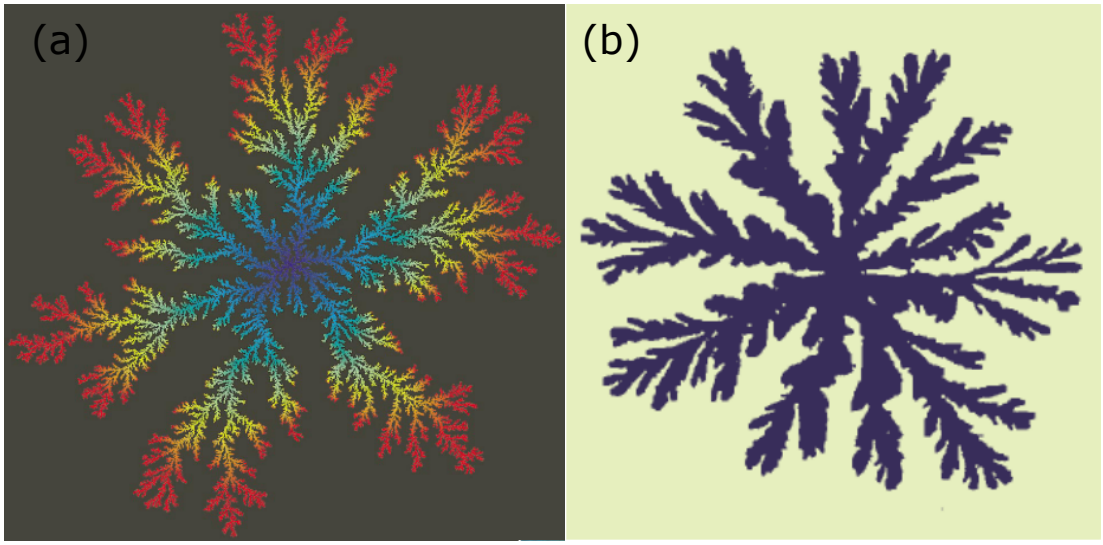

Figure 2.14 *(a) DLA cluster in two dimensions. Color scale goes from red (recent events) to blue (old events) to indicate how new particles will attach preferentially at the tips. (b) Hele-Shaw pattern obtained when injecting water (dark-colored) into 2.5% hexadecyl end-capped polymer (light-colored). Images adapted from [79].*

Chapter 3

Compositional ripening in the ethanol/toluene/water system

3.1 Introduction

Much current attention is focused on functional droplets able to perform a wide range of roles, from reactors in microfluidic devices [80] to containers for biological cells while they are analyzed. [81] The ability to dynamically control the size and composition of droplets mean that they also find application in, for example, electricity generation (microfluidic Kelvin device [82]), as dynamic lenses [83] or as sensors. [84, 85]

The exchange of material between drops is an important high-level form of functionality. [86] To study this phenomena it is useful to have an experimental system in which material is transferred in significant quantities. This can be achieved using partially miscible liquids: ternary mixtures composed of an oil, an alcohol and water often have a standard and relatively simple phase diagram. Without the alcohol, the oil and water are typically immiscible. Added alcohol improves miscibility leading to a binodal line which separates an alcohol-rich single-fluid phase from a two-phase region. Here, we are interested in a system comprised of toluene, ethanol and water, especially its behaviour as it attempts to reach compositional equilibrium. For our particular ternary system, an ethanol concentration above ≈ 60 vol.% always yields a single-phase system. [20]

Even for a single particle-stabilized drop, the behaviour in a ternary liquid system

can be quite unexpected. For example, if a water drop is injected into a toluene bath containing a small proportion of ethanol and interfacially active particles, it can sprout a tube which grows upwards. [15] This curious phenomena is driven by the partitioning of ethanol into the water drop, which then migrates towards the top of the drop due to its lower density. The enhanced ethanol concentration at the top of the drop softens the particle-coated interface directing the growth. The elasticity of the particle-coated interface is crucial for supporting the weight of the tube: fresh particles from the bath are adsorbed onto exposed interface during growth. Recent studies have probed the interaction between the sprouting tube and a pendant drop placed in its path. [87] The behaviour depends on bath composition and drop size, as expected, but remarkably also on the time when both drops are injected. If both drops are created at similar times, then the growing drop will try to avoid meeting the pendant drop. This reflects the fact that the pendant drop has had some time to absorb ethanol from the surrounding bath while the sessile drop has been growing. Because of the ethanol depleted layer around the pendant drop, the growing tube steers towards richer ethanol zones, away from the depleted layer. However, if the pendant drop is only injected as the growing tube approaches, then there is no time for the ethanol to become depleted: the tube approaches the drop. In place of direct contact, a "bridge" forms which appears dense and dark. It was suggested that the bridge was primarily comprised of particles from the continuous phase. [87]

The particles used in our system are fumed silica, which are small amorphous particles with a high surface area. These particles are produced by high temperature hydrolisis, injecting chlorosilanes into a flame of hydrogen and oxygen. Microdroplets of amorphous silica become fused into branched structures that agglomerate easily into chain-like clusters. They are used to reinforce the strength of various materials and to tune the rheological properties of the system. It is used as a universal thickening agent, anticaking, desiccant, light abrasive, filler or viscosity adjuster. [88]

Due to the presence of silanol groups on the surface of the particles, fumed silica is initially hydrophilic. However, it can be modified to be hydrophobic by using a fluid-bed reactor with dimethyldichlorosilane. This will transform the hydrophilic silanol groups (about 30% of the existing ones) into hydrophobic dimethylsiloxy groups. Fumed silica particles can be dispersed into mixtures of toluene and alcohol at low concentrations (about 0.6 vol. %). Manually shaking the solution yields a cloud-looking bath, but using a ultrasound probe for a few minutes will

produce a clear solution, that will remain stable for a few hours. After this period of time, the solution will become cloudy again, gelling after a few days.

These particles become irreversibly attached to the interface produced when injecting a water drop in a toluene-alcohol solution. Even at low particle concentrations (i.e, 0.2 vol. %), there are 10^4 times more particles in the bath than those needed to cover the drop surface, resulting in a huge excess of particles. The coverage of the drops' interface by these particles seems to suppress the Marangoni instability. Particle-covered interfaces also reduce the speed at which the drops change volume or shape, while also making the drop more able to resist gravity. [15] That is explained if we consider particle monolayers as two-dimensional elastic solids. Capillary forces aggregate the particles into a monolayer, whose elastic properties are dependent on the underlying surface tension, its particle diameter and geometry of packing. These "solids" will buckle under enough stress, returning to their original state once the stress is removed. They also experience fracture, with a tensile crack appearing when a drop of surfactant is added to the monolayer. Due to the huge change in surface tension and the advection of surfactant to the crack tip by Marangoni flows the crack propagates, resulting in a exposed interface with particles jammed at its edges. [89, 90]

Recent work has been carried out on particle coated interfaces, such as the study of the armor robustness of particle rafts probed via droplets' impacts. A sharp transition from stable to coalescing droplets can be observed when increasing the velocity of the droplets, with an opposite trend if the raft is immobile (where the velocity threshold decreases with increasing particle diameter). [91] A novel method to create water-in-water armored drops using "rafts" (monolayers) of particles has been reported recently [92]. A small drop situated on top of the raft, made of particles and a thin layer of oil, increases its volume until it destabilizes the whole raft, which sinks into the underlying bath (water) wrapping the drop. A dimensionless parameter, which compares the weight of the raft to the buoyancy effect, is enough to determine the shape of the drop, the raft deformation and the destabilization volume.

The novelty in this chapter resides in the use of macroscopic drops that allow direct visual observations coupled with microscopic phenomena observed under the microscope. The big size of the drops is in contrast with the most common use in the literature of microscopic droplets to obtain a large sample size that is statistically analyzed. However, by using these millimetric drops we can probe

some features that are often neglected, such as the elastic behavior observed between connected drops, the long time stability of macroscopic Pickering emulsions with reduced diffusion times due to their size, and how different drop-particle interactions can form some interesting structures.

In this chapter we have focused on the mentioned bridge created between injected drops of differing alcohol content immersed in an oil/alcohol/silica particles bath. By changing the experimental conditions we were able to replicate the formation of the self-assembled "bridge", which is composed of hundreds of spontaneously formed water-rich droplets trapped in the gelled bath solution. Those tiny droplets are created by the diffusion of water driven by the compositional gradient between injected drops. While there has been an effort to keep the system as simple as possible, the spectrum of phenomena observed during the later stages of our experiments is rich and diverse, as will be revealed later on.

3.2 Experimental methods

We have focused on video techniques to observe the time evolution of our system, which will help us to draw a picture as complete as possible of the new phenomenon this chapter introduces. Other techniques, such as Raman spectroscopy or rheology, have also been used to confirm our hypothesis. Depending on the scale of the experiments, we can distinguish between a 3D "bulk" configuration or a reduced 2D experiment (Figure 3.1). Glass cuvettes were chosen to avoid chemical reactions with our bath components. In the first case, a 9.6 mL Krüss SC01 cuvette was employed, whereas a 1 mm path length optical cuvette from Starna Scientific was used for the 2D setup. This thin cuvette allowed us to locate our system directly under the microscope and study its evolution in real time.

Our standard experimental procedure consisted of injecting drops into a cuvette filled with a certain bath composition and record their time evolution.

The bath has been prepared using toluene (Sigma-Aldrich, $\geq 99.7\,\%$), ethanol (Sigma-Aldricht, $\geq 99.8\,\%$) and fumed silica particles (HDK H30) with a cluster size $\approx$100 nm, which were a gift from Wacker-Chemie (Burghausen). The usual bath composition was 90 % toluene, 10 % ethanol and 0.2 % silica in volume. It was chosen to work in a system where the injected drops experience a slight

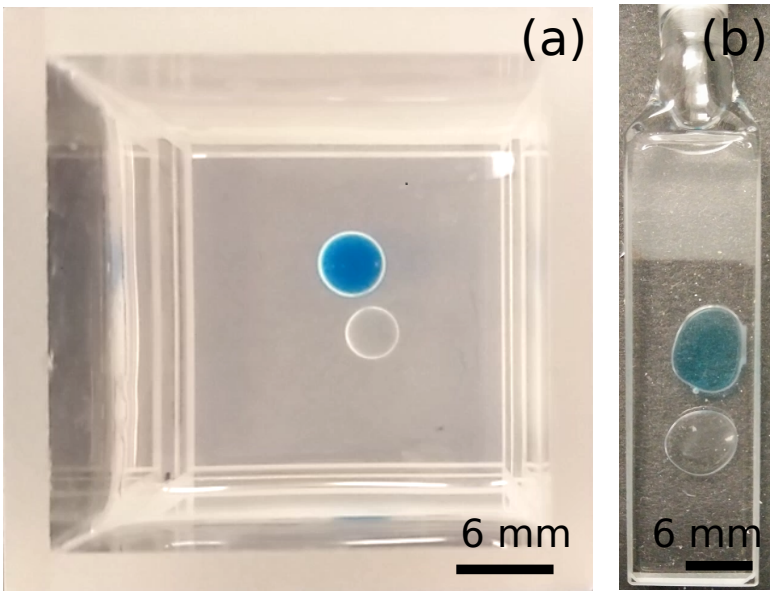

Figure 3.1 *(a,b) Experimental setup showing the cuvettes with the injected drops for the 3D and 2D configuration, respectively.*

volume expansion, according to the phase diagram described in [15]. Other compositions have also been studied, for example, varying the silica concentration to try to discern its importance and role.

The silica particles were dispersed in the bath using an ultrasound probe (Sonics Vibracell VCX500) for a total time of 2 minutes, using a 20 seconds on/off configuration with an amplitude of 20%. These are hydrophobic particles due to the dimethylsiloxy groups attached to their surface. Additional silica nanoparticles (radius 14 nm) were synthesized via the Stöber method [93] and fluorescently labeled with fluorescein isothiocyanate (FITC) dye (isomer I, Sigma Aldrich) as described by Imhof et al [94] by Dr. Andrew Schofield.

Usually two drops were injected, first a distilled water drop and immediately after and at a short distance a 50/50 vol.% water/ethanol drop. For the macroscopic studies using the 3D configuration, drops $\approx$30 μL were carefully injected using a Hamilton gas-tight #1750 syringe and a Krüss steel needle of 1.8 mm diameter at the bottom of the cuvette. For the microscopic studies a Hamilton Microliter #702 syringe with a Hamilton steel needle of 0.72 mm diameter was used to inject drops $\approx$5 μL, capping the cuvette afterwards to avoid evaporation. Care was taken while the drop was still attached to withdraw the needle.

The time evolution of the experiments was recorded using an Allied Vision Stingray F-046 camera (mounted on the Krüss EasyDrop apparatus) and a mobile

phone that captures High Definition videos (720p) for the 3D experiments. For the microscopic configuration, different microscopies were used, such as:

- Bright field microscopy was mostly carried out using a Nikon Eclipse E800 microscope (Fig. 3.2 (a)) with a ×4 objective. Other objectives (×4, 10 and extra long working distance (ELWD) ones for higher magnification) have also been used to make more detailed studies.
- Phase-contrast and dark-field microscopies were also used occasionally on this same microscope.
- Confocal Laser Scanning Microscopy (CLSM) was also performed with a Zeiss LSM700 confocal microscope (Fig. 3.2 (b)). It allowed us to record simultaneously the bright field and fluorescent channels, following different dyes and observing the system evolution at the same time. For this reason we added either a fluorescein dye (Fluka Fluorescein Reag. Ph. Eur., free acid) at 0.02 wt.% to the distilled water drop to follow the diffusion of water, or the aforementioned fluorescent silica particles at 0.02 vol.% into the bath to track the particle coverage of drops.

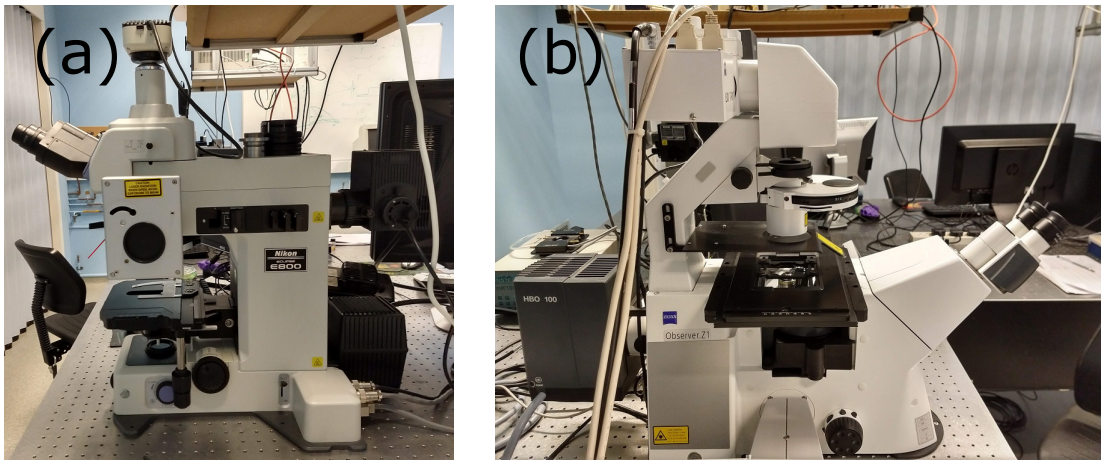

Figure 3.2 *Picture of the optical (a) and confocal (b) microscopies used*

As previously mentioned, Raman spectroscopy and rheology were employed to obtain quantitative results. The Raman spectrometer Horiba Jobin-Yvon LabRam HR800 (Fig. 3.4 (a)) with a λ=532 nm laser was used to study the composition of the injected drops. The experimental setup included a ×10 objective, a confocal hole diameter of 1000 μm, slit width of 100 μm, grating of 600 and exposure time of 3 seconds with 3 accumulations for wavenumbers in

the range of 200-4000 cm^{-1}. This equipment was used at Solvay's Laboratoire du Futur in Bordeaux, France, during my secondment in Autumn 2017.

Experiments were recorded measuring the Raman spectrum in one drop and then moving the sample holder until the laser was focusing onto the other drop. This way we obtained the time evolution of the composition for both drops at close times (the difference is the measurement time, which was about 30 seconds). A Python script (whose full code can be found in Appendix A.1) was used to analyze the large amount of spectra obtained. This script performed a background correction and integrated the water and ethanol peaks (doublet and triplet, respectively) indicated in Figure 3.3 (a). These integrated areas were converted into concentrations using a calibration curve, depicted in Figure 3.3 (b) , obtained under the same experimental conditions.

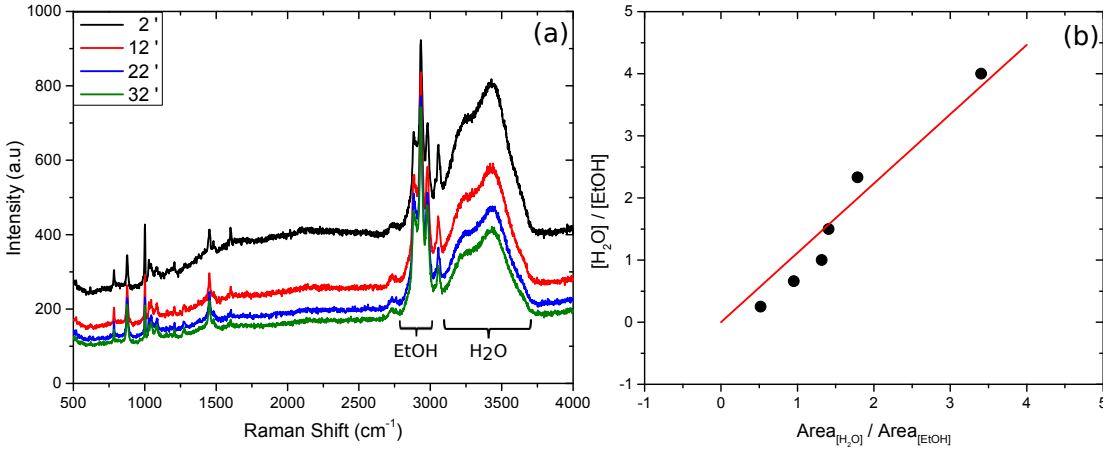

Figure 3.3 *(a) Raman spectrum at the center of the pure water droplet at four different times, indicated in minutes. The spectra have not been offset. (b) Calibration curve used to transform the Raman spectra into concentration ratios, which were translated into individual components. Fitted slope is K=1.12± 0.08.*

We were not able to determine toluene concentrations in the drops as its signal was masked by water/ethanol peaks. This is due to the enormous difference between the amount of toluene to water/ethanol. The same thing happened for the water/ethanol peaks in the bath, where no water signal was detected when the laser was focusing in the bath.

We characterized our bath solution with and without silica particles to gain an insight into what may be the role of said particles. Strain sweep measurements were performed with a Anton Paar Physica MCR 301 (Fig. 3.4 (b)), using a stainless steel cone-plate geometry where the cone diameter was 50 mm, its angle

1° and the gap between them 0.1 mm. About 1 ml of previously dispersed sample was spread out on the plate, and the cone carefully lowered. A solvent trap with added toluene to reduce evaporation was employed.

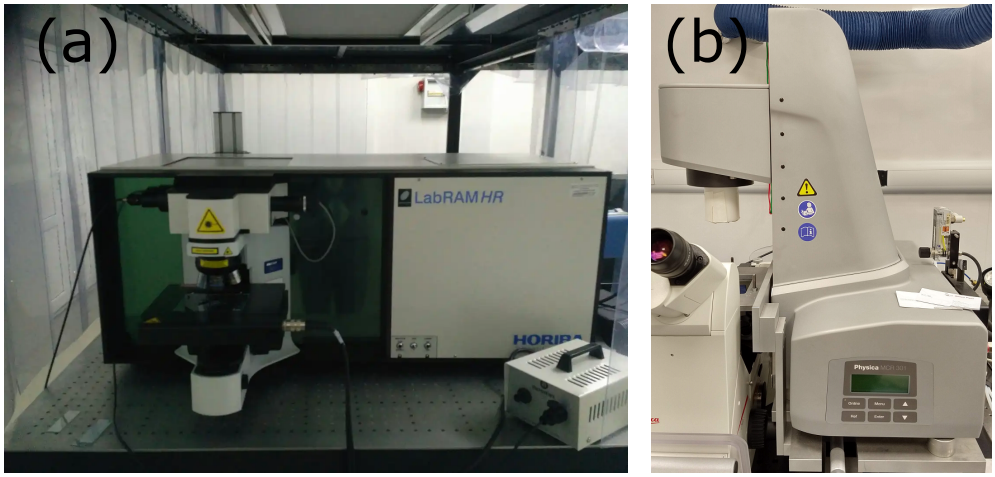

Figure 3.4 *Images of the Raman spectrometer (a) and rheometer (b) used. Image (a) has been taken from [95]*

3.3 Results

3.3.1 Macroscopic view

Inspired by the sprouting tubes phenomenon described in the Introduction section 3.1, we decided to explore more about these systems in search of novel behaviours. Systems with several pure water drops injected in the standard bath composition have already been described in [15] along with the experimental setup defined as the 3D configuration in section 3.2. The reported behaviour for same-composition multiple-drop systems is to behave as if each drop was alone in the bath, according to the phase diagram shown in Figure 4 in [15]. Depending on the alcohol and particle concentration, different phenomena are observed. For low ethanol concentration, the drops will experience a small volume expansion. However, at higher concentrations tube sprouting or overspilling are the most likely phenomenon to occur. Tube sprouting and its explanation has been described in detail in the Introduction, and more can be found in [15].

I have modified the previously presented approach, where various pure water drops were injected, by changing the composition of said drops. The aim was to observe differences in the way drops interacted with the bath depending

on their alcohol content. Two roughly 50 μl water drops with different alcohol concentration were placed in the bath with the standard composition. Figure 3.5(a, c, e) shows these two drops shortly after being injected, one of them 100 % distilled water and the other 50/50 vol.% water/ethanol. Drops with higher ethanol concentrations than 50% in volume will redissolve as soon as they contact the bath.

The pure water drop was dyed with Nile Blue A to distinguish it and to determine whether the surrounding phase becomes very strongly enriched with water. This would indicate that a great amount of water is coming out of the drop and into the bath, dyeing it. However, the amount of dye observed to leave the drop appears to be small, with any surplus dye being found at the air-liquid interface at the top of the cuvette.

Nevertheless, the main feature of this system is the structure, which resembles a "bridge", observed developing between the drops over a period of 10 minutes. It starts from the pure water drop and extends towards the mixed drop, Fig. 3.5(b, d). Evidently, the "bridge" formation seems induced by a composition difference between the drops. More experiments using different amounts of ethanol in the pair of water drops (such as 0-20 % ethanol for the low concentration drop, or 20-50 % ethanol for the high concentration drop) have been carried out. The same bridge formation phenomenon was observed, always being initiated from the lower ethanol concentration drop towards the other drop across the shortest distance between them.

The distance between drops and the time needed by the "bridge" to fully extend across their distance was fitted to the simplest case of diffusion. It obeys the equation $x = \sqrt{D\,t}$, where x is the distance, D the diffusion coefficient and t the time. The diffusion coefficient, through a nonlinear least squares fitting, yielded a value of $D = (0.55 \pm 0.08) \times 10^{-5}\,\mathrm{cm}^2/\mathrm{s}$. This will later be compared to the results obtained from the microscopic observations. As with shorter distances, the bridge formation time shortens as the composition gradient between the two drops becomes steeper.

To probe the nature of the bridge, one of the drops was pulled away to force the rupture of the structure, Fig. 3.5(e-h). Although the completed bridge behaves somewhat elastically for small "pushes", it does fracture if the drops are strongly forced apart. Following bridge breaking, the formation of a new bridge starting on the displaced drop can be seen. On the other drop, the thinning of the broken

bridge as time passes also becomes apparent.

Experiments with three drops using two different compositions were also performed. For example, two pure water drops at the sides of a mixed drop, or two mixed drops next to a pure water drop. In both cases the same phenomenon was observed; a structure extending from the low alcohol drops towards the high alcohol ones. For these systems, the observations made for the two-drop systems regarding how the distance and alcohol difference affects the bridging time fully applies, as can be observed in Figure 3.6.

3.3.2 Microscopic view

To obtain more information about the bridging process presented in the previous section, we confined the drops in a thin cuvette to observe what is happening between the drops at a microscopic scale. To do so we employed the 2D configuration described in the Experimental methods section 3.2, replacing the cubic cuvette by the 1 mm path length optical cuvette. The characteristic lengths of these drops will be smaller than the capillary length scale for water (≈2.7 mm) and ethanol (≈1.7 mm), so we can neglect the role of gravity in the shape of the drops. These values were obtained according to $\lambda_c = \sqrt{\frac{\gamma}{\rho g}}$, where γ is the surface tension, ρ the density and g the gravity acceleration.

The cuvette was then filled with the standard bath composition, and carefully two distinct drops with a compositional gradient between them were injected.

As a representative example of these measurements, Figure 3.7(a-d) displays a series of unprocessed frames obtained through bright field microscopy with a ×4 objective up to 30 minutes. This provides a better insight into the development of the bridge over time. Due to field-of-view limitations it is not possible to show both drops completely, but only their facing interfaces could be captured.

To gain more insight into the nature of the bridge and its components, higher magnification objectives were used to focus on the structure. In similar experiments [87] to those of the water droplets sprouting tubes a similar bridging phenomenon was observed. It was suggested that the bridge, which was observed between the growing sessile droplet and the newly created pendant droplet, was primarily formed from particles. Our experiments presented here demonstrate otherwise.

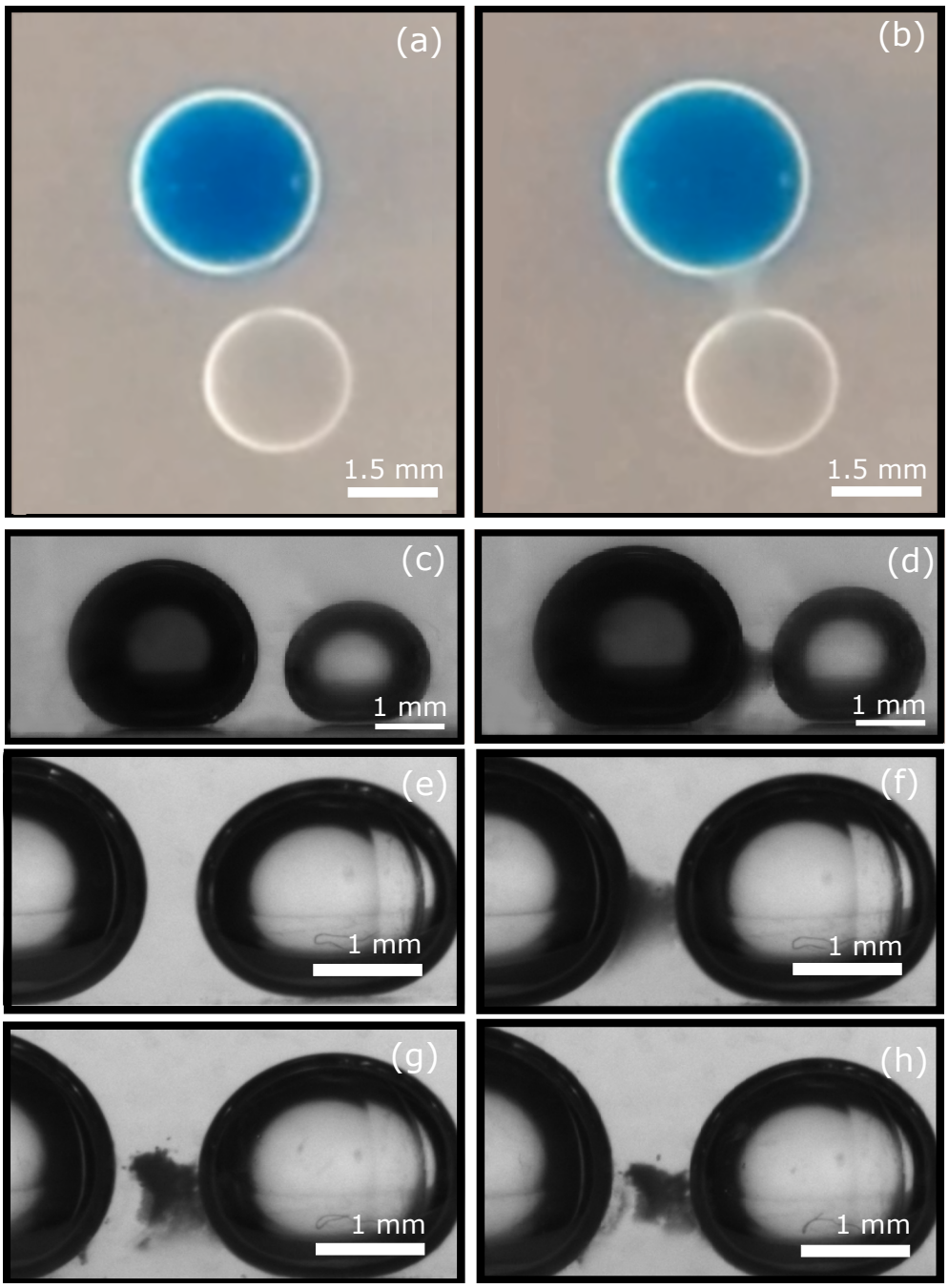

Figure 3.5 *(a-d) Two drops in a bath of standard composition (see Methods). The pure water drop is dyed with Nile Blue A (blue, black), the other drop is 50\50 vol.% water/ethanol. (a, c) The drops soon after being injected; (b, d) 10 minutes later, a cloudy-looking connection has developed between them. (e-h) Left, pure water drop, right, 50/50 vol.% water/ethanol drop with standard bath composition. (e) Immediately after injection; (f) 12 minutes later; (g) immediately after the bridge is broken; (h) 12 minutes later. The fracture of the old bridge, new bridge formation as well as thinning of the old bridge can all be observed.*

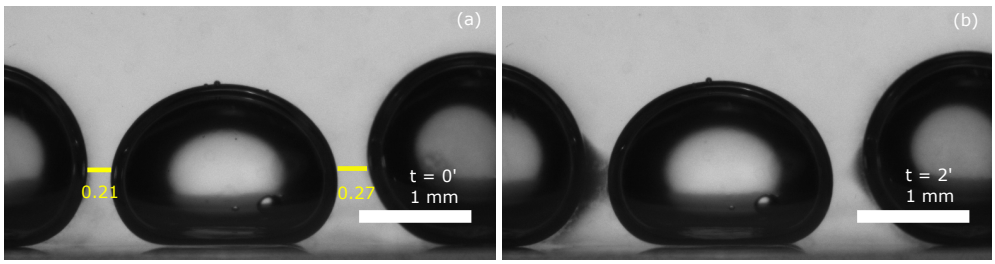

Figure 3.6 *Three drop system experiment consisting in two pure water drops dyed with Nile Blue A at each side of a pure mixed drop (50/50 vol.% water/ethanol), sitting in the center. The distance between the drops, in mm, has been delimited by yellow lines. (a) shows the system shortly after injection, and (b) two minutes later, when the bridge between the closest drops is completed.*

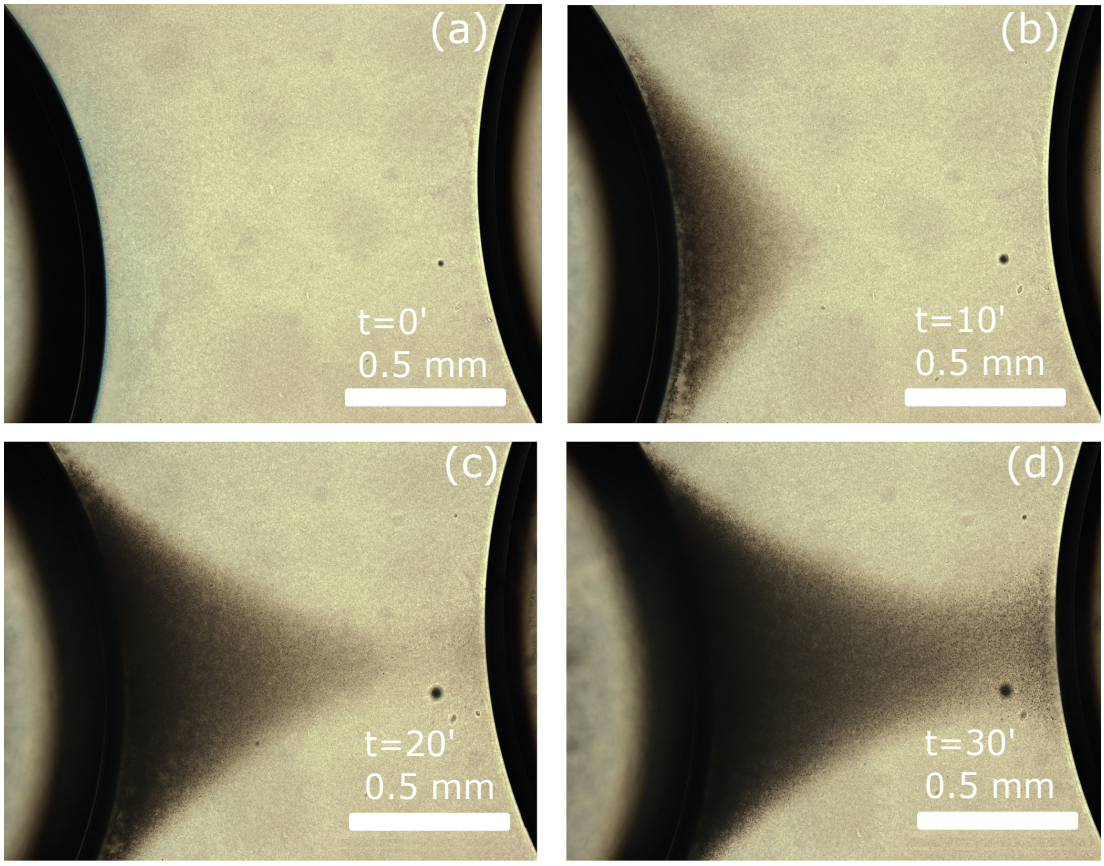

Figure 3.7 *(a-d) Selected frames showing a pure water drop on the left and the bridge growing towards the mixed drop on the right.*

Figure 3.8(a, b) displays a pair of frames showing the development over time in the middle of the bridge using a ×40 objective. At this scale, we are able to confirm that the bridge is comprised by thousands of tiny droplets. The droplets move only slowly ($\sim$ 100 μm in 24 hours) without being jammed into contact, which together with the bridge fracture shown in Fig. 3.5(g) suggests that they

might be held in place by a sparse network of nanoparticles.

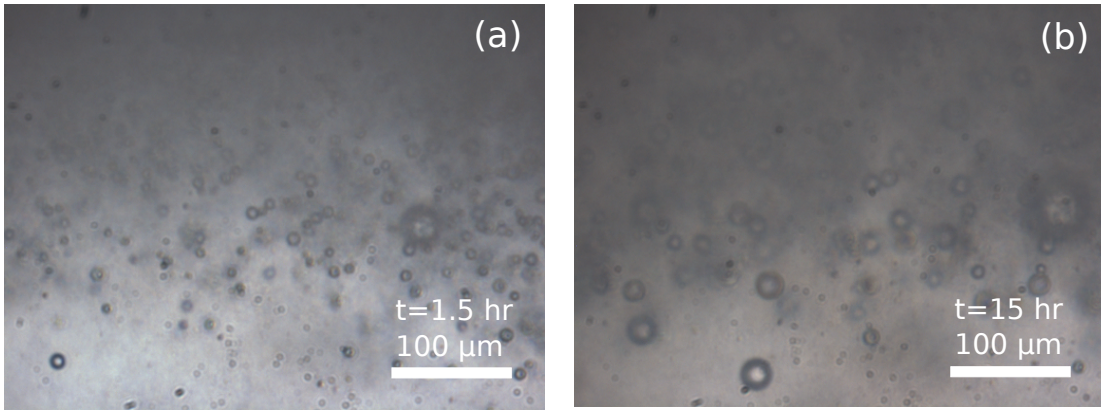

Figure 3.8 *(a, b) Bright-field microscopy images showing in detail what is happening in the middle of the bridge using a ×40 objective at two times.*

At this point, we will present the current explanation developed for this system which will be supported in the findings presented during the rest of the chapter. The reported [20] ternary diagram (by weight) for our system will be used to explain the bridge formation phenomenon.

We start by placing the three initial compositions that correspond to the bath, pure water drop and mixed drop in the ternary diagram in Figure 3.9. Please note that the lines drawn have NOT been calculated, and are merely suggestions:

- Initially, the bath phase has a composition indicated by the point where the red line meets the toluene / ethanol axis, Fig. 3.9(a, b). As water enters the bath due to the compositional gradient between the injected drops, the composition follows the red line. Once the bath composition crosses the binodal line (black lines) phase separation begins. If the bath phase remains in the metastable region between the binodal and spinodal (the 'Ouzo' region) the phase separation remains on the level of droplets.

- The mixed drop composition starts out at a little below the mid-point on the water/ethanol axis, Fig. 3.9(c). Once the drop is within the bath, the compositions of the phases on either side of the interface have to adjust themselves, by diffusion, to become two compositions joined by a tie line shown as a blue dashed line. This process for the mixed drop is indicated by the cyan line, Fig. 3.9(c).

- The pure water drop lies on the bottom right vertex and its composition evolves along the ethanol / water axis, deviating only slightly due to the

small amount of toluene able to enter the drop, as the ethanol increase is able to solubilize it.

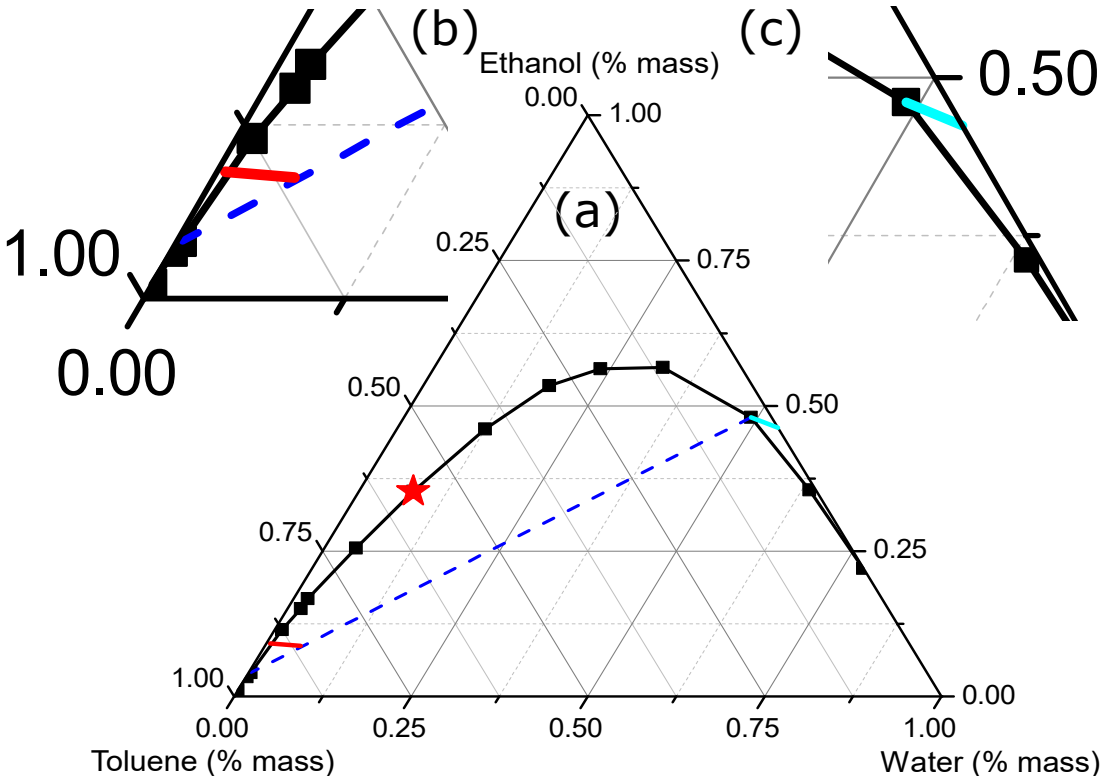

Figure 3.9 *(a) Ternary phase diagram for the toluene, ethanol, water system. The black line is the binodal, the red star is the critical point and the blue dashed line is a tie line which joins two compositions. Experimental points were taken from [20]. (b) The bath (typically 90 % toluene, 10 % ethanol) moves along the red line as water diffuses in. Local phase separation occurs into a continuous phase and a droplet phase joined by a tie line. (c) The surface of the mixed drop (typically 50 % water, 50 % ethanol) moves along the cyan line as it comes into equilibrium with the surrounding bath. The ethanol concentration scarcely changes.*

A sketch of the bridge formation mechanism is shown in Fig. 3.10, and explained in the following paragraph:

Hypothesis. *Underlying this mechanism is the diffusion of water from the pure water drop to the mixed drop, creating supersaturated areas where the local water concentration is able to randomly nucleate into droplets. There will be an ensemble of droplets of different sizes that will evolve under Ostwald ripening due to their different Laplace pressures. We found that although there are no particles covering the droplets, they are essential for the formation of the bridge, as observed in experiments with varying concentration of silica. The particles dissolved in the bath modify its liquid behaviour, which is now gel-like. This will cause the droplets to be under arrested movement. For long times, the evolution of the system towards equilibrium has been studied, with some surprising findings, such as the reversal of flow, or the final compositions of the drops.*

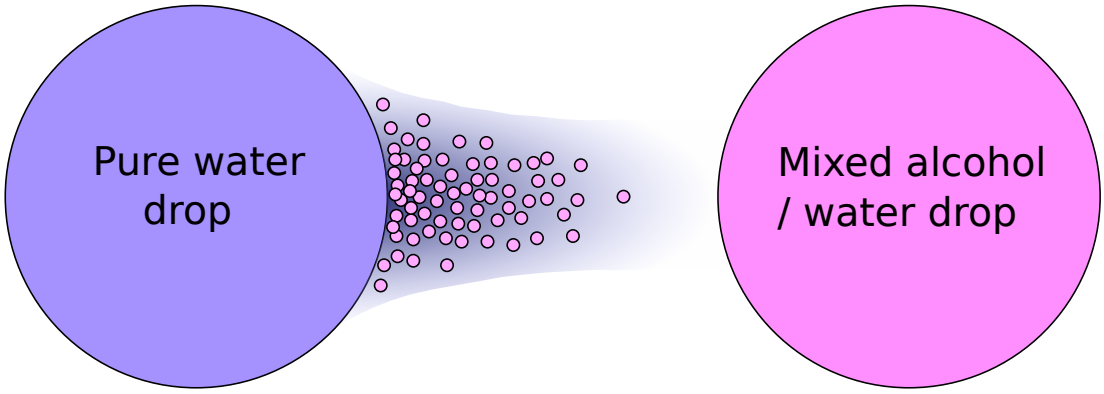

Figure 3.10 *A cartoon of the droplet formation process. For clarity the particles on the drop interfaces and in the bath phase are not shown.*

To demonstrate the diffusive behaviour of our system, the growth behaviour was quantified by measuring the time needed for the bridge to extend to half the drops' separation as a function of their separation distance. These times were obtained from the photomicrographs using the software Fiji [96]. Our procedure was as follows:

1. Find the halfway point between the drops along a line connecting their centers.

2. Convert the colour images into gray-scale for easier determination of intensity levels.

3. Suppress noise by averaging the gray values perpendicular to the line of centers in a rectangular region of interest (about 100 μm total width).

4. Detect the sharp decrease at the center-point in the average gray value going through the movies frame by frame.

We recorded the time at which the sharp decrease reaches half the distance between drops as our halfway bridging time. This and the corresponding data for the macroscopic experiments are represented in Figure 3.11. The data for the 2D and the 3D experiments has been fitted separately to the aforementioned simple diffusion model. For our microscopic experiments, a diffusion coefficient of D=$(1.1\pm0.1)\times10^{-5}$ cm^2/s was obtained. This value, double that the obtained for the 3D experiments, is very close to the value obtained for the mutual diffusion coefficient $D_{12} = 0.88 \pm 0.01$ between water and toluene. [97]

This suggests that the diffusion of small molecules is playing a very important role driving the bridge growth between the drops.

To further demonstrate the diffusion of water, another experiment with the standard compositions but using a fluorescent agent in the water drop under CLSM was performed. The diffusion of the dyed water is shown in Figure 3.12 and can be seen especially in the outer parts of the"bridge". This is easily explained by noting the vast amount of droplets at the center of the bridge, which will scatter hugely, therefore obscuring the image. We believe the diffusion follows the shape indicated in the cartoon at Fig. 3.10 as a purple shadow.

A further role of the water diffusing between droplets is that it destabilizes the dispersed silica particles. These partially hydrophobic particles can be dispersed reasonably successfully in our bath by sonication. The droplet formation process described above will remove some ethanol from the continuous phase into the water/ethanol droplets, as well as into the injected drops. These changes in the bath composition, reducing the amount of ethanol, may also be responsible for destabilizing the dispersed particles in the space between the drops.

The volume for the spontaneously formed droplets over 24 hours have been determined using the highly magnified images and have been included in Figure 3.13. Spontaneous formation of the droplets occurs, as previously hypothesised, as the water concentration in the bath increases enough to create random nucleation spots. Water diffusing from the pure water drop towards the ethanol-rich drop paves the way for droplet formation, and we observe the bridge

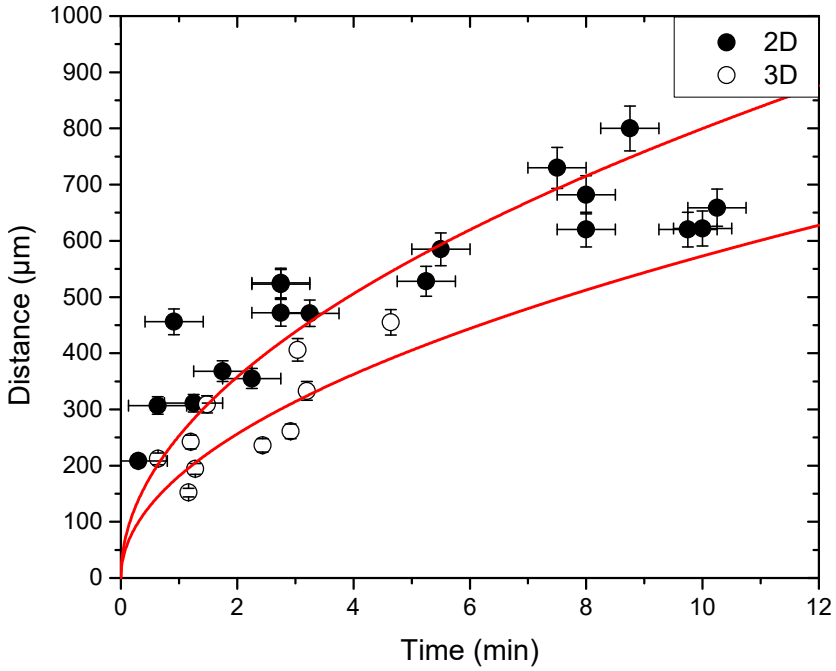

Figure 3.11 *Time needed for the bridge to reach half the distance between the drops versus their separation distance. 2D experiments are represented as black filled circles, whereas the 3D experiments discussed in the Macroscopic section 3.3.1 are shown as white empty circles. Red lines indicate the best fit line of the function* $x = \sqrt{D\,t}$*, where* x *is the distance,* D *the diffusion coefficient and* t *the time, for each separate set of points.* $D_{2D} = (1.1 \pm 0.1) \times 10^{-5}\ cm^2/s$ *and* $D_{3D} = (0.55 \pm 0.08) \times 10^{-5}\ cm^2/s$*. Error bars indicate repeatability error.*

in that direction because the higher water content is close to the pure water drop.

Once the droplets are created, they will increase their volume until there is an ensemble of different sizes, causing the smaller droplets to shrink until they redissolve in the bath whereas the larger droplets are shown to undergo a linear increase in volume over a period of hours. This could be Ostwald ripening given that the droplets are in the range 2–20 μm, although compositional effects due to slow changes in the bath composition are also possible.

The coverage of the liquid-liquid interfaces by the silica particles have been studied using confocal microscopy. Usual compositions were modified by replacing 10% of the fumed silica with fluorescent silica. Surprisingly, whereas the injected drops are covered with silica almost immediately, the small spontaneously formed droplets appear to have no particle coverage at all, as shown in Fig. 3.14(a). It can be inferred by the difference in brightness for the yellow halo between the injected drop's interface and the droplet's interface shown in the inset.

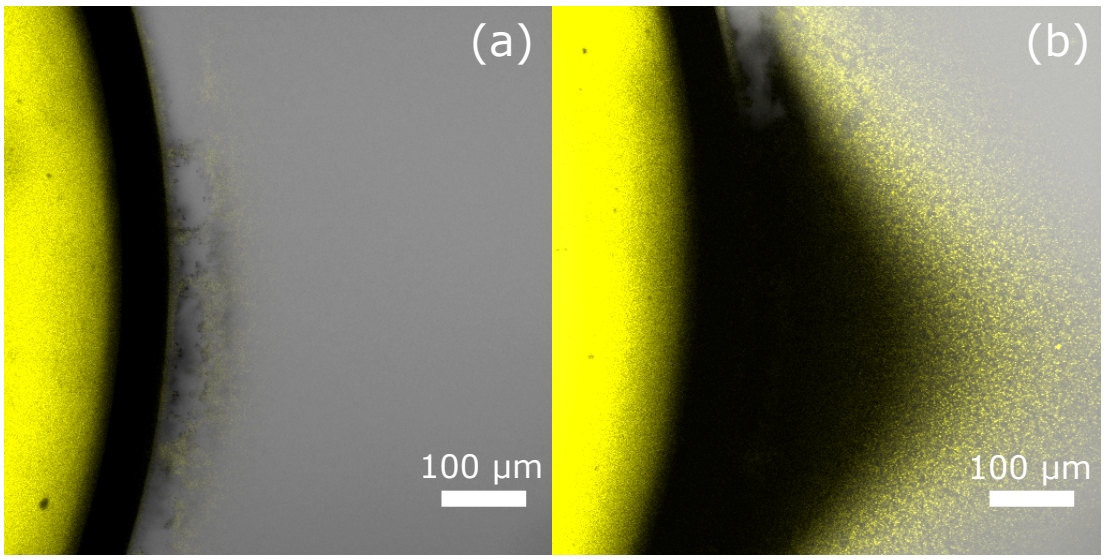

Figure 3.12 *(a,b) are composite images of the bright and fluorescent channel for a pure water-dyed drop, shortly after injection and 5 minutes later respectively. Dyed water can be seen flowing from the pure drop (showed in the image) towards a mixed drop to its right (out of view).*

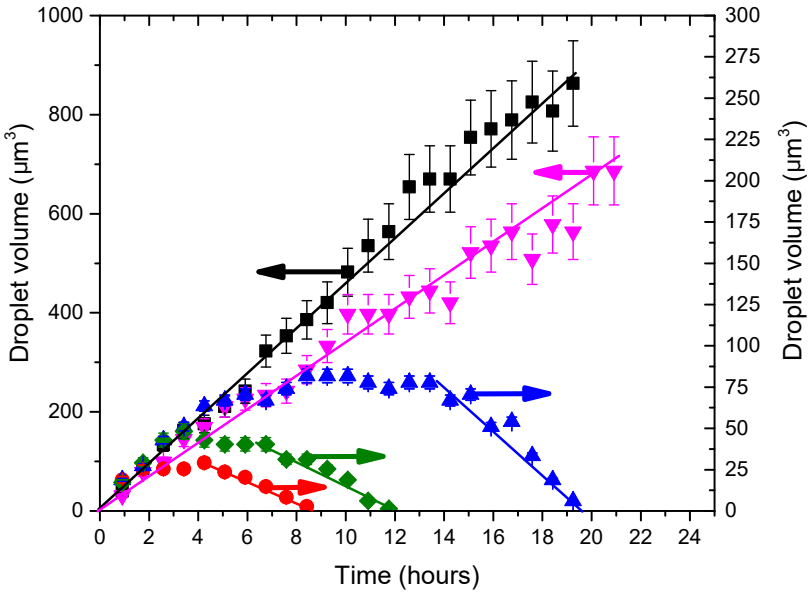

Figure 3.13 *Volume of five spontaneously formed droplets versus time. Two of them are ever-increasing (left axis), whereas the others experience a decrease at about 5 hours until they redissolve. Error bars represent the standard deviation for 3 measurements. Lines are a visual guide.*

For our experiments with standard compositions, careful examination reveals another phenomenon, which seems compatible with a phase separation process. Similar to the two-staged phenomenon reported for sessile electrolyte drops in

[98], two clearly distinct stages that create two different structures, delimited by yellow lines in Figure 3.14(b) are visible:

- First, a structure composed of concentrated and depleted layers, similar to that reported for spinodal decomposition in a confined geometry. [99]. It develops sooner and only extends over small distances ($\approx 20\%$ of drops' separation). The inset to Fig. 3.14 (b) shows a phase contrast image taken with a $\times 40$ objective which seems to confirm this hypothesis, as it highlights changes in the refractive index with a white halo, indicating in our case the existence of many newly created interfaces.
- Second, for longer distances there is a more gradually changing structure that develops all the way across to the other drop (as previously reported with both, the micro- and macroscopic approaches).

A first stage consisted of a fast formation of a water-rich layer around the drop, followed by slow diffusion-limited behaviour. The experimental formation time observed for the water-rich layer is approximately twice than the calculated value assuming growth by diffusion (using the model and the experimental values presented in Fig. 3.11) suggesting that molecular diffusion might not be the only effect taking place.

We know from our fluorescence observations, Fig. 3.14(a), supported by observations of Ostwald ripening, Fig. 3.13, that the particles do not become trapped on the interfaces of these droplets. Additionally, the static droplets are not necessarily in contact with each other, Fig. 3.8(a, b).

To ascertain the role of the particles in our system, we have studied the effect of the concentration of fumed silica particles on bridge formation, ranging from 0.0 to 0.2 vol.%:

- In the absence of particles, Fig. 3.15(a), droplets form but they are highly mobile. The motion takes the form of transient waves which are seen between the injected drops. These intermittent and short-lived (usually less than 20 seconds) waves of aggregated droplets seem to travel in the same direction as in bridging experiments, i.e. from the pure water drop towards the mixed one. In a period of 12.5 minutes at least three distinct temporary waves were observed.

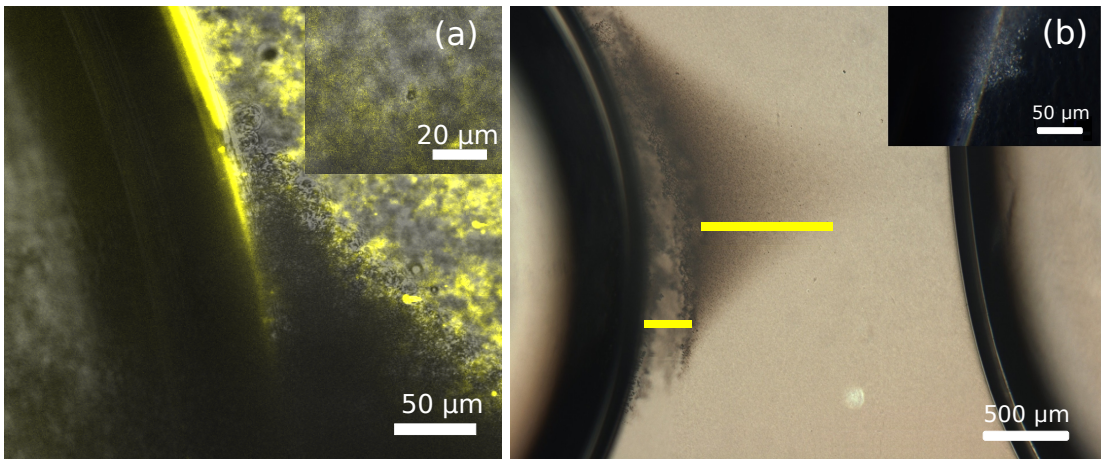

Figure 3.14 *(a) Overlay confocal microscopy image of the fluorescence and transmission channels showing the interface of the pure water drop. Standard compositions and procedure were used, with the addition of a small proportion (0.02 vol.%) of fluorescent silica. Coverage of the pure drop can be observed by the bright yellow lines, whereas the small droplets that form the bridge do not seem to exhibit any fluorescence. Inset: one of these droplets in the middle of the bridge. (b) Showing large-scale phase separation close to the drop and droplet formation further away. Inset: a ×40 phase contrast micrograph showing in detail the droplets formed close to the water drop interface.*

- Between 0.05 and 0.10 vol.% silica, the bridge forms and extends over roughly a quarter to a half of the distance between the drops, Fig. 3.15(b, c). This partial bridge remains stable over short times.
- At 0.15 vol.% silica, a bridge crossing the whole divide is formed, although it is considerably less populated by spontaneous droplets than for the standard bath composition with 0.20 vol.% silica, Fig. 3.15(d).

This dependence between the bridging distance and the fumed silica concentration in the bath suggests that the particles may be responsible for holding the droplets in place by modifying the surrounding medium. This is presumably due to the formation of a sparse network which prevents droplet motion. This has been further investigated through rheology measurements. Figure 3.16 shows a strain sweep at 1 Hz for our standard bath composition with and without silica particles. With particles, a linear viscoelastic behaviour for strains up to 10% is observed, with the storage modulus (G') dominating the loss modulus (G"). However, if no particles are present, the loss modulus dominates as for a liquid.

This supports our previous comments about the bath hindering the movement of

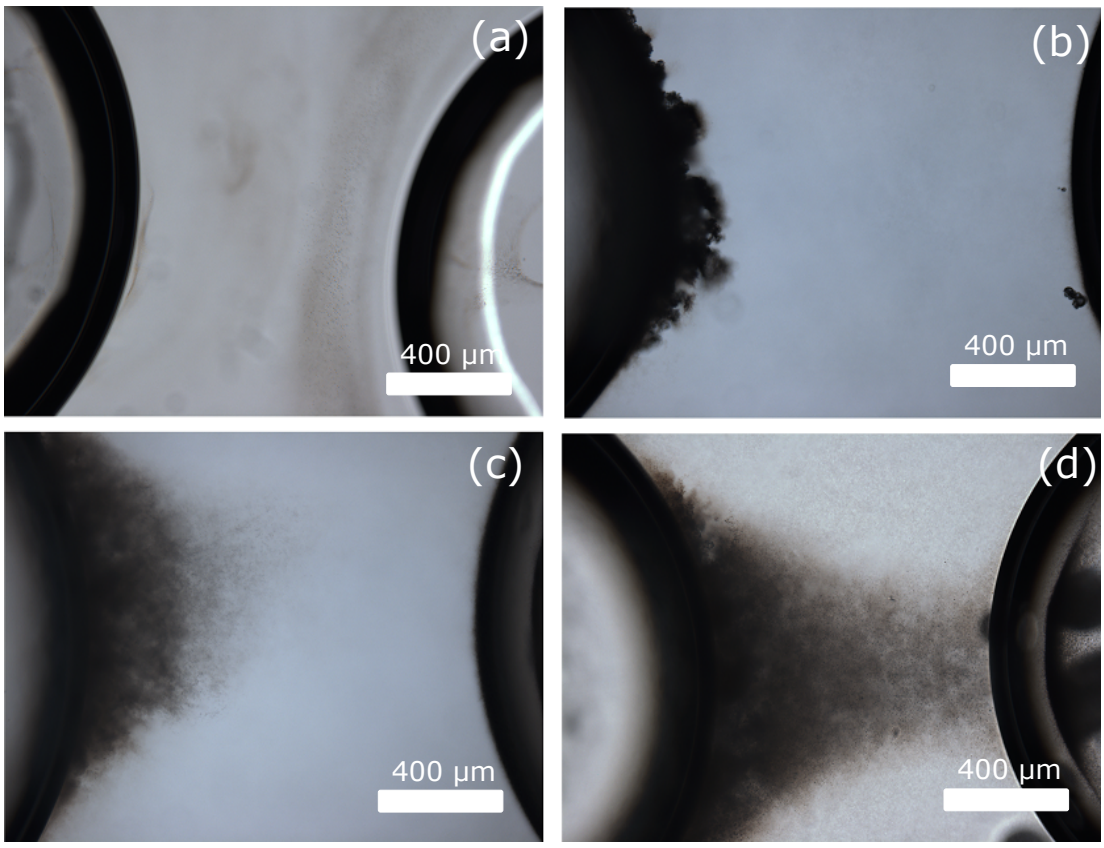

Figure 3.15 *(a-d) Effect of varying silica particle concentration in otherwise standard bath compositions. As vol.%, (a) is 0, (b) is 0.05, (c) is 0.10 and (d) is 0.15. Frames captured 10 minutes after injection, except (a), which shows a transient wave formed by droplets that only lasts around 20 seconds.*

the spontaneously formed droplets. It also agrees with the reported relationship between the amount of particles and the distance the bridge extends in Figure 3.15.

For our current explanation to hold, the ethanol concentration in the mixed droplet must remain roughly constant in order to keep a concentration difference that drives the bridge formation. If this holds then our system's behaviour is a variant of compositional ripening. Water and ethanol concentration in the center of each drop has been determined using Raman spectroscopy. The experiments were performed as a function of time switching the position at which the laser was focused from one drop to the other. The results for short times (up to 35 minutes) are presented in Figure 3.17. Time zero in the graph refers to the measuring time. There is a ∼2 minutes delay between the injection and the measurement. The legend refers to the drop in which it was measured either Pure or Mixed, for its initial state before injection (100% distilled water or 50/50 %vol ethanol/water),

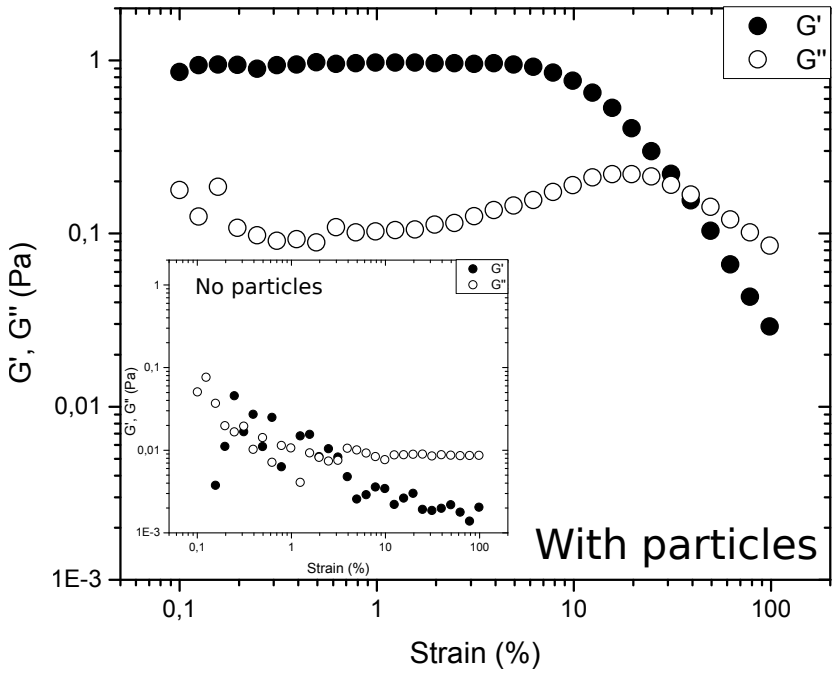

Figure 3.16 *Strain sweep performed at 1 Hz for our standard bath composition. Inset: Strain sweep for the same bath composition without particles.*

followed by the measured component (either ethanol or water).

Both drops seem to follow the same trend, decreasing the water concentration and increasing the ethanol one. For the mixed drop, the ethanol concentration increases only slightly from 54±3 to 60±2 %, supporting our assertion about the mixed drop. The main difference between drops is the magnitude of their change. For the pure drop its compositions are modified by nearly 20 %, whereas for the mixed drop there are only minor adjustments, with differences close to 6 %.

Although Raman spectroscopy allowed us to measure relative concentrations, the total volume of the drops is also an interesting factor to know. Figure 3.18 shows the total volume for the two injected drops over a period of 24 hours. The volume for each drop was obtained by fitting their interface to a circle to obtain the perimeter, which gives the diameter. As the diameter was always bigger than the cuvette height (1 mm), a cylindrical shape was assumed. The values have been normalized to 1, dividing by their initial volume. The first point for each drop has been slightly shifted to be visible in the Figure. We can observe how the initially pure water drop increases its volume substantially, by around 75%. This is easily explained with reference to the phase diagram [15] of our system, which indicates expansion shall be expected, as ethanol goes into the drop. For the initially mixed drop, the changes in volume are rather small, decreasing about

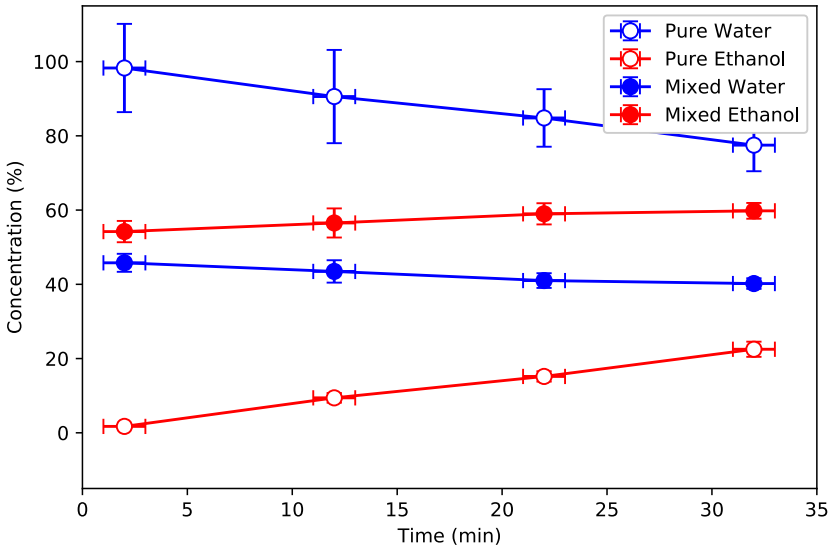

Figure 3.17 *Composition of the pure (hollow) water and 50/50 vol.% water/ethanol (filled) drops for short times (30 minutes) determined with a Raman spectrometer. Error bars indicate repeatability error.*

15%. This agrees with our postulate that the ethanol concentration, and therefore volume of the drop must remain stable. Therefore, it has been proved with the Raman compositions and the volume of the drop that it is indeed the case, and our explanation built on the ternary phase diagram holds.

Bridge formation at different stages over 24 hours is shown in Fig. 3.19(a-d). As reported and explained previously, initially the bridge grew from the pure water drop towards the mixed drop; spontaneously formed small droplets are observed in the usual way, Fig. 3.19(a). Surprisingly, after a few hours, a large amount of droplets could be observed inside the mixed drop, Fig. 3.19(b). These droplets form slightly later than the bridge itself and in a smaller quantity, being much more mobile than the ones in the bath. Even more surprisingly, after ~6 hours another stream of small droplets is observed within the left-hand drop (pure water drop) moving away from the interface, Fig. 3.19(c). After 24 hours, Fig. 3.19(d), and although the bridge is thinning progressively we can still distinguish droplets inside both drops.

The streams of small droplets inside the injected drops may be explained by the changes in drops' compositions that occur steadily by diffusion. The drops' composition over time for long periods (24 hours), which were obtained through Raman spectroscopy, has been included in Fig. 3.20. The initially pure water drop has taken in ethanol from the bath (and a very small amount of toluene, which cannot be measured due to an overlap between the Raman characteristic

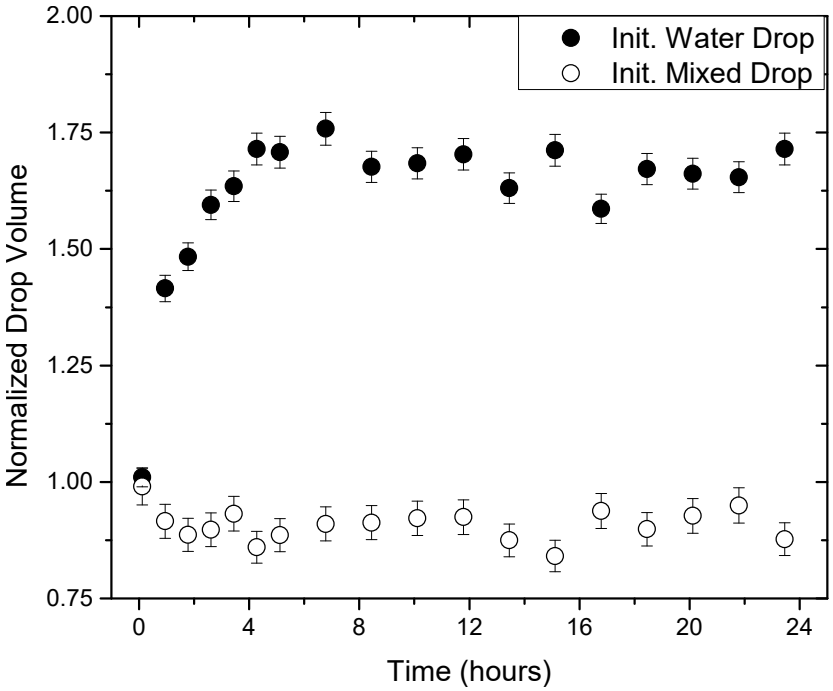

Figure 3.18 *The volume for each drop was obtained at different times by fitting the interface to a circle to obtain the radius. Assuming cylindrical shapes, as the diameter was greater than the cuvette's height, the volume was then determined and divided by its initial value. Error bars indicate repeatability error.*

peaks for toluene and ethanol around 3000 cm^{-1}) and will eventually begin to behave like the initially mixed drop. The mixed drop changes its composition only slightly, remaining fairly constant (a maximum of 6% change during the first hour was observed, with a further 6% over the remaining 23 hours), which is in agreement with our hypothesis for short times, which required a constant amount of alcohol in this drop. Both drops achieve the same composition after ~7.5 hours, which is about the same time at which a small stream of droplets appear inside the initially pure-water drop. This secondary droplet production reduces over time, although it is still visible after 24 hours.

A tentative explanation for toluene-rich droplet production inside the mixed drop at short times, and inside the pure drop after a long period of time can be found by studying the ternary phase diagram. At short times, there is a certain amount of toluene diffusing inside the mixed drop, according to Fig. 3.9 (c). Due to the same diffusion and stranding mechanism that creates the water-rich droplets in the bath, it is also possible to have toluene-rich droplets inside the aqueous domain. As the mixed drop composition evolves, which in the ternary diagram is represented as moving from the water/ethanol axis towards the binodal line,

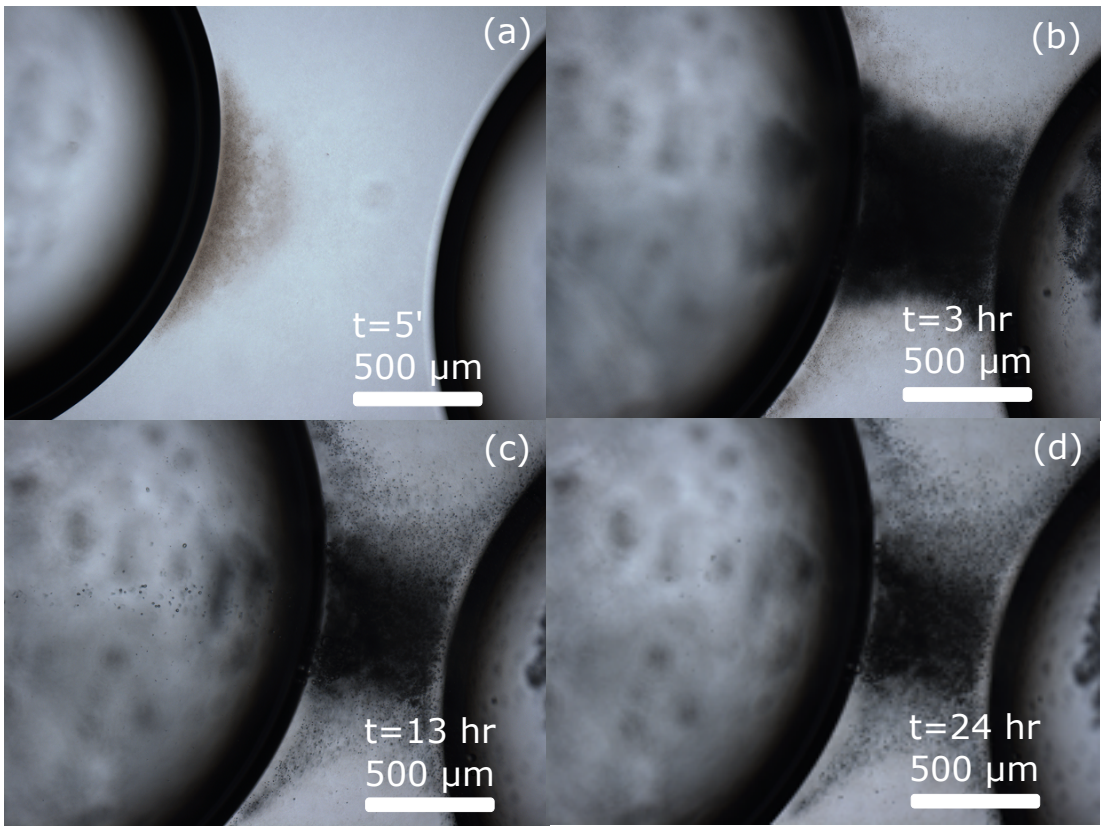

Figure 3.19 *(a-d) Bridge formation over long times. Frame (a) shows the initial stage; (b) shortly after injection droplets are observed inside the mixed drop (right) and start to agglomerate until ; (c) finally, droplets are also observed within the water drop (left) and disappear from the mixed one; (d) for longer times the bridge starts to thin, due to droplets redissolving in the bath*

the amount of toluene diffusing inside the drop increases. In Fig. 3.21 (a) we can observe these spontaneously formed droplets inside the initially mixed drop. They are first observed a few minutes after injection, with its size evolution over time following Ostwald ripening, which due to differences in size between droplets drive growth from the smaller towards the bigger droplets. In some experiments, a structure through which a stream of droplets can be seen penetrating the drop has been observed, and has been included in Fig. 3.21 (b). This exact same phenomenon occurs at long times (several hours) at the initially pure water drop. As its composition evolves to resemble a mixed drop (after all, they are trying to achieve equilibrium by attaining the same composition), toluene is able to start diffusing into the drop the same way it happened in the initially mixed drop. The influx of toluene will create supersaturation zones from which nucleation of toluene-rich droplets is possible.

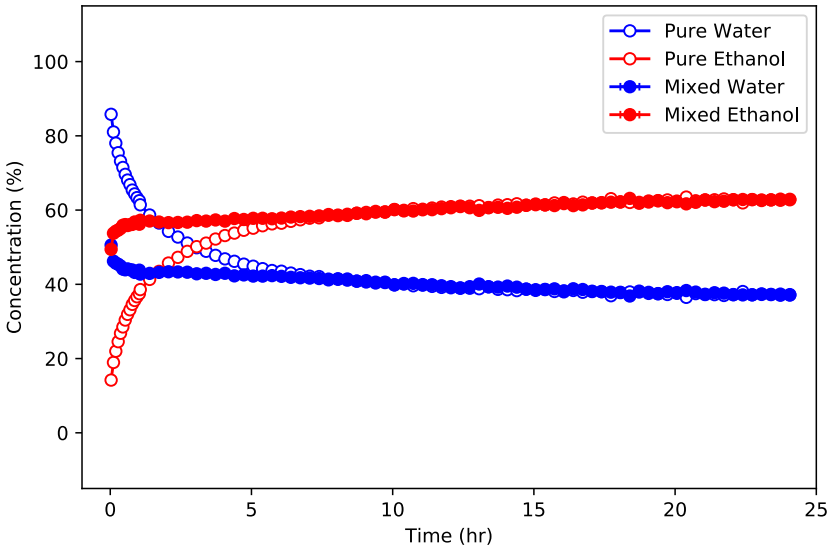

Figure 3.20 *Drops' composition evolution for long time experiments (24 hours) obtained with the Raman spectrometer. In the legend, pure refers to a 100% water drop (hollow), and mixed to a 50/50 vol.% (filled) water/ethanol drop.*

Compound	Surface tension with air (mN/m) [101]	Dynamic Viscosity at 30°C (mPas) [102]
Toluene	28.4	0.53
Ethanol	22.1	0.98
Water	72.8	0.80

Table 3.1 *Surface tension and dynamic viscosity values for toluene, ethanol and water.*

We believe these oil in water (O/W) droplets (toluene-rich inside the aqueous drops) follow a solutal Marangoni flow that occurs at the vertices from which the droplets originate. If the diffusion of water into the oil ($D_{W/O} = 6.19 \pm 0.05$) is faster than diffusion of oil into water ($D_{O/W} = 0.85 \pm 0.03$) that would explain why on our standard experiments the "bridge", made up of water in oil (W/O) droplets, is observed rather sooner than the (O/W) droplets inside the drop. According to Gouda [100], interfacial instability will occur if the solute reduces the interfacial tension and the diffusion takes place from the more viscous to the less viscous phase. This is indeed the case if ethanol is diffusing from the mixed drop (high viscosity due to its aqueous component) to the bath (where the main component is toluene). For numerical values please refer to Table 3.1.

Another possible explanation for the creation of these toluene-rich droplets is by means of the low-tension interface mechanism for spontaneous emulsification. If the composition is, if only transiently and at random spots, near the critical point,

the surface tension at that point will be negligible. This would allow an inflow of toluene into the droplet, which may start to nucleate into droplets inside injected drop. This phenomenon plus the poor coverage of the drop surface by the silica particles plus the Marangoni effect may create a spot where the spontaneous emulsification of toluene-rich droplets is enhanced. Please refer to Fig. 3.21 (c) for a graphical explanation.

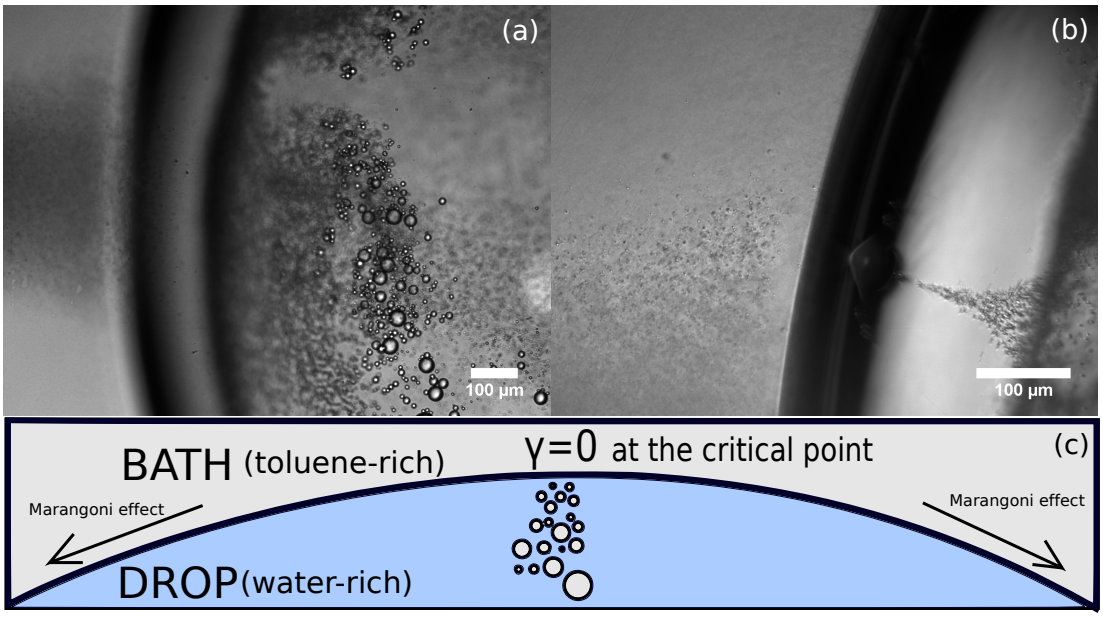

Figure 3.21 *(a) Spontaneously formed toluene-rich droplets inside the initially mixed drop are shown, at a slightly different focus from the rim. (b) A kind of "vortex" through which droplets appear to enter the drop, although they are nucleating across it, probably due to a stream of solvent. (c) A cartoon depicting a possible explanation using Marangoni effect to describe the nucleation of droplets.*

When comparing our findings to a study (Chapter 4 in [103]) where they used water/ethanol drops injected in anethole oil, we find a good agreement in the main points of our works. They do observe both, (O/W) and (W/O) emulsions:

- In their study, the (W/O) emulsification appears less than 5 seconds after injection, although only for high alcohol content drops ($\geq$ 50% vol.). About 30 seconds after injection, the (W/O) emulsification disappears. In our experiments, we would also observe the emulsification shortly after injection, although in our case it does not disappear, but remains over a day, forming a "bridge". This can be explained by the presence of fumed silica particles, which gelates the bath halting the coalescence between droplets.

- About the (O/W) emulsification, they found that it is present preferentially

at the mid of the drop, independently of the ethanol concentration of the drop. Emulsification will occur at later stages and will cloud the drop, giving it a milky appearance. In our case, we found that these (O/W) droplets appear from vertices and move inwards trying to reach the center. They also appear significantly later than the (W/O) emulsions.

Another feature of our system for long times is the "thinning" it suffers, observed as an increase in the brightness transmitted through the bridge. This was also the case for our 3D configuration after breaking the bridge by increasing the separation between drops, shown in Fig. 3.5 (h). The grey value along a line connecting the two injected drops at 3, 13 and 24 hours has been collected in Fig. 3.22. Zero distance is situated within the pure water drop. In this figure, high grey values indicate whiter areas, whereas low values are characteristic for dark zones. The bridge is contained in the valley between the outermost peaks, which represents the interface of each drop. The mean grey values at increasing times (0.5, 13 and 24 hours) are 11.2, 15.7 and 20.0, respectively. This value could be seen as an indicator of the amount of droplets forming the bridge, and the decrease is likely to be due to droplet ripening and coalescence leading to a decrease in the density of liquid-liquid interfaces.

3.4 Conclusions and future work

We have demonstrated that a composition gradient between two injected drops, in a ternary liquid system containing nanoparticles, can create a new self-assembly process. The gradient drives the diffusion of water between the two particle-stabilized drops; the resulting change in the composition of the bath phase leads to the spontaneous formation of a large population of tiny droplets.

So far, this is a description of a variant of compositional ripening. However, in the presence of silica nanoparticles, the droplets aggregate in the form an elastic "bridge" along the path connecting the two drops. This bridge extends over time with a diffusivity (D=10^{-5} cm^2/s) similar to the values obtained for the diffusion of small molecules. Particle concentration in the bath determines the extension of the bridge, ranging from no bridge to a fully developed bridge, for values between 0 to 0.20 % in volume. Using rheology measurements we discerned that the particles are able to gellate the bath, inhibiting the movement of droplets.

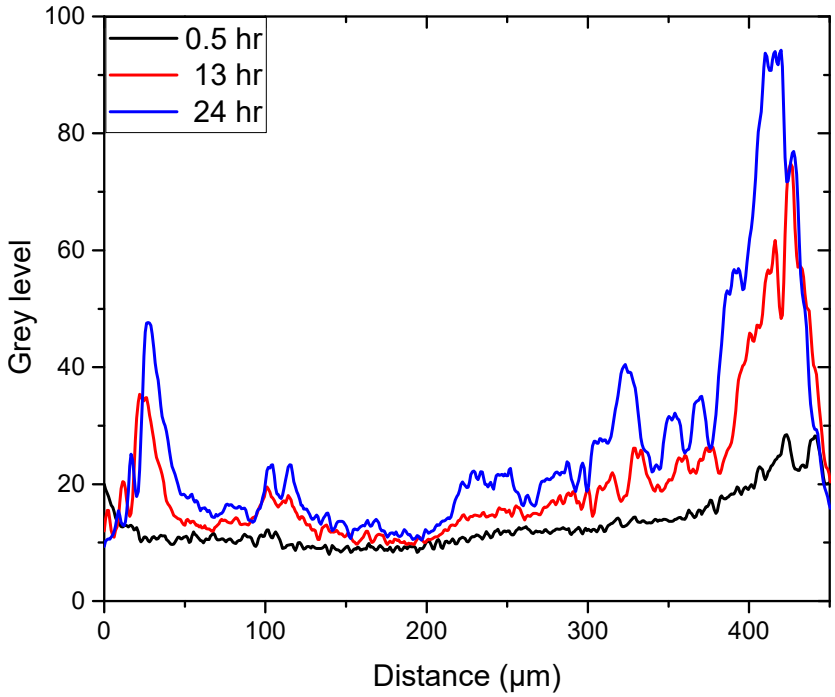

Figure 3.22 *Mean grey value obtained across a line across the bridge at three different times, depicted in Fig. 3.19. The sharp peaks at both edges delimit the bridge. Due to the small movement of the injected drops the boundaries shift slightly towards shorter distances.*

We note, however, that the silica nanoparticles do not appear to be adsorbed to the droplet interfaces. Ostwald ripening drives the temporal evolution of the droplet sizes within the bridge; coalescence is also seen. Confocal microscopy using fluorescein dyed water drops confirmed that the diffusion of water is the main drive for the formation of the bridge.

Using Raman spectroscopy, the composition of both drops were followed over time. They reached equilibrium roughly after 8 hours, achieving an alcohol/water ratio of 60/40 % in volume. This produces a swelling of about 175% for the initial pure water, with a decrease of nearly 15% volume in the mixed drop. After approximately four hours, the initially pure water drop becomes more alcohol-rich than the initially mixed drop. This provokes a reversal in the direction of the flow, which becomes fainter over time, leading to a progressive thinning of the bridge as the non-particle covered droplets redissolve into the bath.

Careful observations, especially at later times, reveal a zoo of subsidiary phenomena. A phase separated boundary layer is found close to the pure water drop on a $\sim 100\,\mu$m scale for standard bath compositions. The spontaneous formation of oil-rich droplets is also found inside the injected drops.

Future work to complement the study presented here may include:

- The use of different gradients (throughout our study we employed a 100/0 and 50/0 %vol H2O/EtOH compositions) may be a useful route to study the role the compositional gradient has on the dynamics of the system.
- The use of different particles, particles size and its surface composition may reveal concealed effects regarding the bridging phenomenon. For example, smaller or more hydrophilic particles may produce more efficient coverage of the interfaces, resulting in slower diffusion of water and more stable spontaneously formed droplets.
- The use of a different oil in which this phenomenon is still present can enable the use of Raman spectroscopy to follow the bath composition at different points (to track the diffusion of methanol in the bath) or evaluate the amount of oil inside the drop to confirm mutual solubility values in the literature. This may also be achieved by devising some alternative way to measure concentrations where signal overlapping does not occur.
- Rheology studies on aging bath solutions may prove useful to explain some of the effects we observe at later times, as well as to quantify the gellation of the bath.

Chapter 4

Study of alcohol influence in the methanol/toluene/water system

4.1 Introduction

As in our previous chapter, in this study our main motivation is to successfully employ ternary diagrams with calculated diffusion paths to explain our experimental observations. The ever increasing importance of new materials, which are becoming more and more specific and are synthesized through more complex processes, along with the necessity of more efficient and eco-friendly formulation routes, makes it necessary to achieve a deeper understanding of the diffusion dynamics in systems which are more complicated than binary mixtures. That is why the ability to predict the behaviour when contacting two phases becomes crucial. For example, this is the case when you need to dilute a concentrated solution, whether it is a cleaning product, an agrochemical element or a food compound, for it to be used.

In the last chapter, we focused our attention into a very peculiar phenomenon observed when employing a certain set of specific experimental conditions. These conditions were a particular bath solution which would gel easily, an alcohol content high enough so miscibility was improved and the existance of an alcohol gradient between the injected drops which would induce a compositional gradient of water diffusing out of the lower alcohol-content drop. This would produce the spontaneous emulsification of thousands of tiny water droplets according to the

"diffusion and stranding" working mechanism for spontaneous emulsification. [55] This "tailored" system permitted us to gain insight into the different types of phenomena that may occur in this type of systems, and to obtain the most complete picture as possible we performed very different experimental techniques. These types of system, which have been used throughout all this thesis, have been used abundantly to study spontaneous emulsification, [15, 28, 38, 55, 87] along with the Ouzo effect, [39, 42, 44, 59–61, 80] where a system made of trans-anethole oil, water and ethanol displays metastability when displaced from the binodal, and whose ternary diagram is very similar to our systems of interest.

The initial study of the influence of different alcohols on the diffusion behaviour of injected water drops, [87] motivated a more in-depth investigation into the relationship between the systems' ternary diagrams and our empirical observations, with an interest in furthering the knowledge of the role the tie-lines associated with the diffusion path have on the overall diffusion behaviour. In contrast to Chapter 3, this chapter focuses on single drop experiments in order to minimize the existence of compositional gradients that occur between different drops.

This drop will be, as in previous experiments, immersed in a bath composed of a mixture of oil, alcohol and gelling particles. These particles will cover the surface of the injected drop, becoming trapped at the interface. Such a layer of particles increases the compressibility of the interface, contributing to the interfacial elasticity of the drop. Lateral particle-particle and particle-interface interactions (electrostatic, van der Waals, capillarity, etc.), dependant on the surface chemistry of the particles, induce surface stresses, the macroscopic observation of such interactions. [104] These stresses will control the mechanical properties of the composite interface. After relaxation, the particles will redistribute on the surface to experience zero tangential forces. [105]

Interfacial elasticity allows the drop to better withstand the effects of gravity (for example on a pendant drop) or to increase its volume when experiencing a homogeneous dilatational deformation, as in our experiments. Pendant drop measurements usually fit the Young-Laplace equation using the shape of the suspended drop. Its shape is determined by the gravity force and the surface tension, which should be at equilibrium for a stable drop. There is controversy about whether particles at the liquid-liquid interfaces modify its interfacial tension or not. Although for micron or large nanoparticles it is generally accepted they do not affect interfacial tensions, [106–108] for small nanoparticles (<20 nm)

there are a number of studies both disregarding [109, 110] the hypothesis of the particle influence on interfacial tension, or supporting it [111–113].

For large surface particle coverage, or very weak particle adsorption there is the possibility of particle detachment from the interface, [105] contrary to the experimental observations in Langmuir troughs where rafts of particles did not expel particles, but rather buckle under compression forming wrinkles or folding. [114]

The time evolution of the drop was also studied using solvatochromic dyes, where no particles were added to the bath, as they may suppress the movement of the dye. The presence of nanoparticles in conjunction with solvatochromic dyes was able to quench fluorescence [115] or form dye aggregates, which depending on the dye's concentration may or may not be fluorescent. [116] These dyes can be used as sensitive probes for different solvents, as they are able to change colour according to changes in the polarity of their vicinity. They are usually push-pull molecules, meaning they have donor and acceptor parts, and their emission shifts to the red in more polar solvents if they are positively solvatochromic (bathochromic), like Reichardt's dye and Nile Red. [117]

The use of these dyes create very striking and visually appealing experiments where the diffusion of different components may be followed just by looking at the colour changes each phase experience. The colours can then be matched with a previously obtained "calibration" palette to determine the evolution of the system. Special care needs to be taken when choosing the appropriate dye, with a wide variety of colour changes with each of the components present in the system, in order to clearly identify each colour change with each diffusing solvent.

There is a rich literature about the use of "clever" droplets. Initially originating from the idea of mimicking biological processes, there has been a huge success in producing moving droplets responding to different stimuli, such as chemotaxis, phototaxis or a combination of both. With smart experimental designs, droplets were able to propel themselves forward due to Marangoni flows arising from surface tension inhomogeneities. Herminghaus et al. [118] describe how interfacial tension gradients can induce a viscous shear flow in the solution, which produces a pulling movement at the interface towards higher values of interfacial tension. With a simple scale analysis of the capillary velocity, the quotient between usual interfacial tension values (several mN/m) and the viscosity of usual oily solutions (several mPas) yields speeds of meters per second, thus achieving large speeds

with small Marangoni flows. One of the simplest mechanisms to induce motion in a drop, similar to the movement of a squirmer (spherical microbe with a cilia), arises from a non homogeneous process that creates differences in the surfactant layer around a drop. The Marangoni flow created by such differences brings fresh surfactant to the low surface tension areas, thus maintaining the difference and creating a directed gradient towards the depleted surfactant zone (see Figure 4.1).

Using these type of mechanisms, either with pH gradients [119] or surfactant gradients [120, 121] experiments as amazing as maze solving droplets [122] can be produced. Using molecules that experience conformational switching upon irradiation, such as changing from trans to a cis structure, create a heterogeneous surface distribution when the light was non uniform, thus creating a wettability gradient that made the drop follow the light beam. [123] Both of these phenomena were combined, producing chemical changes in the composition when exposed to light. This is the case when a bath solution able to change its pH upon irradiation is used in conjunction with a droplet that reacts to pH changes by redissolving partially. This modifies the surface tension of the interface in a non homogeneous way, producing a Marangoni flow. [124]

There are more elaborated setups involving the use of magnetic particles, such as infusing magnetite into porous silicium particles. These particles attached themselves to the interface of a water droplet in an oily bath, allowing the drop to be moved by external magnetic fields. [125] Marbles produced with similar particles were able to reach high velocities (30-50 cm/s) and even expose some area of the aqueous domain under strong fields. [126, 127] Movement of droplets has also been achieved by a clever design of the substrate. Substrate thickness' differences introduce a stiffness gradient that, when a drop is injected, produce different contact angles that will be able to produce movement. [128] Topography with different micropatterns can also induced either a Fakir or Cassie sate, where air pockets situated under the drop force it to bead up, increasing the contact angle. [129] The Leidenfrost effect, where an increase of temperature to the boiling temperature creates a thin vapor layer that lifts the drop, facilitating its movement. [130]

Once the movement of the droplets has been achieved by a number of different processes, another biological process of special interest is replication. It has also been accomplished in different systems, but usually micelles and surfactants play a huge role. One of the first successful experiments [131] involved an aqueous drop with surfactants octanoic acid sodium salt (OASS) and LiOH immersed in

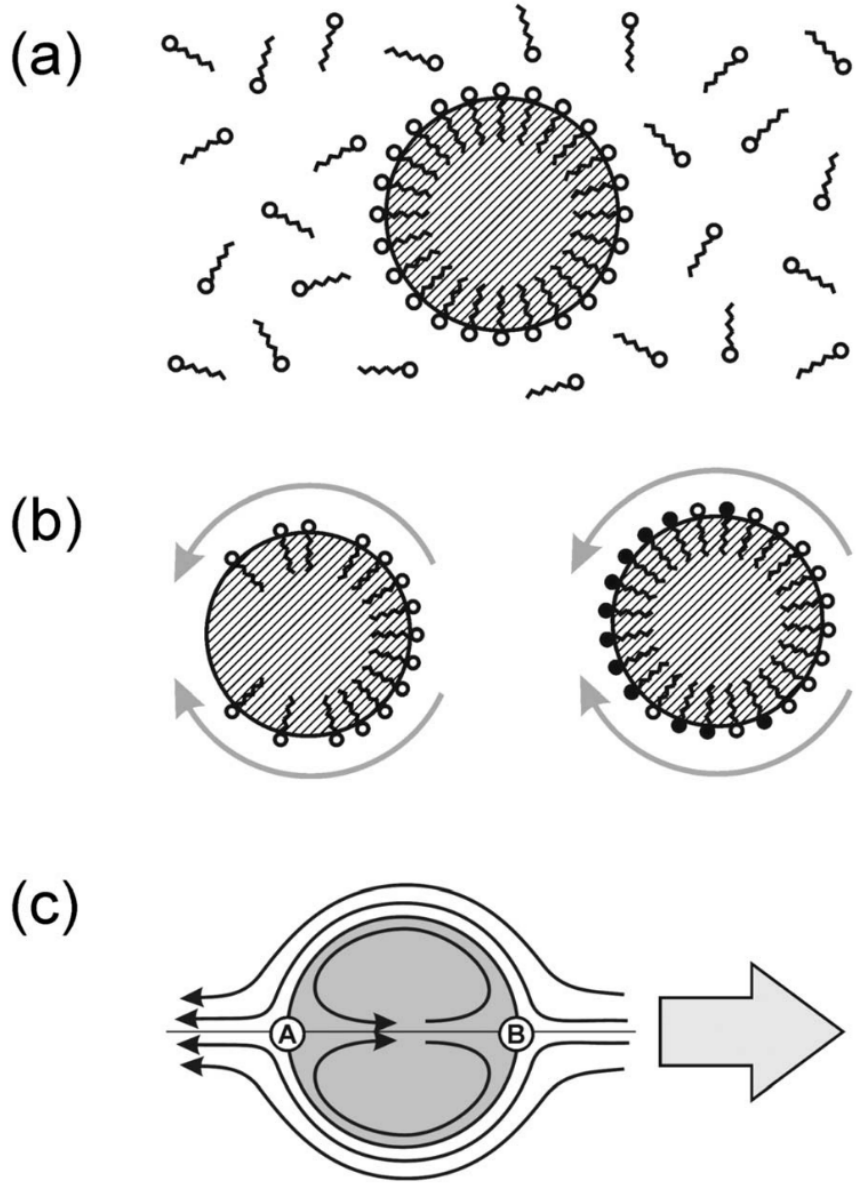

Figure 4.1 *(a) Surfactant molecules in the bath and adsorbed at the interface, reducing the interfacial tension. (b) Two different ways to produce Marangoni stresses in the direction of the arrows, either with an inhomogeneous density or with a chemical reaction that modify only some of the surfactant molecules. (c) Marangoni flow in the direction of the black arrows, with the droplet moving towards the big grey arrow. New surfactant molecules only reach point B, maintaining the movement. Image taken from [118]*

an isooctane/1-octanol mixture. Octanoic acid octyl ester located in the bath was catalyzed at the surface, producing (OASS) and 1-octanol. To accomodate this surfactant excess, the micellar drop broke down into smaller micelles. They were able to replicate this type of experiment using double-layered vesicles. [132]

Szostak and his group performed experiments to gain some insight into whether mineral particles and micelles could be vesicle precursors in life. They observed that clay particles acted as a catalyst, greatly increasing the rate of vesicle formation. [133] They demonstrated how upon the addition of excess micelles, some vesicles formed elongated structures that broke into smaller vesicles upon agitation. [134]

Lastly, the work of Cronin et al. developing a method of "natural evolution" upon an ensemble of droplets is worth mentioning. They used four different chemical compounds, which would be the different genes, to try and obtain the best performing combination of "genes" at three different activities, such as movement, replication, and vibration. They were able to map several ternary diagrams with the performance of each composition evaluated for each of the different activities, resulting in a selection of the better performing compositions for each task. [135]

The work presented in this chapter offers an innovative way to relate experimental diffusion (and spontaneous emulsification) observations in ternary systems with their ternary diagram, while also making use of solvatochromic dyes to provide a very simple way to identify which components are diffusing into which phase.

4.2 Experimental methods

In most of the experiments, a 9.6 mL Krüss SC01 cuvette was employed, whereas a 1 mm path length optical cuvette from Starna Scientific was used for the Raman measurements and dye experiments. The standard procedure was the same than in the previous chapter - filling a cuvette with a known bath composition and injecting different composition drops to record its time evolution. The bath solution was prepared using toluene (Sigma-Aldrich, $\geq 99.7\,\%$), methanol (Sigma-Aldricht, $\geq 99.8\,\%$) and fumed silica particles (HDK H30) with a cluster size $\approx$100 nm, which were a gift from Wacker-Chemie (Burghausen). The usual bath composition was 77.5 % toluene, 22.5 % methanol and 0.2 % silica in volume. The hydrophobic silica particles were dispersed in the bath using an ultrasound probe (Sonics Vibracell VCX500) for a total time of 2 minutes, using a 20 seconds on/off configuration with an amplitude of 20%.

The experimental control parameters were the alcohol concentration in the

injected drop for the expansion studies, and the silica amount in the bath in the Raman research.

In the expansion studies, a ≈20 μL drop was carefully injected using a Hamilton gas-tight #1750 syringe and a Krüss steel needle of 1.8 mm diameter at the bottom of the cuvette. Its time evolution was recorded using an Allied Vision Stingray F-046 camera (mounted on the Krüss EasyDrop apparatus) for about two hours recording a frame every five seconds. The images captured were then treated using the software Fiji [96]. The images were transformed into a binary picture, and the substrate removed, obtaining a clear image from which the projected area of the drop was measured.

For the Raman and dye studies a Hamilton Microliter #702 syringe with a Hamilton steel needle of 0.72 mm diameter was used to inject drops ≈5 μL, capping the cuvette afterwards to avoid evaporation. Raman experiments injecting only a single drop were performed under the same conditions described in the previous chapter. A typical Raman spectrum obtained in this system is shown in Figure 4.2 (a), with the calibration curve used afterwards to obtain relative concentrations included in Figure 4.2 (b).

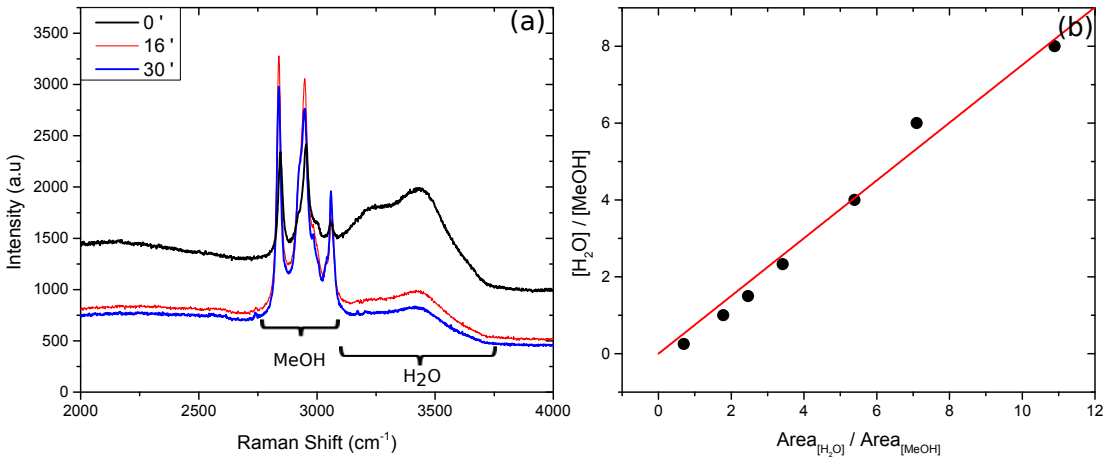

Figure 4.2 *(a) Raman spectrum at the center of the pure water droplet at three different times, indicated in minutes. The spectra have not been offset. For each component the range of Raman shift integrated for each component is indicated by brackets. (b) Calibration curve used to transform the Raman spectra into concentration ratios, which were translated into individual components. Fitted slope is K=0.75± 0.03.*

In the dye experiments, a solvatochromic dye (either Reichardt's dye (Betaine 30) or Nile Red, both supplied by Sigma-Aldrich) was added, as 0.02% weight, to the methanol used later in the bath solution and vortex-mixed for 1 minute. Then, in

the same experimental setup as the one used in the Raman studies, a pure water drop was injected into a standing thin cuvette. Its time evolution is recorded with a MicroPublisher 5.0 colour-camera coupled with the Krüss EasyDrop apparatus, saving a frame every three seconds.

4.3 Results

We consider this system to be very similar to the one we have explored in Chapter 3, replacing the ethanol by methanol. The phase diagram changes only slightly, with all the main features that we considered affected our experiments remaining fairly similar. Therefore, it is safe to assume that the silica particles in the bath rapidly cover the interface of the injected drop and that there will be an exchange of material between the drop and the bath, with the alcohol flowing inside the drop, and water diffusing out. To study the influence that the amount of alcohol has on the growth behaviour of a single water droplet we have analyzed about 30 experiments with varying methanol concentration in the injected drop. The droplet is placed in a cuvette filled with an oily dispersion of particles, whose composition was in all cases the standard one (described in the Experimental Methods section 4.2). As an example, three of these experiments have been included in Figure 4.3.

- For the pure water drop, we observe a steady increase in volume until its shape deviates from spherical after 45 minutes. Then it starts to sprout and overspill material to the bath, converting into a tubular shape which finally redissolves after 2 hours.
- As we increase the amount of methanol in the injected drop two changes become apparent. First, the maximum volume the drop is able to achieve decreases because it needs to incorporate less methanol from the bath to reach equilibrium. Second, it starts to sprout a tube sooner than in the previous case, as the amount of alcohol needed is reached faster because the initial amount is larger. The drop first experiences an isotropic expansion at early times and a tubular-shape expansion (at the middle of the experiment) is directed by preferential alcohol gradients, rather than the absolute amount of alcohol inside the drop.
- For higher amounts of alcohol, the drop starts to become less stable,

sprouting very fast and redissolving sooner, as it reaches equilibrium faster and is solubilized by the bath much more easily.

The spreading shapes extending from the drops at early and intermediate times are clouds of spontaneously formed water-rich droplets that will eventually redissolve. More about this can be found in Chapter 3, where it is thoroughly discussed.

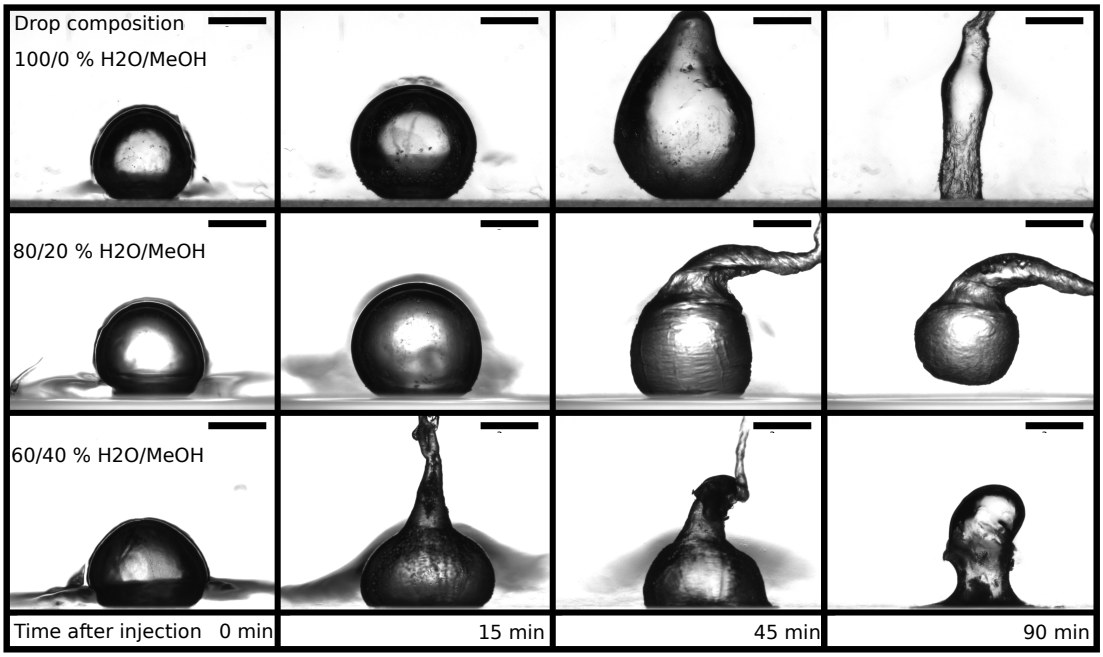

Figure 4.3 *A series of frames at different times for three different alcohol/water drop compositions. For the pure water drop, we observe a constant volume increase that is associated with a slow change from a spherical shape into a tubular one, with overspilling taking place. Over time the whole drop redissolves in the bath. As we increase the amount of alcohol in the drop, the maximum volume the drop is able to achieve is reduced, as there is now less alcohol flowing inside. The change in shape and overspilling also occurs sooner as the amount of alcohol needed inside the droplet is achieved faster. The black "ribbons" that extend from the drops are clouds of spontaneously formed water droplets created by the diffusion of water into the bath. Scale is 2 mm.*

Another relevant feature is the fact that any overspilling from our drops is always upwards, which differs from the ethanol system where high amounts of alcohol (above 20%) would lead to overspilling downwards, adding to a rich state diagram [87]. This difference and the observation of a floating drop, as shown in Figure 4.3 (second row, last column), can be explained by the density changes the drop experiences as its composition varies. Due to the bulk nature of our

bath we can consider its density value as stable over the whole experiment, with a value close to 0.9 g/cm^3. However, any increase in the amount of alcohol in the drop will decrease its density linearly. As the drop composition evolves towards the equilibrium composition, we can distinguish two different behaviours, which agree with what we have observed experimentally.

- For the methanol system, our Raman experiments (described in detail later on) yield a very high alcohol content (about 85%) inside the drop at late times. Therefore, when our drop has a density lower than the bath it will float upwards.
- In the case of ethanol, the amount of alcohol inside the drop at the equilibrium is considerably lower (about 40%), therefore being always heavier than the bath, impeding the flotation.

These explanations have been collected graphically in Figure 4.4, indicating both the initial and final compositions of the drop, as well as colour-coding as red those cases where the drop will sink, and blue for those when it will float. Although this explanation indeed addresses the experimental differences observed, there are other reasons as to why the sight of a floating drop is a rare occurrence in our experiments. Firstly, the buoyancy of the drop is hindered by the gelation of the bath caused by the sedimentation of the sticky silica particles. Secondly, these particles also act like a "glue", fixing the drop interface to the cuvette floor.

From these experiments, analytical data to represent the volume changes (measured as the area of the drop in the image) as time progresses was obtained. For the experiments represented in Figure 4.3 the corresponding data is shown in Figure 4.5. This representation of our experiments allows us to determine and compare different important values, such as the time at which the drop reaches its maximum value (which we have called "offset time") and starts to shrink redissolving into the bath, as well as the maximum volume achieved at that time.

As described when presenting the frames of the actual experiments, increasing the alcohol concentration in the injected drop results in lower offset times and maximum volumes. We have analyzed drops ranging from 0 to 50 % methanol in volume. For values above this threshold the drop redissolves immediately after contacting the bath.

In comparison with other dissolving experiments, in particular water/ethanol drops injected in an anethole bath [103], we find that the presence of alcohol in

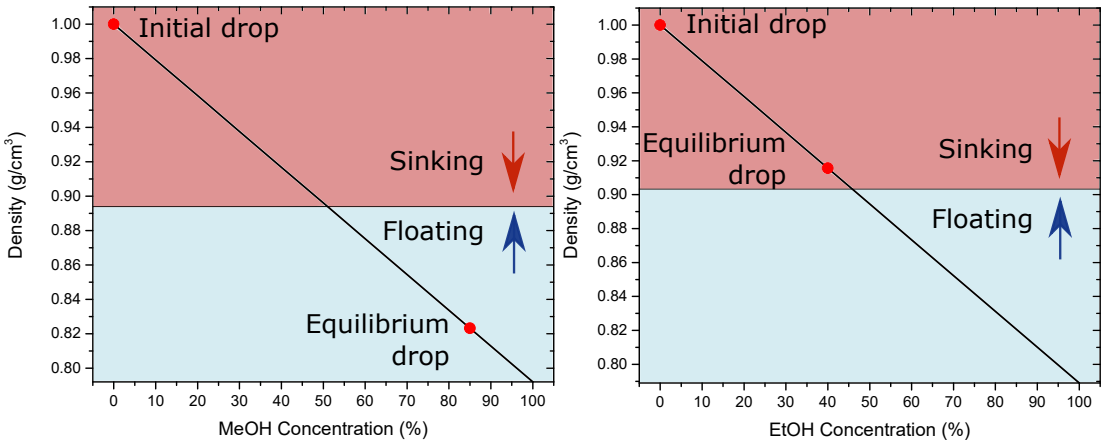

Figure 4.4 *Density as a function of the amount of alcohol (methanol on the left, ethanol on the right) in the injected drop is plotted as a black line. The initial and final (termed as equilibrium) drop densities have been included as red filled circles. Bath density is indicated as the dividing line between the coloured-backgrounds. As the alcohol content increases inside the drop, its density decrease until it reaches the equilibrium composition. Drops will sink when its density is higher than the bath's, indicated by the red-coloured background. On the contrary, they will float upwards if they are lighter than the bath, shown as blue-coloured background. For the methanol system, we observe that it is indeed possible to observe drops rising up. However, for the ethanol system flotation will not happen as its equilibrium composition density is higher than the bath's, not being able to reach the blue area.*

our bath results in the following differences. First, their normalized volume curve over time resembles a purely dissolving drop in two steps, a first, faster diffusion for the ethanol followed by a slower dissolution of water. This is different to what we observe, where we can distinguish between an initial, swelling behaviour for the drop up to a maximum volume, after which the drop starts to dissolve in a more or less uniform fashion. Timescales also differ between our experiments. Whereas their first step, transfer of alcohol from the drop to the bath, occurs in about 50 minutes (which is in agreement with our experiments), their second step, which consists in the dissolution of the water drop, may take up to 30 hours to complete. In all our experiments we attained complete dissolution in a few (2 or 3) hours. Again, we believe the difference in the amount of alcohol in the oil is responsible for these quantitative differences, and we believe that taking into account the differences in the initial compositions, our experiments are in agreement and experience the same underlying phenomenon than the mentioned literature.

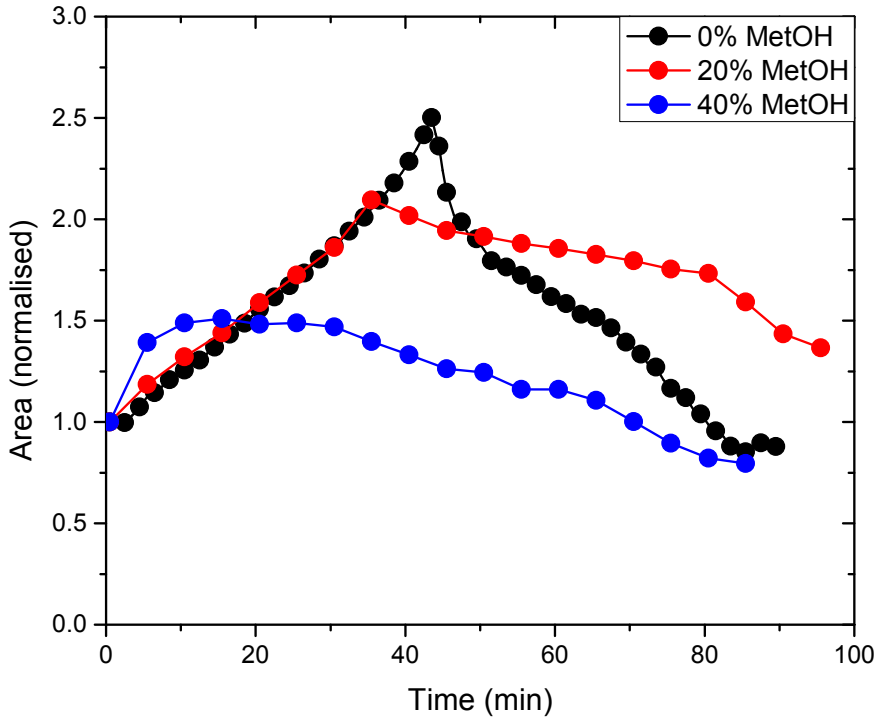

Figure 4.5 *Area (normalized by its initial value) evolution for three different drops with varying methanol concentration. They correspond to the experiments shown in Figure 4.3, under the assumption that the drops have cylindrical symmetry. From this representation, the offset time, initial and maximum volume are easily obtainable. A decreasing trend for the offset time and the maximum volume with an increasing amount of alcohol is obtained. These trends are qualitatively reproduced in other experiments.*

The values obtained for the relative growth, calculated as the difference between the maximum and initial volume divided by the initial volume, as well as the offset and spontaneously formed clouds' times have been plotted in Figure 4.6. The error bars represent the standard deviation obtained from the several experiments analyzed. Within these substantial error bars, the trends for the relative growth and offset time are similar and reasonably linear. The clouds' dissolution time follows an increasing trend however, which we have explained below.

With the presented information, our tentative hypothesis about the role of the alcohol inside the initially pure water drop is that it aids the dissolution of the drop in the bath, leading to a one-phase system. This would explain the increase in volume due to the influx of methanol from the bath, resulting in bigger

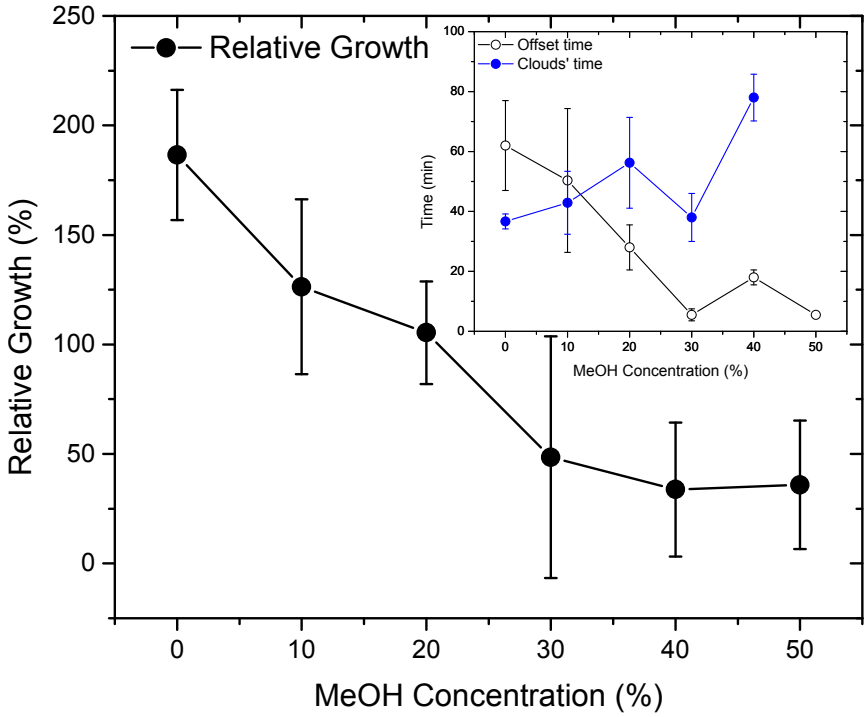

Figure 4.6 *Relative growth, offset and spontaneously formed clouds' time versus the methanol concentration in the single drop injected. We can observe a clear decrease in the relative growth and the offset time as the amount of alcohol increments, with an opposite trend for the clouds' dissolution time. The error bars were obtained as the standard deviation between several experiments analyzed.*

drop volumes when the initial methanol concentrations are low. The offset time, which is the elapsed time until the volume starts to decrease, is also explained by the same reason - if the amount of methanol inside the drop is low, more time will be required to achieve the concentration needed to start redissolving. The "clouds" spontaneously formed around the injected drop, which are created almost immediately after injection for all alcohol compositions, can be seen in the first frames of the drop evolution shown in Figure 4.3. For drops with lower alcohol compositions, these clouds redissolve faster (e.g, in the case of the pure water drop, after 15 minutes the clouds are almost redissolved, whereas in the case of the 60/40% water-methanol drop the clouds are clearly seen after 45 minutes). This means that the higher the alcohol content in the drop, the longer it takes for this huge amount of tiny droplets to redissolve. This is the opposite of what happens to the injected drop, where a higher alcohol content leads to a lower offset time, indicating when the drop starts to redissolve. Our explanation

is as follows: the less the initial amount of alcohol in the drop, the larger the amount of methanol flowing in from the bath, leading to longer redissolving drop times. At early times, the drop is far away from the composition needed to start to redissolve, but the continuous flux of alcohol into the drop helps the spontaneously formed droplets to dissolve, as they are much smaller and therefore only need a tiny amount of methanol to redissolve, which is supplied by the continuous renewal of methanol around the drop. For high-alcohol content drops, they reach their offset time much earlier than the spontaneously formed clouds dissolution time. Therefore, there will be an increased water content around the drops, and the alcohol flow in the area around the drop will be reduced. This would be the reason for the longer droplet dissolution time.

Now, we will relate the observed behaviour with the ternary phase diagram of our system. We have written a Python script (see Appendix A.2) which is able to do two different tasks. The first objective is to be able to generate a number of tie-lines, connecting the conjugate phases in which a composition located inside the binodal will divide into. Given a set of tie-lines (obtained from the literature [136]), the code performs a transformation of the given compositions as concentrations into concentrations in a Hand coordinate system. [137–139] A linear fit of these Hand concentrations when plotted as the ratio of the miscible solute (methanol) to the other solutes, i.e $log\frac{[MeOH]}{[H_2O]}$ versus $log\frac{[MeOH]}{[Oil]}$, give us the Hand constants A and B, which allows us to find the parameter E and F. With these variables we are now able to obtain more tie-line compositions.

The next objective is to use the generated tie-lines to calculate the diffusion paths when contacting an unknown binary mixture (for example, alcohol-water) with a fixed, known, binary mixture (such as alcohol-oil). With the analysis described in [140], we can find a function with only one variable (α) that we can solve for our known compositions (the tie-line compositions generated in the previous step) to obtain the values for α. With those values we are able to determine the composition of the unknown binary mixture.

We have used this approach to recreate the diffusion paths our aqueous solution goes through when injected into the bath solution. Therefore, the fixed binary mixture corresponds to the bath, and we will obtain several solutions for varying ratios of alcohol-water solutions. We have plotted some of these solutions in Fig. 4.7. The blue circles indicate the initial compositions (bath on the left axis, and drop on the right axis) for the contacted solutions. There are blue lines that connect these initial compositions with the tie-line compositions generated by our

code, which appear as red circles. The tie-lines itself have been represented as red dashed lines.

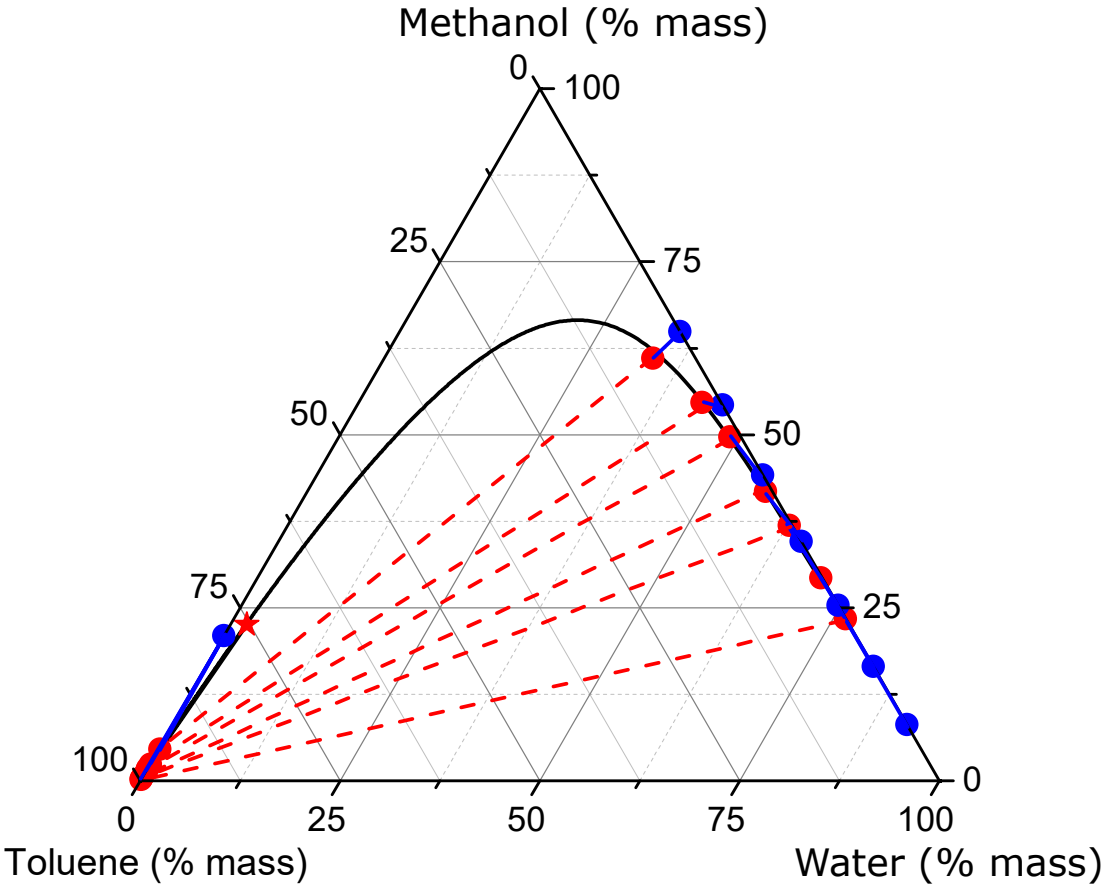

Figure 4.7 *Ternary phase diagram for the methanol-toluene-water system. Plait point (red star), initial (blue circles) and tie-line compositions (red circles joined by dashed lines), which were determined using the code described in Appendix A.2, are included.*

The slope of the tie-lines indicate the preference of the miscible solute (methanol) for the aqueous phase, having a positive slope towards the alcohol-water axis. Then, as expected, the diffusion pathways generated by our code connects a very alcohol-rich water phase with an almost pure toluene (oil) phase. An initially lower alcohol content in the water phase resuts in shallower tie-lines, which become steeper the higher the amount of alcohol in the drop. This relates with our experimental observations of faster, more dynamic mass transfer observed in systems with a higher alcohol content in the injected drop (see Figure 4.3 for the experimental images).

The slope of the obtained tie-lines has been plotted in Fig. 4.8, where we can observe an steady increase of the slope when increasing the methanol concentration inside the injected drop. A higher slope is usually identified with

faster dynamics in the system, which will lead to shorter diffusion times. This is indeed what we observe in the size-evolution curves for injected drops shown in Fig. 4.5. These curves reach their maximum value (previously defined as the offset time) at shorter times for higher alcohol concentrations, which means higher tie-line's slopes. After this value, curves are smoother due to the slower diffusion of water.

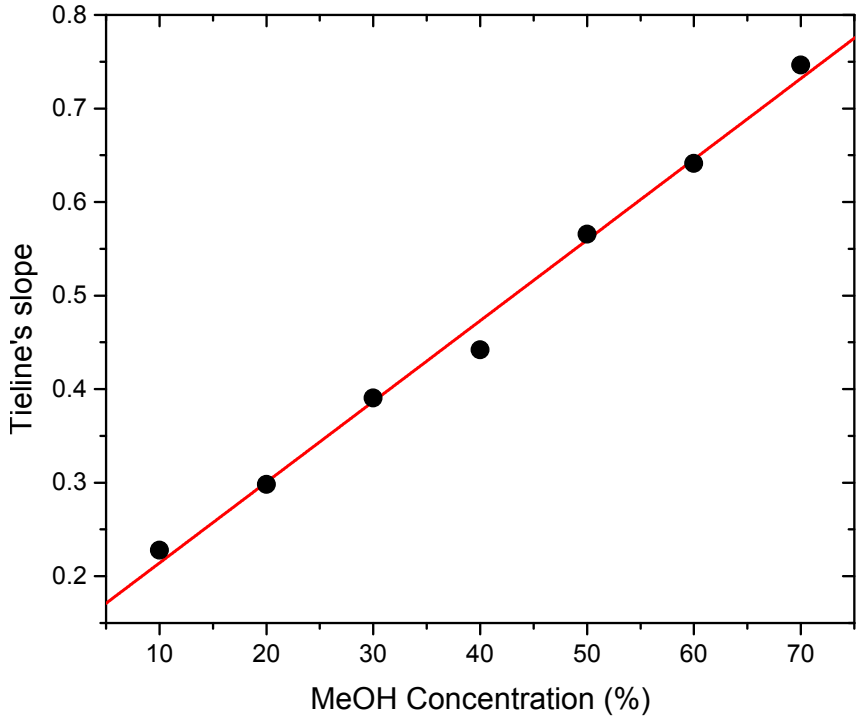

Figure 4.8 *Slope of the determined tie-lines versus the amount of methanol in the alcohol-water mixtures contacted with the bath solution. The red line represents a lineal fit with slope* $m = (8.6 \pm 0.3)10^{-4}$.

We have determined the amount of methanol with respect to water in the drop when it starts to shrink (the maximum volume for each composition at Figure 4.5) from geometrical considerations, i.e assuming the drop's growth is due only to the influx of methanol. This has been represented in Figure 4.9 for various initial methanol concentrations. The ratio was obtained by determining the amount of alcohol that entered the drop from the measured area (assuming the drops were spherical), which allowed us to obtain a radius from which we could determine the volume. The difference between this volume and the initial one, plus the initial methanol if there was any, divided by the initial amount of water was plotted on the ordinate axis. For all but the pure water drop case, we observe

that the obtained value is around ≈ 2.2, which would yield a drop composition of $[H_2O]/[MeOH]$ 31.25/68.75 % in volume, or 36.45/63.55 % in weight. This constant value would indicate that the drops start to redissolve only when these ratios of alcohol/water are achieved inside the drop, and not before. We have also included in Fig. 4.9 shaded areas that represent the confidence interval for different ratios. Using Raman spectroscopy in the 2D experimental setup we have obtained a range of values represented as an orange shade. For the pure water drop using the volumetric considerations described above, the red shade includes the error zone. For the other experiments using different methanol concentration inside the injected drop, error propagation from the standard deviation of each value determined the interval represented in a green shade.

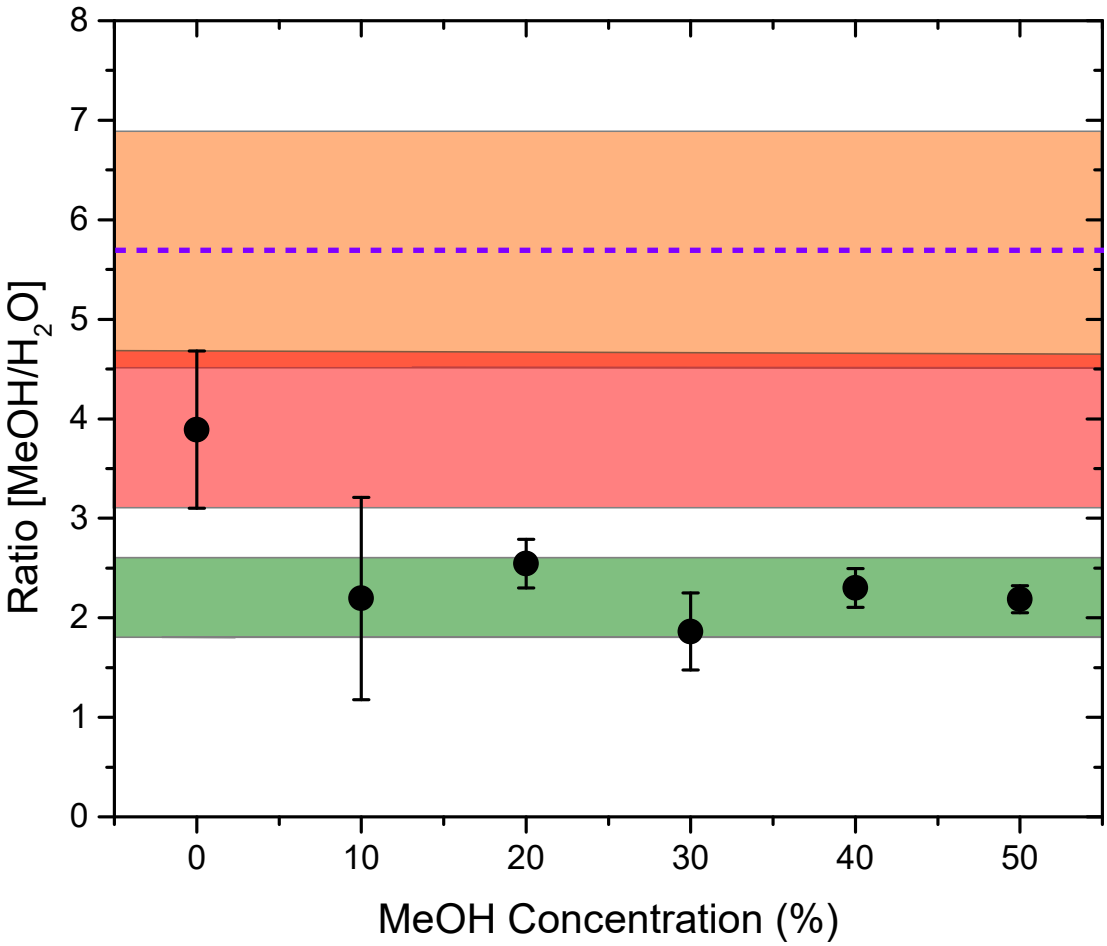

Figure 4.9 *Ratio of the amount of methanol with respect to water obtained from 3D experiments from volumetric considerations. Shaded zones indicate the confidence interval for the value obtained in Raman in 2D experiments (orange), volumetric ratio for pure water drop (red) and for mixed drops (green). Purple dashed line indicates the ratio necessary to stop spontaneous emulsification, obtained through the argument depicted in Fig. 4.11.*

We have also employed this system's ternary phase diagram to help us explain our experimental observations regarding spontaneous emulsification outside the drop. In the following text, the references to certain points present in the next discussion refer to the points marked in Figure 4.10.

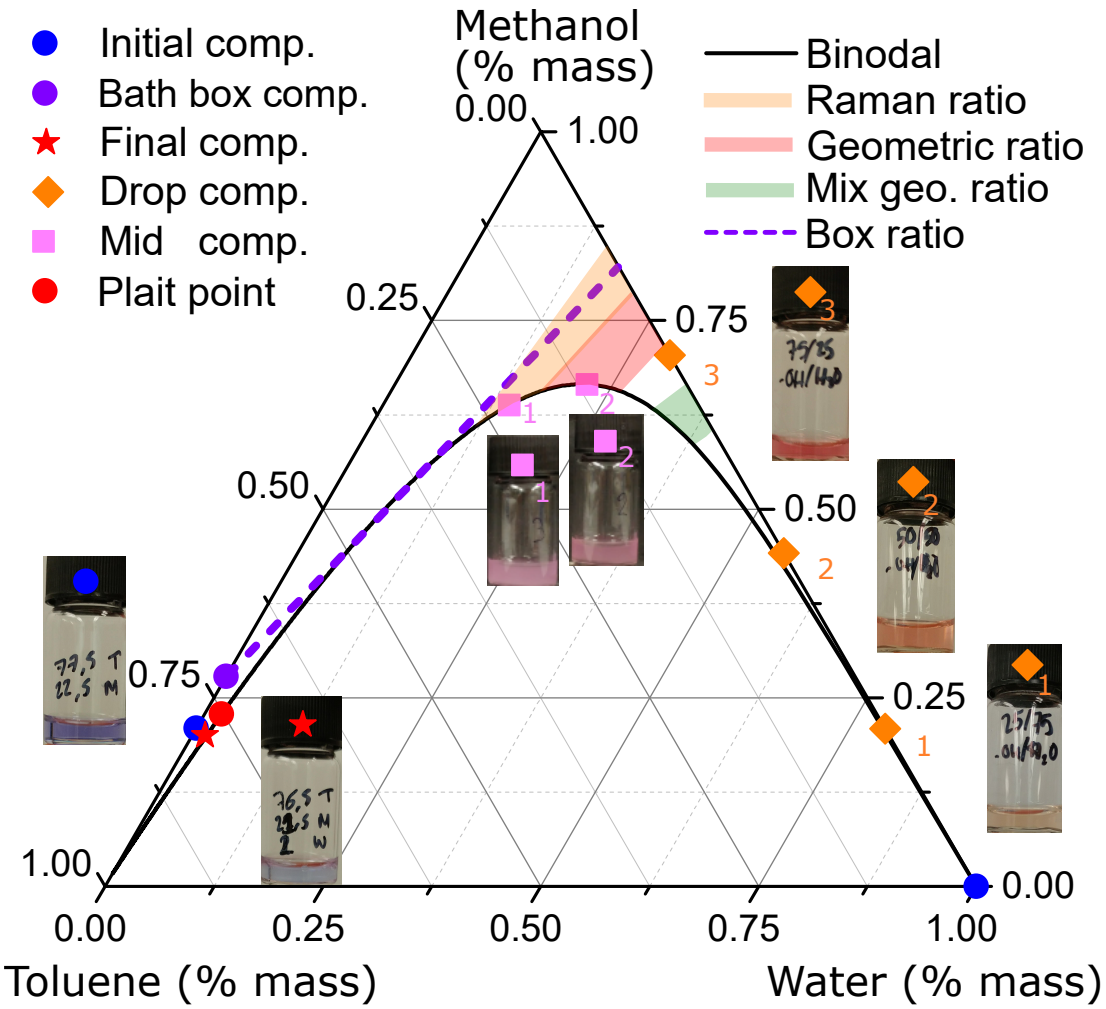

Figure 4.10 *Ternary phase diagram for the methanol-toluene-water system. Plait point (red circle), initial (blue circles), final (red star) and drop equilibrium compositions (in different shades, see legend), as well as other compositions related with the evolution of the drop next to their picture when dyed with Reichardt's dye (pink and orange diamonds).*

First, we need to clearly differentiate between the final system composition (red star), which due to the difference in volumes involved (10:1 relative to the bath:drop) is very close to the initial bath composition (blue circle on the left axis), and the equilibrium drop composition on the alcohol-water axis, which we define as the composition found when the drop achieves its maximum volume before shrinking. Depending on which of our experimental setup we use, we have

obtained different values for equilibrium drop composition:

- If we use the measured compositions using Raman spectroscopy in a 2D experimental setup (which will be explained in more detailed later on), this composition will lie somewhere in the orange-shaded area ("Raman ratio" in the figure). The compositions in this area, which is the same than the orange zone in Fig. 4.9 have the same ratio of alcohol/water.

- Instead, if we use the volumetric argument described before (see also Figure 4.9) and assume all the volume increase is due to the influx of alcohol inside the drop, we obtain the red-shaded area, shown in the legend as "Geometric ratio".

- For the rest of experiments using mixed water/alcohol drops its equilibrium composition would be the green-shaded zone, labeled as "Mix geo. ratio".

- Finally, we have also included as a purple dash line one of the diffusion paths for which no spontaneous emulsification would be observed. To obtain the composition for the purple point situated in the Toluene-Methanol edge (left axis), we need to explain the simplification we used.

We have represented in Figure 4.11 a diagram to help visualizing the approximation we did to obtain the composition for the bath near the drop at an intermediate time (bath box composition). The situation we are representing is as follows: after the drop has achieved its maximum volume by means of incorporating alcohol from the medium, said drop starts to slowly redissolve into the bath. Because the alcohol has a higher diffusion coefficient than water, alcohol will diffuse faster than water into the bath. This creates an area around the drop in which the bath solution is highly enriched in alcohol. This zone has been enclosed in Fig. 4.11 by a red dashed cube, and its composition is indicated in Figure 4.10 as the purple dot. Again, this equilibrium drop composition will evolve as the drop starts to redissolve into the bath, with the system's composition changing towards the final system composition (indicated by a red star), a single homogeneous phase.

In our experiments, when we inject the drop it starts to incorporates alcohol, its composition rising from the water vertex (blue circle on the bottom-right vertex) along the water-methanol axis (situated on the right hand side of the diagram) until it reaches the drop's equilibrium composition (indicated by different

dash areas). According to Ruschak and Miller's criterion [55], spontaneous emulsification occurs whenever the diffusion path joining the bath and drop compositions crosses the binodal. This happens for all the different compositions the drop goes through until it reaches the equilibrium drop composition. However, once the drop has the equilibrium composition if we join it with the bath box composition (the composition inside the enclosed red dashed cube in Fig. 4.11) the obtained diffusion path crosses the binodal ever so slightly. Using the equilibrium drop composition obtained through Raman spectroscopy we obtain an area compatible with the purple dashed line, which would stop the emulsification. For the other equilibrium drop composition ratios, such as the geometric ratio and the mixed geometric ratio, their diffusion paths would still cross the binodal. Because the calculation of diffusion paths and the "crossing binodal" criterion for spontaneous emulsification only applies under a series of "model" assumptions, it is possible that the real diffusion path does not cross the binodal at late stages for our system. This would halt the the spontaneous emulsification. This would agree with our experimental observations, where after some time the spontaneously formed clouds of water-rich droplets stop growing and start to gradually dissolve into the bath.

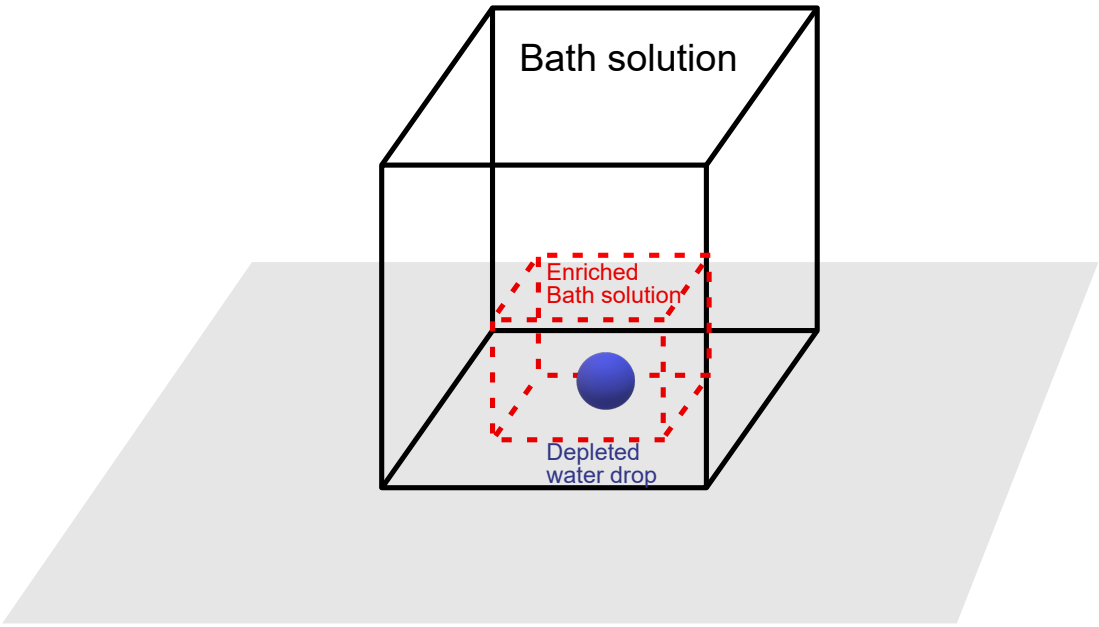

Figure 4.11 *A cartoon showing the situation after the methanol from the swollen drop has diffused out to the bath. Standard bath solution is enclosed in the cuvette (delimited by the black cube), with an enriched bath solution (enclosed by a red dashed cube) and a depleted water drop in the center (blue sphere). The substrate is shown as a grey rectangle. Cartoon is scaled, with a 2 cm. side cuvette.*

In our explanation, the offset time parameter, which corresponds to the time at which the equilibrium drop composition is achieved, indicates the time at which the drop starts to redissolve, observable as a decrease in its volume. Using the simplest diffusion equation, $t = x^2/D$ with x=1.5 mm as the radius of the injected drop and D=1.0×10^{-5} cm^2/s as the diffusion coefficient for these kind of systems (similar to the values we got in Chapter 3), we get a diffusion time of 37.5 minutes, which is similar to the values we have obtained experimentally for the offset times. At roughly the same time, the "clouds" made of spontaneously formed droplets that hover around the drop start to slowly redissolve. As explained in the previous paragraph, this is because no more spontaneous emulsification is occurring for these compositions and the previously formed droplets are redissolving into the bath.

We have been able to follow the diffusion of methanol visually through solvatochromic dyes, specifically Reichardt's dye and Nile Red. According to the polarity of the solvent around the dye molecules, the wavelength of the light they scatter changes, therefore changing its colour locally. The use of particles in our bath seemed to inhibit the dye movement, so the experiments were performed in a bath without particles, thus not strictly adhering to our "standard" compositions, but using a very similar experiment in which the diffusion movements observed can be directly extrapolated to our "standard" experiments.

It is possible to find cases in the literature where the presence of nanoparticles certainly interfere with the emission of dyes [115, 116], which was our case. It is also well known in the literature that several dyes are surface-active, acting as surfactants and modifying the surface tension of the system. [141] Depending on the nature of the dye, they affect the interfacial tension in a different way, which broadens their possibilities to even be used in medical applications. [142] However, at the concentrations we have employed them, the dyes does not seem to modify the interfacial tension in our experiments, as readily seen by the lack of change in the contact angle of the injected drops when comparing Figures 4.3, 4.13 and 4.16. We have displayed an example experiment for each of the dyes used and we can observe how various coloured zones, which indicates the presence of different chemical environments for the dye molecules, are present.

We have compared the compositions and colours in different solutions displayed in Figure 4.10 with our experiments. Doing so, we have been able to identify the different zones indicated in the Figure 4.12, such as the initial bath solution, and a water-rich bath solution. Reichardt's dye proved to provide more obvious and

distinguishable colour changes, especially inside the drop, where the use of Nile Red did not yield any observable change. Using these dyes we were able to easily follow the evolution of the bath, from an initial dark blue/purple characteristic of no water presence, towards a more water-rich bath composition shown as a lighter blue colour. We could also track changes in the drop itself, which evolves towards more red tones as it becomes enriched with methanol. Unfortunately, the images showing this are not able to capture this change as clear as it is in reality. Alas, this method proved limited when being employed to discern the diffusion paths our system may follow. This is because we couldn't relate some of the compositions shown in the ternary diagram with colours observed experimentally (mid compositions indicated by the magenta squares in Fig. 4.10 were not observed). However, it certainly proved useful to reveal very visually which components diffuse towards which phase.

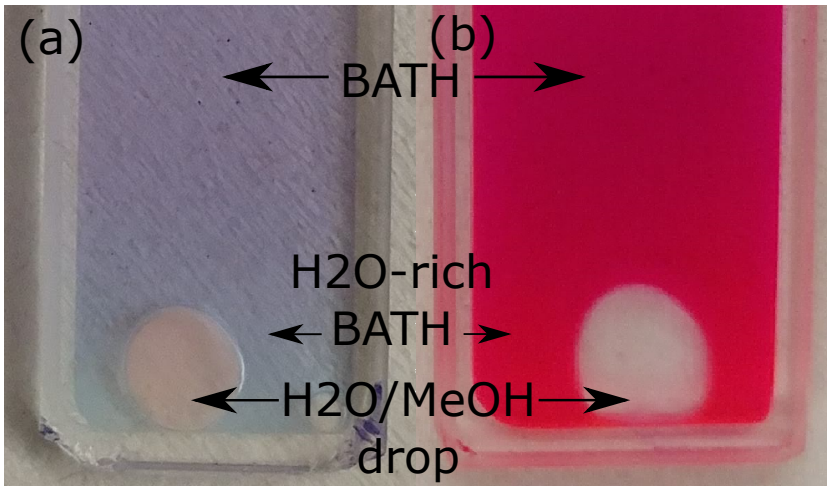

Figure 4.12 *Dye experiments with no particles in the bath, using either Reichardt's dye (a) or Nile Red (b). Different regions and their colours are indicated. Although it is not very clear from the picture, the drop in (a) becomes slightly red. Experiments were performed in the quasi 2D experimental setup. Cuvette width is 5 mm.*

A series of frames of a typical experiment with Reichardt's dye using a 3D cuvette recorded with a colour camera are shown in Figure 4.13. This allowed us to visually identify the interactions between different components at different places thanks to the dramatic colour changes it induces. Very shortly after injection (less than 10 seconds) the bath around the drop changes its colour towards more blue tones, indicating the presence of water in that area. That is also confirmed by the creation of spontaneously formed water droplets, which can be seen as dark grey streams, confined to the water-rich bath region, which is light-blue coloured. These droplets appear initially in the bottom part of the cuvette, where due to

buoyancy effects the water-rich bath solution has settled because of its higher density.

The influx of methanol into the drop is clearly seen as an increase in volume, which supported by our Raman measurements indicates a more methanol-rich drop, which changes its colour gradually towards redder tones. Two color scale bars have been added to Fig. 4.13, the top bar showing change in color when the amount of water in the bath solution changes from 0 to 2 % in weight, whereas the bottom bar represents color change when the amount of methanol inside the drop evolves from 25 to 75 % in weight. As shown in Figure 4.10, increasing amounts of water into dyed methanol modify its colour, reducing its strength towards lighter tones. That is why we are confident to assume that methanol is indeed flowing in.

Lastly, it is worth noticing the strange structure formed at the apex of the drop, which is transitory, as it appears intermittently as the system evolves. Because of how close our bath composition is to the plait composition (where the tie-line's length is zero and the miscibility gap disappears) in our system, as can be seen in Fig. 4.10, it may very well be the case that a phase separation phenomenon occurs, which is in agreement with what we experimentally observe. This is, a clear interface between the "stock" bath solution shown as purple, a water-rich bath solution coloured as light-blue, and the injected drop is created at the top of said drop. It is also remarkably similar to vortex structures created by the Marangoni effect. In our case, because the methanol inside the drop is not distributed homogeneously due to density effects, we predict it is able to create surface tension gradients along the drop interface. These gradients will create Marangoni flows which are able to form structures as the ones we observed (please compare with the figures included in [143] and Figure 2 in [144]). Because we do not have particles in these solvatochromic experiments, these effects may be amplified and shown more dramatically due to stronger interfacial flow effects, which might be dampened in our standard experiments including particles.

We have used the experimental images presented in Figure 4.13 to discern whether a quantitative change in "redness" is measurable. To do so we have extracted the red channel from the RGB images and obtained the histogram only inside the drop for the same times as the images in Fig. 4.13. These histograms have been included in Figure 4.14 and they show a decrease in intensity towards darker (lower) intensity values, which indicates that there is less transmitted light due to the presence of spontaneous emulsification inside the drop, visible as a milky or

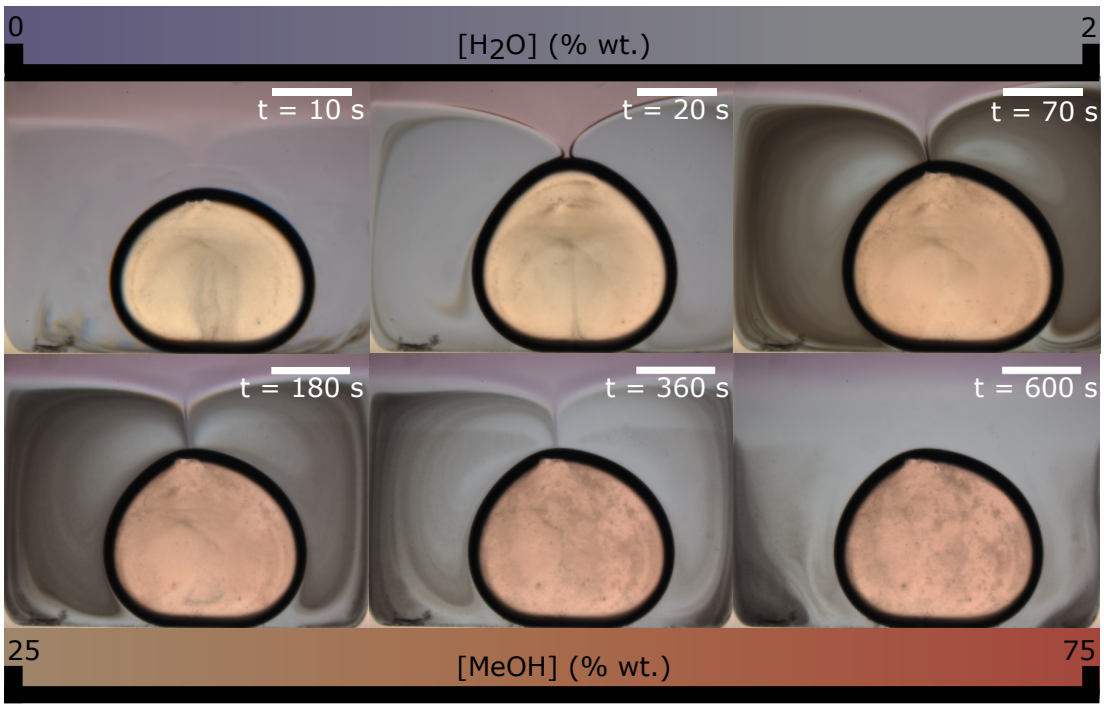

Figure 4.13 *Evolution over time of a water drop in the bath without particles captured with a colour camera. In comparison with the first frame, we can observe how in the following frames the bath around the drop gets bluer, indicative of a water-rich area. The grey areas around the drop are created by spontaneous emulsification of the out-diffusing water, which gradually fades away as equilibrium is reached. A progressive colour change towards redder tones along with a volume increase indicates methanol influx into the drop. The top color bar scale represents the amount of water in the bath solution whereas the bottom bar represents the amount of methanol inside the drop. Lastly, it's worth mentioning the vortex-type structure observed on the apex of the drop, characteristic of Marangoni flows, which would happen as the methanol content in the drop is unevenly distributed, creating surface tension gradients. Scale bar is 2 mm.*

cloudy-looking aspect. The presence of emulsification obscures the color changes due to their higher influence on the intensity.

We have included a cartoon in Fig. 4.15 to explain why the convection rolls observed are formed and their direction. First, we need to identify the three different phases in play as the drop, the bath, and a water-rich bath solution. It is in this last location where an Ouzo effect takes place, producing spontaneously formed water droplets. As we've said before, a methanol gradient inside the drop and the possibility that the critical point in our ternary system is close to our compositions create differences in the interfacial tension values along the

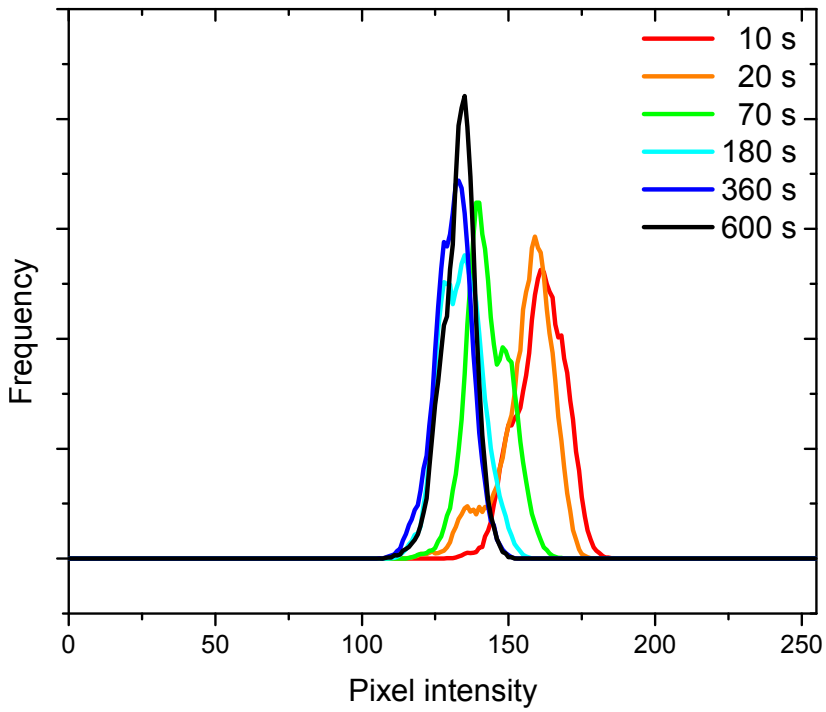

Figure 4.14 *Histograms of the drop shown in Figure 4.13 of the red channel at different times. A decrease in intensity over time due to spontaneous emulsification masks any change towards redder tones.*

drop's interface. Lower values will be situated at the top (where the methanol concentration is higher) whereas higher values of the interfacial tension will be located at the bottom, where we have a water-rich composition. These differences are able to create a Marangoni instability along the interface that will create a flow going from the top to the bottom. To achieve continuity in the water-rich bath portion of our system, another flow to bring fresh material will occur from the bottom to the top far away from the drop.

A similar montage for the time evolution of a water drop injected in a bath with no particles, but using Nile Red instead of Reichardt's dye, is included in Figure 4.16. Although it is not as dramatic and striking as the colour changes that happen when using Reichardt's dye, it is possible to observe a bath colour change towards more orange tones in the vicinity of the drop. The creation of spontaneously formed clouds and its evolution over time, which is slightly slower than with Reichardt's dye, seem more dramatic, with darker (more populated) regions.

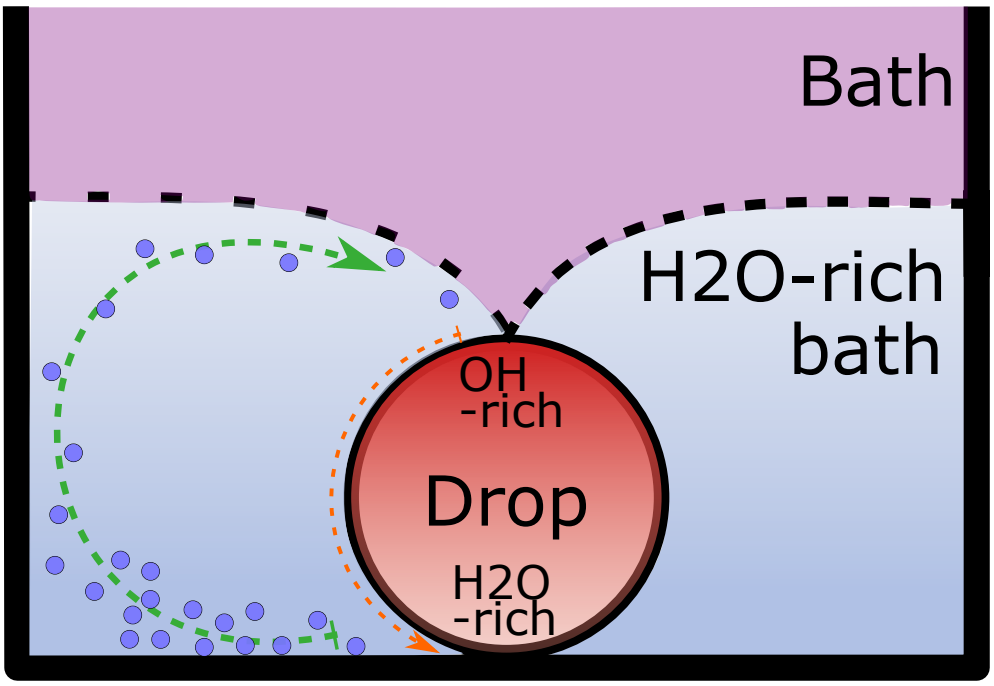

Figure 4.15 *Sketch with our three-phased system composed by the bath (top), a water-rich bath solution (bottom) and our injected drop (bottom circle). Solvatochromic dyes helped us to identify these different compositions by colour changes. A methanol gradient inside the drop is indicated by a red colour-gradient. This gradient induces a Marangoni flow (orange dashed line) along the drop interface because the interfacial tension also changes with the methanol gradient. To maintain continuity, there must be another flow from the bottom to the top far away from the drop (green dashed line) Density effects will also produce a water-gradient in the water-rich bath solution, promoting spontaneous formation of water droplets (dark blue circles) in the bottom part of the cuvette.*

To obtain quantitative results about the methanol concentrations inside the injected drop we have used Raman spectroscopy with our system, as we did for the ethanol system in Chapter 3, except here we only injected one drop. With our "reduced" experimental setup (1 mm width cuvette), we quickly realized that the faster and more aggressive movement of the methanol, when compared to ethanol, leads to a dramatic volume expansion and a great amount of emulsification. This renders our studies with two drops useless, as drops are now able to extend through a great portion of the cuvette and the emulsification hinders the possibility to know where is the Raman laser pointing, and thus, measuring. These were the reasons that motivated our decision to limit our studies to one-drop systems, which is how almost all of the experiments in this chapter have been performed.

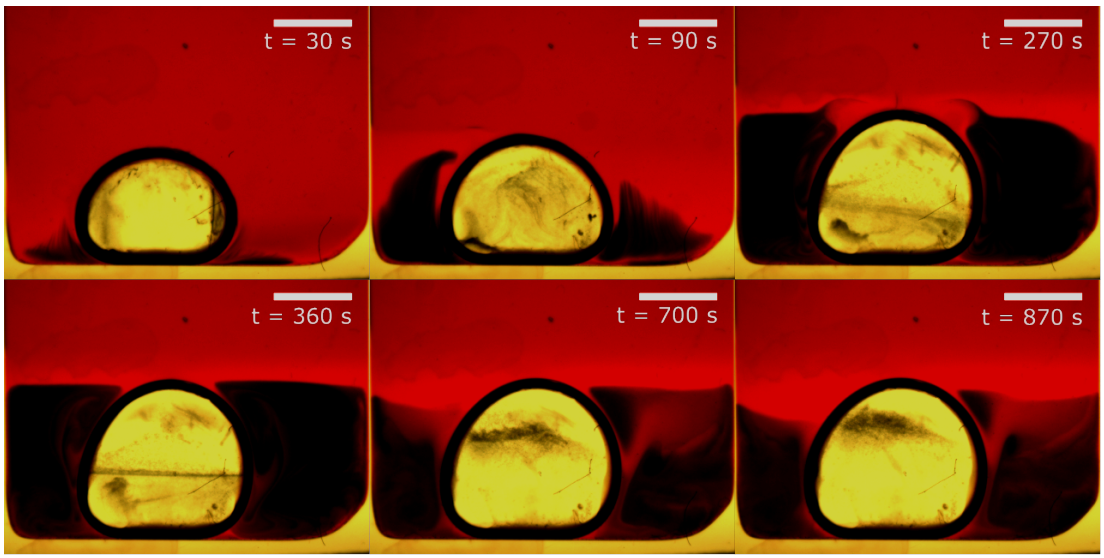

Figure 4.16 *Evolution over time of a water drop in the bath without particles using Nile Red, captured with a colour camera. Although the drop inside does not change colour, in its proximity the bath changes towards more bright/orange-like colours, indicating the presence of water. Black shapes around the drop are spontaneous formed water droplets, emulsified due to the out-diffusing water from the drop. They gradually redissolve as time progresses. Scale bar is 2 mm.*

For our Raman experiments we have varied the amount of silica in the bath and observed its influence on the behaviour of the injected drop. The mean drop composition and its standard deviation, shown as the error bars, for each silica composition has been plotted in Figure 4.17. These compositions were obtained from the ratio of methanol to water integrated areas. Because toluene peaks are in the same place than the methanol's, no measurement of the toluene in the drops, or the bath itself were possible to obtain. There is a one minute delay between the injection of the drop and the measurement of the first point, caused by experimental constraints such as the laser repositioning, its refocusing and the time acquisition needed to obtain a good signal-to-noise ratio. When no particles are present in the bath, which according to our ethanol studies in the previous Chapter creates the most mobile system, the initial water concentration obtained is *circa* 30%. Equilibrium, defined as the point where the concentration remains stable over time, is reached very fast, in about 10 minutes. These values are considerably lower than those obtained for our standard experiments with 0.2 % silica content, where the first measured water concentration is *circa* 70% and the equilibrium time is about 30 minutes. However, the experiment with 0.4 % silica presents results that are similar to those for the 0.2 % content, although the rate of diffusion seems to be slower, with a trend switch from exponential to linear.

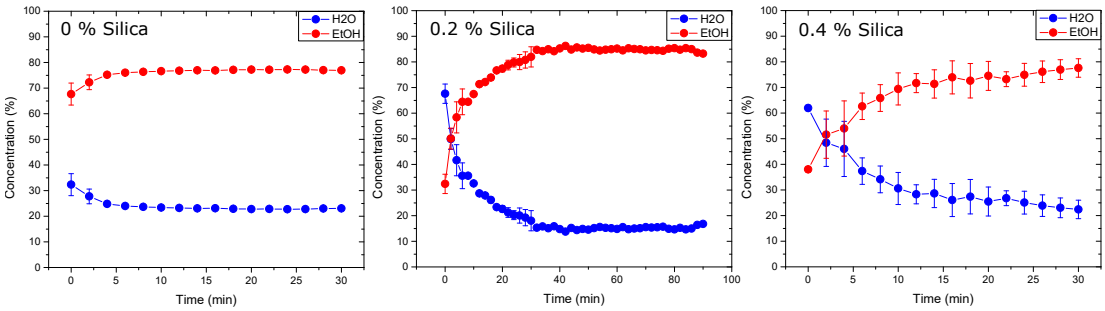

Figure 4.17 *Drop composition determined by Raman spectroscopy over time for different silica concentrations in the bath. If no particles are present, the initial water concentration is low, indicating that the diffusion in this case happens very fast. The second and third experiments, with 0.2 and 0.4 % silica, respectively, are similar, although with lower silica content the change in composition seems to occur faster. Errors are the standard deviation obtained for several experiments.*

4.4 Conclusions and future work

By varying the alcohol concentration in alcohol-water drops injected in an oil bath solution we have obtained several quantitative parameters. After injection, the drop swells up to a certain maximum volume, which is inversely proportional to the initial amount of alcohol in the water, due to the influx of alcohol from the bath. This is due to the preferential partitioning of alcohol into water rather than the oil. This maximum volume is achieved after a certain time that we have termed "offset time", which has the same trend as the volume. After it, the drop starts to shrink as it redissolves into the bath to finally form a homogeneous phase.

Using a homemade-script to calculate diffusion pathways we have been able to relate these paths with the diffusion dynamics observed experimentally. The slope of the tie-lines calculated for increasing amounts of alcohol into the injected drop becomes increasingly steeper, resulting in faster diffusion times. Spontaneous emulsification is also present in this system, resulting visible as clouds of tiny droplets formed around the injected drop. Determining the highest alcohol-water ratios achieved by the drop before it starts to redissolve helped us to explain the disappearance of these spontaneously formed droplets through the "diffusion and stranding" mechanism in the ternary diagram.

We have also employed solvatochromic dyes to follow the direction in which our components diffuse. Reichardt's dye allowed us to confirm the increasing amount

of methanol inside the drop and the presence of water in the bath thanks to its incredible colour variations corresponding to changes in the solvent's polarity. Dyes were used in particle-less systems because the particles interfered with the dyes' movement. This produced more dynamic experiments in which a new phase formation at the apex of the drop was observed. This new phase results from the bath solution being very close to the critical point, forming a water rich bath phase in contact with the "standard" bath solution and the water drop. The absence of particles also allowed us to observe the movement of spontaneously formed droplets following a strong Marangoni effect at the interface of the drop. As seen in the previous chapter, particles in the bath increase its viscosity and make it gel, effectively "trapping" the droplets which are not able to move freely.

Raman experiments were also performed for varying amounts of silica concentration in the bath for diffusing single-drop experiments. A relationship between the equilibrium time and silica concentration was observed qualitatively, resulting in faster diffusion for lower concentrations, as expected.

The use of different alcohols in diffusion experiments as the ones performed here would help to extend the knowledge of the presented relationship between tie-lines and diffusion times. Using inverse systems with oil drops in water bath solutions for alcohols that partition preferentially into the oil phase will also broaden the amount of eligible alcohols.

Using the model (which is divided in two parts, one to model the mass transport between two contacted multicomponent fluids (Stefan problem with a moving interface [145]) and another to determine the equilibrium composition at the interface (equal chemical potentials and the UNIFAC model)) proposed by H. Tan in the Chapter 4 of his thesis [103] may prove useful both to confirm its applicability in a similar system such as ours, and to produce quantitative results to be compared with our extracted quantitative diffusion parameters.

Although we presented our results using Nile Red as another solvatochromic dye, due to its huge hydrophobicity no changes in the drop composition could be followed. Finding a different solvatochromic dye may highlight some concealed features we were not able to discover.

Chapter 5

Spawning droplets and fractal dewetting with Pickering drops

5.1 Introduction

In this chapter we will explore a system that, although made of completely different components than in our previous chapters presents a very similar phase diagram. Here, we have replaced the toluene with an alkane, 2,3-dimethylpentane. Instead of the short chained alcohols previously used (methanol / ethanol) we will use 1-propanol and the hydrophobic silica particles have been substituted by Poly(methyl methacrylate) (PMMA) particles, also hydrophobic.

Even though the new system's phase diagram resembles the toluene/alcohol/water diagrams, we have encountered a set of very different phenomena than in our previous chapters. This highlights the importance of not underestimating the chemistry in our models. This chapter will focus on presenting a series of curious phenomena that were observed when injecting a water drop into a certain bath composition. Most of the discussion will revolve around the formation and evolution of new droplets at the interface of a Pickering emulsion and the fractal dewetting patterns that develop when no alcohol is present in the system.

Stability in Pickering emulsions and, more recently, the ability to tune the particle-coverage of the emulsion droplets to allow or inhibit coalescence have been previously researched. Pawar et al [146] were able to produce three different states of coalescence (total, partial and arrested) in the same system by using a

very simple yet elegant approach. By squeezing the emulsion drop into the pipette tip used to inject it, they obtained a range of interfaces with different particle-covered areas. They were able to obtain clear boundaries for the different states by contacting two of these drops, mapping the different configurations. Schröder et al [147] more recently achieved similar results with a different approach. They tuned the particle-coverage of the emulsion droplets' by varying the flow rate of the continuous phase, which modified the kinetic energy of the particles, thus changing the amount of particles able to attach themselves to the interface. At low surface coverage, they explained the coalescence observed due to particle-bridging, whereas a high surface coverage yielded emulsion stability. This was also observed indirectly when presenting a new approach to measure the microfluidic angle of repose in Pickering emulsions [148], where droplet stability was also affected by the particle-coverage of the interface.

Recently, the creation of protocells by self-assembly has been exploited to understand the emergence of life from non-living components. These protocells are compartimentalized autonomous modules, some of which could be able to self-organise into a viable cell. [149, 150] There are two different approaches to study the evolution of protolife systems: a bottom-up approach that requires the spontaneous self-formation of compartmentalization modules able to replicate and/or metabolize, and a top-down approach where present-day cells are being simplified by removing unnecessary genes for cellular life. [151] A Pickering emulsion stabilized with silica nanoparticles formed spontaneously is a new type of protocell. [152] The addition of tetramethoxysilane (TMOS) to the system induced two mechanisms: the production of methanol by hydrolysis (and subsequent diffusion into the aqueous domains) and the condensation of silica oligomers at the interface. If the rates of droplet expansion by diffusion overcomes the TMOS condensation rate, the membrane is not sufficiently elastic to accomodate the new volume and it becomes punctured. This creates a new protocell bud that grows overtime. Additional silica particles in the oil solution stabilize this new bud, which will separate from the original cell and self-heal the exposed part after some time. Multiple budding was also observed with increased TMOS concentration, and these structures (see Fig. 5.1 (a)) are very similar to some of the results later presented in this Chapter, albeit we obtained them purely through physical effects.

Another mechanism to produce budding structures include the use of artificially created networks of protein nanofibrils, which depending on its concentration

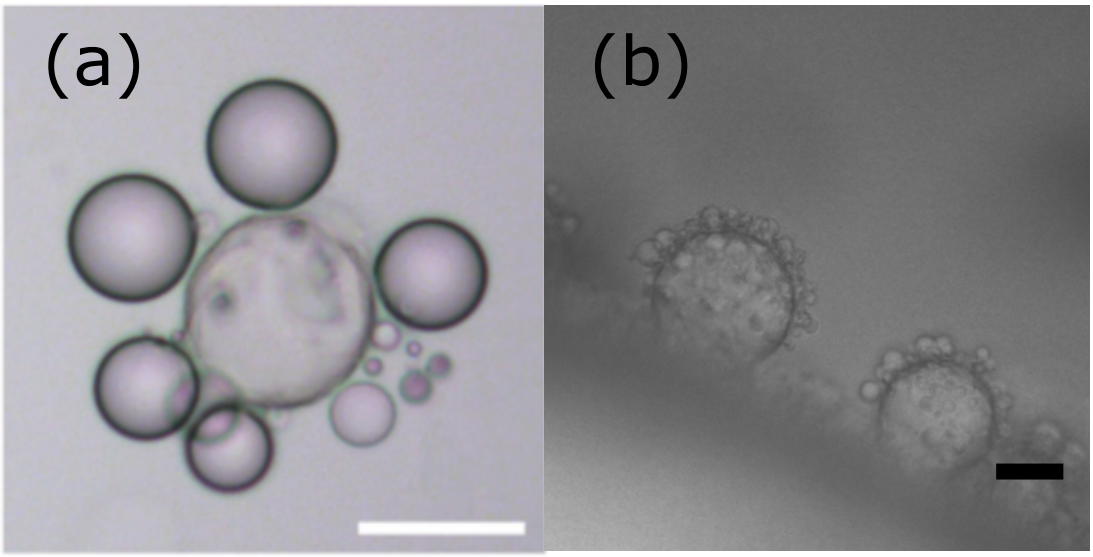

Figure 5.1 *(a) Budding structures observed in [152] and (b) my experimentally observed structures, explained in detail in the Results section.*

can initiate different behaviour regimes. The droplets containing the nanofibrils experience dehydration due to the higher osmolality of the continuous phase. This increases the fibril concentration, producing a phase separation between the fibril network and the droplet aqueous phase. To reduce the interfacial area, the network contracts, buckling the interface and producing liquid protrusions. These protrusions coalesce until enough fibril adsorption at the interface occurs, stabilizing the buds. [153]

Dewetting is the phenomenon that occurs when one liquid retracts from the substrate it was spread onto due to repulsive interactions. It is called fractal dewetting if it creates "tree-branched" structures, as the ones observed in when injecting air into a fluid or separating an adhesive film between two plates. Although these type of structures are very difficult to replicate and understand analytically, they are very common in nature. We can find these examples of this in the veins of leafs, the cardiovascular or the respiratory system (the network formed by arteries or alveoli in the lungs). There are two main mechanisms that produce these structures: tip-splitting, where the fingers divide themselves at their tips (produced by the Saffman-Taylor instability [154]), or shielding [155], where the neighbouring fingers grow faster than the central finger, thus blocking its growth and producing fractal structures. This is considered a variant of the same Saffman-Taylor instability. [156] A popular way to produce and study this type of structure is using Hele-Shaw cells [157]. These cells are formed by two plates narrowly separated creating a channel where a low viscosity fluid (either in

liquid of gaseous phase) is injected into another fluid. Although there is an infinite number of different experimental setups, two examples of the typical geometries used with Hele-Shaw cells can be found in Figure 5.2.

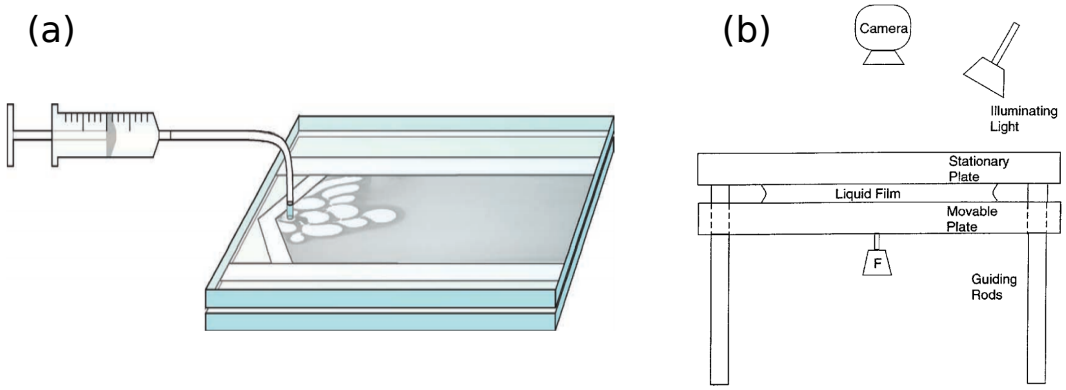

Figure 5.2 *Diagram of two experimental setups using Hele-Shaw cells. (a) A low-viscosity fluid is injected with a syringe into a Hele-Shaw cell, filled with a high-viscosity fluid. Adapted from [155]. (b) Lifting Hell-Shaw Cell setup, where the high-viscosity resting fluid is situated between the stationary and movable plate. The contact surface exposed to the low-viscosity fluid, in this case air, increases when the movable plate is displaced downwards by some adjustable weight. [158]*

The two-dimensional flow occuring in such a device can be used to model the flow of a fluid in a porous medium, such as water displacing oil in a reservoir rock. That is why, historically, there has been a great interest in applications for secondary oil recovery, but more recently, they have become popular as microfluidic mixers [159], heat and mass transporters [160, 161] and vascular systems [162] due to their high surface to volume ratio properties. They have also been used to study the adhesive properties of fluids using "Lifting Hell-Shaw Cells" (LHSC). [155, 156] Using a clever modification of these type of cells - an array of source-holes geometrically arranged - allows the formation of controlled shapes in the resulting structure. [163]

When two superposed viscous fluids are forced through a porous medium, its interface may be stable or unstable. It will be unstable if the less viscous fluid displaces the more viscous one [154], with a number of fingers of the displacing fluid penetrating into the displaced one. Depending on the location of the source (injection) point, we can distinguish two types of fingering. Either linear fingering - if the fluid is injected at one side- with one stable finger forming after some time (see Figure 5.3 (a) for the experimental setup used) or radial fingering [164] if the

injection of the liquid occurs at the centre of the Hele-Shaw cell (see Figure 5.3 (b)). An increment in the injection pressure results in thinner fingers, with an increasing number of side branches with further increments. [165]

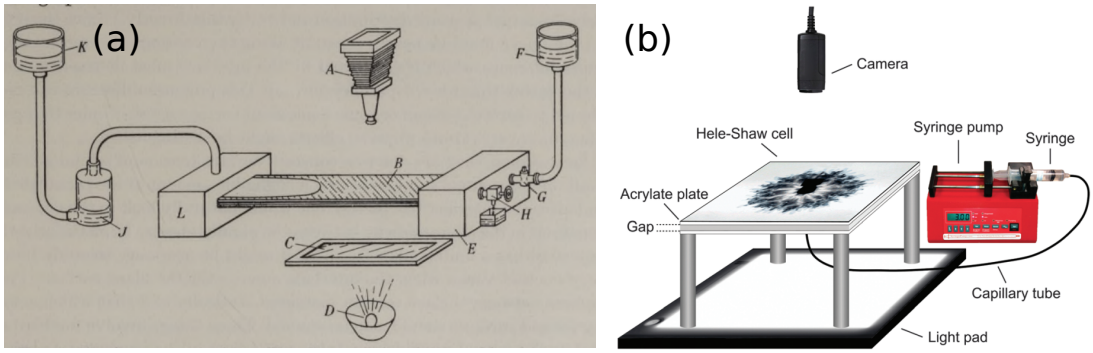

Figure 5.3 *Diagram showing two different experimental setups for Hele-Shaw cells, producing linear (a) and radial (b) fingering. Image (a) has been adapted from [154] and image (b) from [166]*

This chapter presents several striking micrographs of "fractal-like" spawning droplets at different levels (at least three), even when the parent drop's interface is covered by particles. More curious phenomena occuring to these droplets (bridging, sudden dissolution) have also been captured and presented, all this occuring on a chemically "simple" ternary diagram, very similar to the ones employed in the previous chapter, yet yielding very different results. Fractal dewetting patterns changing with the particles' size were also observed and characterized.

5.2 Experimental methods

Typical experiments were performed by filling a cuvette with a standard bath composition (90/10/2 for 2,3-dimethylpentane/1-propanol/PMMA particles) and following the time evolution of an injected aqueous drop in the microscope.

PMMA particles were synthesized by Andrew Schofield using the method described by Antl and others. [167] These type of particles, as well as silica ones, are used extensively in the study of condensed states of matter and concentrated suspensions due to their behaviour as model hard-spheres when sterically stabilized. [168, 169] Our particles were stabilized with grafted poly-12-hydroxystearic acid (PHSA).

The bath was prepared using 2,3-dimethylpentane (Sigma-Aldrich, ≥99 %), 1-propanol (Sigma-Aldricht, ≥99.7 %) and, unless specified otherwise, fluorescent PMMA particles with a radius of 106 nm, as measured by dynamic light scattering (DLS) on an ALV light scattering setup. The particles were dispersed using a "VWR Ultrasonic Cleaner USC 300T" for a total time of 9 minutes and then vortexed for 30 seconds in a "Fisons whirlimixer" shortly before the experiments.

A 5 μL drop was injected into a 1 mm path length optical cuvette from Starna Scientific using a Hamilton Microliter #702 syringe and a 0.72 mm diameter Hamilton steel needle. The time evolution was recorded either in a Nikon Eclipse E800 microscope (bright field) or a Zeiss LSM700 to do confocal scanning laser microscopy (CSLM).

For the analysis of the dewetting patterns found, we have used ImageJ [96] to threshold and binarize the images. A homemade Python script (see Appendix A.3) determined the "Minkowski-Bouligand" fractal dimension by using the Richardson's method (see section 2.6), also known as varying slope or compass dimension. This program quantifies the amount of the fractal structure inside a certain grid. By varying the size of the reticles in the grid, we are able to plot the amount of fractal inside the grid versus the size of the reticle, thus obtaining the fractal dimension as the slope. [74]

5.3 Results

5.3.1 Exploring the phase diagram

A wide range of bath and drop's compositions have been explored to cover an extensive part of the phase diagram (as shown in Figure 5.4), in order to map different behaviours. Contacted compositions have been colour-coded by pairs, being the bath points along the left axis, and the drop compositions along the right axis. Bath compositions will be indicated as 2,3-dimethylpentane/1-propanol in % volume, whereas drops compositions will be indicated as water/1-propanol. Although this phase diagram does not take into account how particles may influence it, the complete phase diagrams ("prismatic phase diagrams") are not common in the literature, and fairly tedious to obtain experimentally. One of the most important particles' parameters which may affect the phase diagram is its wettability, where a different ternary diagram is plotted for each

wettability value along the prism axis, or Z-axis. [170] These changes in wettability mainly affects the morphologies the system will present, which may include Pickering emulsion drops, bijels, or if one phase is in gaseous state foams or liquid marbles. [171]

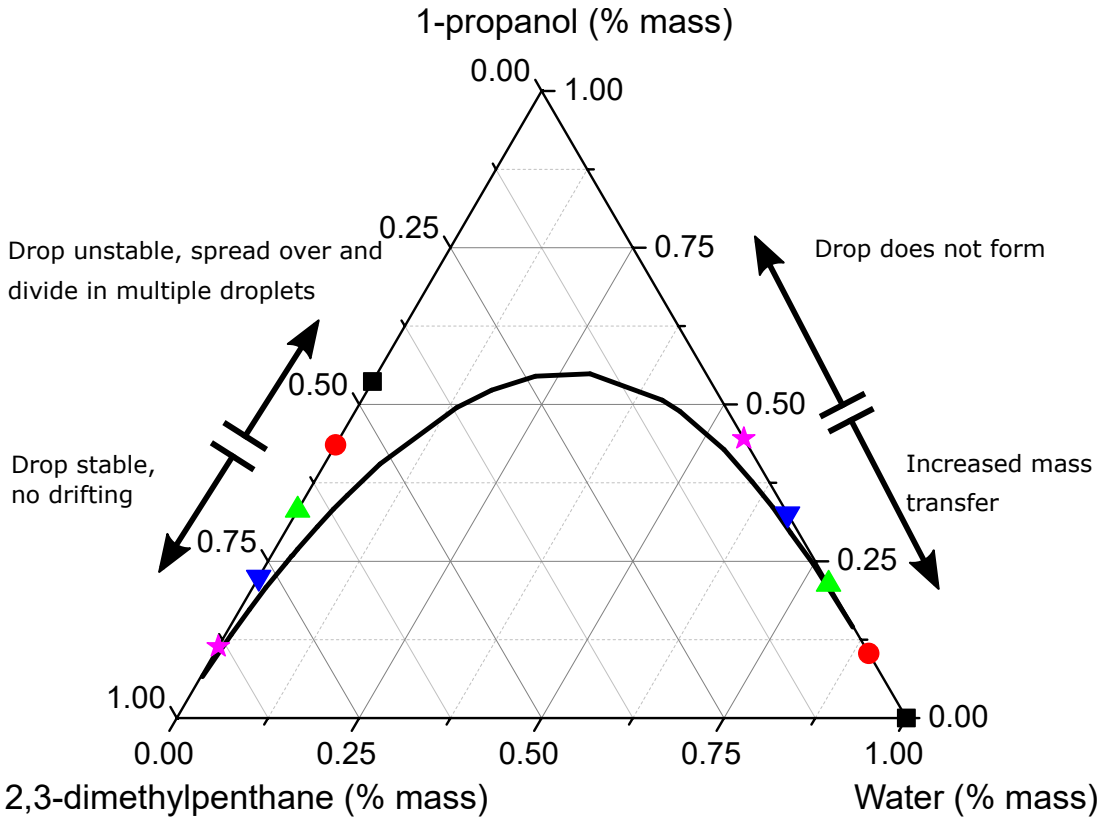

Figure 5.4 *Phase diagram for our system by weight. The black line defines the binodal curve, obtained from [139] and the composition of the pairs BATH (left axis) - DROP (right axis) contacted have being symbol&colour-coded. Arrows at the axis indicate the expected behaviour when moving along those directions.*

For high-alcohol bath compositions such as 50/50 % and 60/40 %, the injected drop was unstable and quickly spread over the cuvette, breaking into smaller droplets. Some mass transfer between the bath and the smaller droplets were observed as dark trails going into the droplets, as depicted in Figure 5.5 (b).

For lower alcohol bath concentrations, the drop remained stable without drifting inside the cuvette, although the same type of flow-trails that occurred at high-alcohol concentration baths previously shown are also present. Black streams of material moving from the edges towards the center of the injected drop can be seen in Figure 5.6 (a). According to our previous studies, we believe that the streams are spontaneously formed alkane-rich droplets whose movement is driven by the

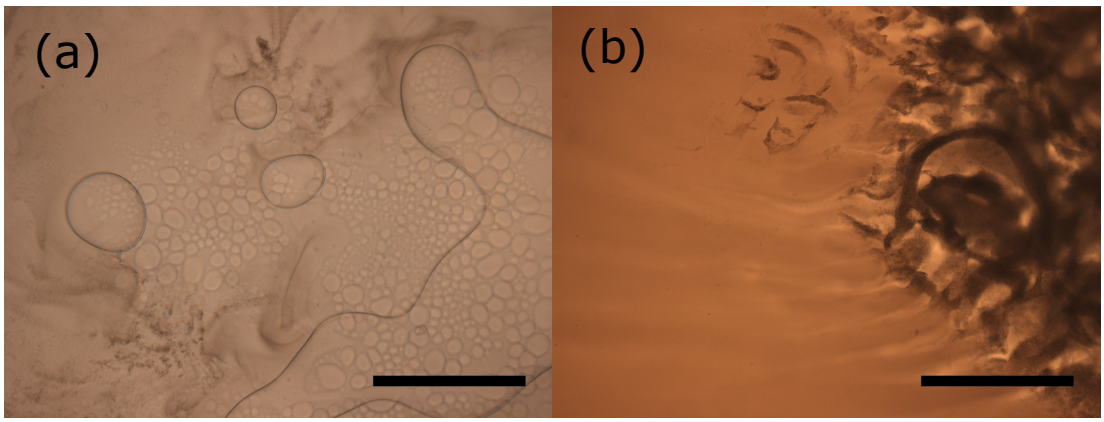

Figure 5.5 *Bright field images with a ×4 objective shortly after injecting the drop. In (a), drops broken off from the injected drop are shown in a very dynamic environment. At (b), mass transfer can be seen by the light-coloured trails near the drop. Bath composition as 2,3-dimethylpentane/1-propanol/PMMA (in volume) was (a) 60/40/0.2 % and (b) 60/40/2 %. Drop composition as water/1-propanol was in both cases 87.5/12.5. Scale bars are 500 µm*

alcohol concentration gradient. Confocal microscopy reveal non-fluorescent flows going out of the drop, which would indicate the presence of water being poured from the droplet into the bath (see Figure 5.6 (b)).

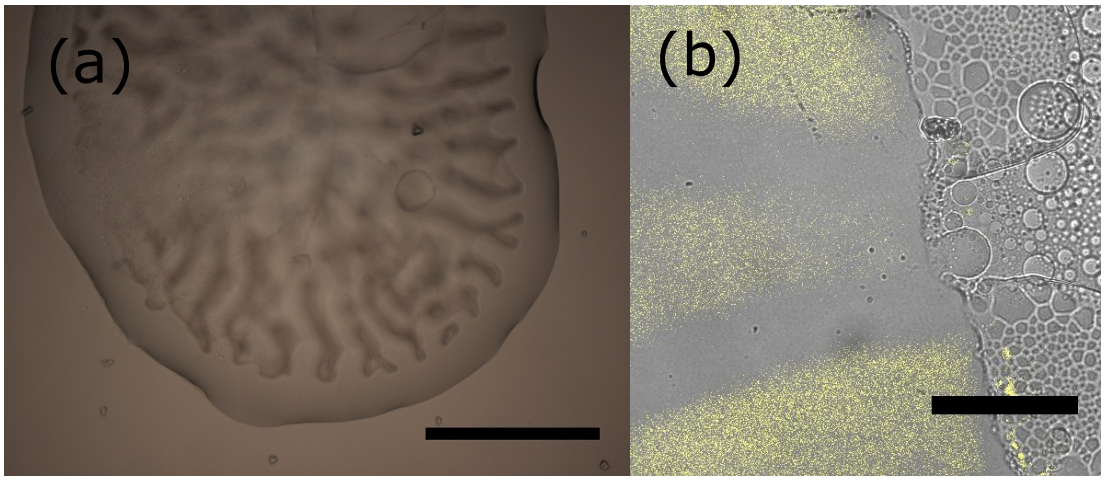

Figure 5.6 *At (a), a lower magnification image on a more alcohol-rich drop shows the presence of several fingers radially oriented. At (b), a CSLM composed image of both channels clearly demonstrate the existence of a flow of water going outwards (which is not dyed, as PMMA particles are hydrophobic). Bath composition as 2,3-dimethylpentane/1-propanol/PMMA (in volume) was 90/10/2 for (a) and 80/20/0.2 % for (b), with drop compositions as water/1-propanol (in volume) being 50/50 in (a) and 62.5/37.5 % in (b). Scale bars are 500 and 200 µm, respectively.*

However, the most striking phenomenon occurring at low-alcohol bath compositions such as 80/20 % and 90/10 % is the spontaneous formation of droplets at the particle-covered interface of the injected drop, as depicted in Figure 5.7 (a). Surprisingly, smaller droplets also spawn on top of the already spawned droplets (see Figure 5.7 (b)). Although these small droplets are also present in a system with no alcohol present (the bath consisting of pure 2,3-dimethylpentane with dispersed PMMA particles and the drop being pure distilled water), the droplets are significantly fewer, smaller and evolve over time much slower. This fully supports our explanation previously laid on the previous chapters, which states that the alcohol serves to increase miscibility, and its presence, especially when gradients exist, greatly enhances the spontaneous emulsification in such systems.

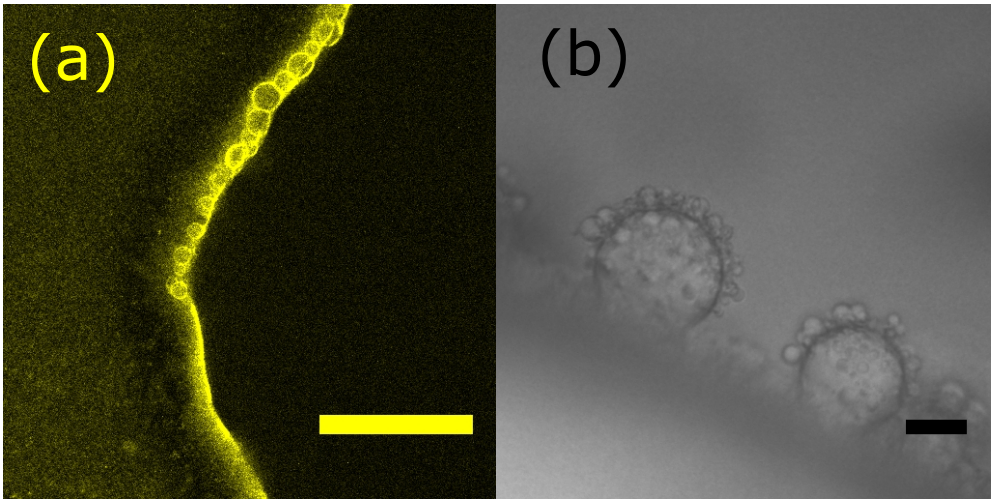

Figure 5.7 *Microscopy image showing the presence of particle-covered droplets on the rough interface of the injected drop at (a). Optical photomicrograph showing spawning droplets on spawned droplets on a pure water injected drop can be seen in (b). Bath composition as 2,3-dimethylpentane/1-propanol/PMMA (in volume) was 80/20/0.2 % in (a) and 90/10/2 % in (b), with pure water drops being injected in both cases. Scale bars are 500 and 20 μm, respectively.*

The time evolution of these droplets sitting at the interface was followed at the side of the injected drop for 20 hours, as shown in Figure 5.8. The initial frame was captured an hour after injection to have the interface hugely populated by these droplets. The growth rate is fairly slow, with the radius of the droplets evolving from $r_{1hr} \approx 4$ μm to $r_{20hr} \approx 40$ μm in a period of 19 hours.

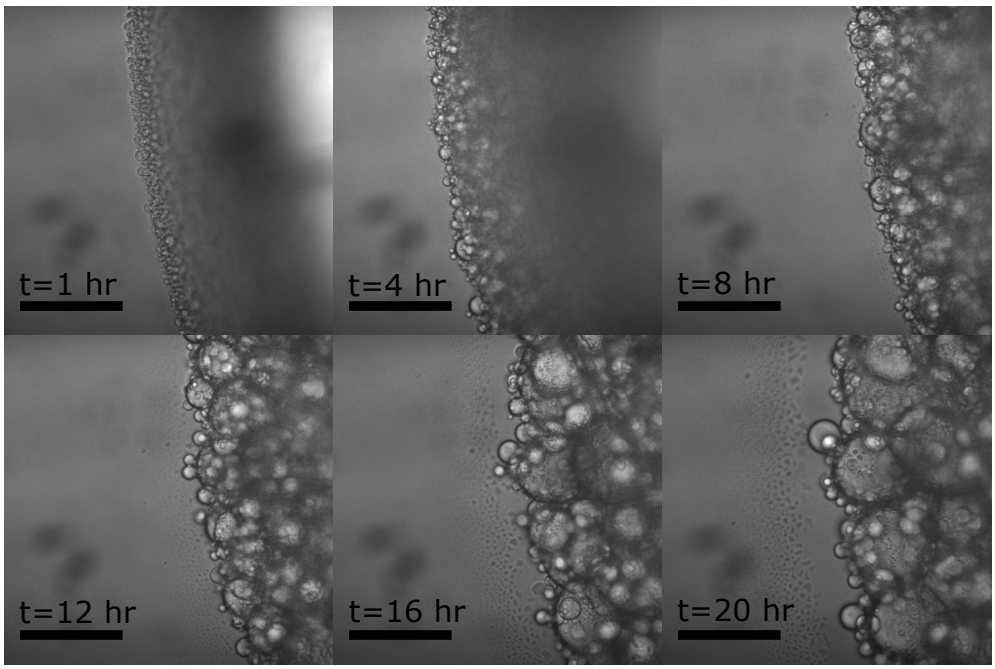

Figure 5.8 *Optical microscopy images at different times showing the evolution of the spontaneously formed droplets on the interface of the injected water drop. Bath composition as 2,3-dimethylpentane/1-propanol/PMMA (in volume) was 90/10/1 %. Scale bars are 100 μm.*

By using confocal microscopy, we recorded the surface of the drop along the Z-axis, which has been represented in Figure 5.9. In the top row, the fluorescent images at three different heights (Z values) show that the spontaneously formed droplets at the interface of the drop are covered by the PMMA particles dispersed in the bath. The bottom row containing the optical microscopy images show that these droplets are formed all over the drop, not only at the equator.

At short times, when there were not such a huge number of droplets, we could easily locate and track small droplets emerging at the center of the drop. These droplets would spontaneously form and grow. Although some of the smaller droplets move under Brownian motion, they usually remain motionless until they coalesce with a nearby droplet. Employing PMMA particles larger than usual, with a radius ≈ 500 nm, we have followed the time evolution of a coalescence event between two droplets, occurring at the center of the drop depicted in Figure 5.10. We observe how even when the droplets are covered by particles, they are able to coalesce and grow, which hints us towards an instability due to a continuous droplet growth. This growth, which will give rise to exposed regions on the droplet surface, could be caused by compositional ripening, as in our previous

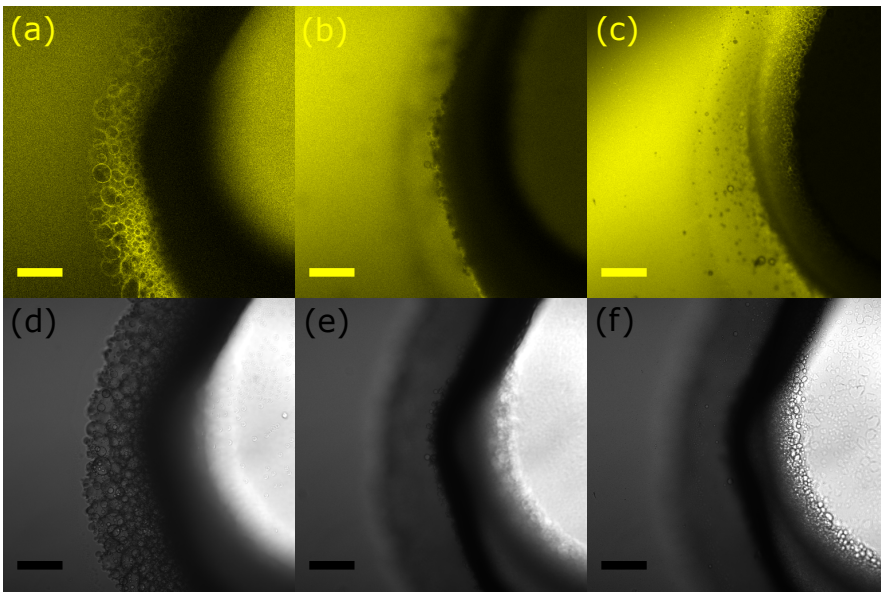

Figure 5.9 *Fluorescent (a-c) and optical (d-f) images on the side-interface at different heights of the drop corresponding to the experiment depicted in Figure 5.8. We can observe how the formed droplets are covered by particles, and that the whole interface of the injected drop seems to be covered by droplets. Bath composition as 2,3-dimethylpentane/1-propanol/PMMA (in volume) was 90/10/1 %. Scale bars are 200 μm.*

experiments in other chapters.

The time evolution of the projected area of the center droplets that coalesce in Figure 5.10 has been plotted in Figure 5.11 (a) along with the data obtained from another experiment with significantly bigger droplets (an order of magnitud) in Fig. 5.11 (b). In both cases the area increases linearly with time until they coalesce, and we have marked with a red star the sum of the areas of both droplets, which confirms that the coalesced drop area is indeed originating from the merge of those initial droplets.

We believe coalescence between droplets occurs through the gaps in their interface not covered by particles that were created during their expansion. An oversimplificated explanation for this can be deduced geometrically from the cartoon depicted in Figure 5.12. We have represented the area (scaled) of the two droplets whose numerical data has been plotted in Fig. 5.11 (a) at two times. First, when they were detected 10 minutes after injection, and 25 minutes later just before coalescence. Assuming the droplets were completely covered by particles at the beginning, if no (or very few) particles become attached to the expanding interface, there would be a sufficiently exposed area through which

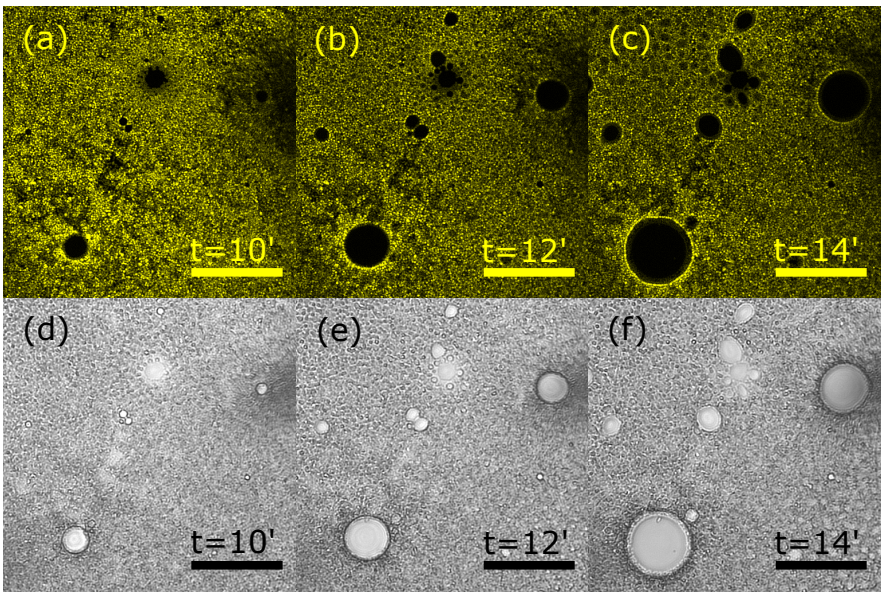

Figure 5.10 *Fluorescent (a-c) and optical (d-f) images on the center of the drop. We can observe how several spontaneously formed droplets are covered by fluorescent PMMA particles, although it does not inhibit coalescence between droplets nor its growth, pointing towards a type of compositional ripening. Bath composition as 2,3-dimethylpentane/1-propanol/PMMA (in volume) was 90/10/2 %. In this case, to observe the PMMA in more detail, larger particles were used. Its radius was ≈ 500 nm, 5 times larger than the size normally employed. Scale bars are 50 µm.*

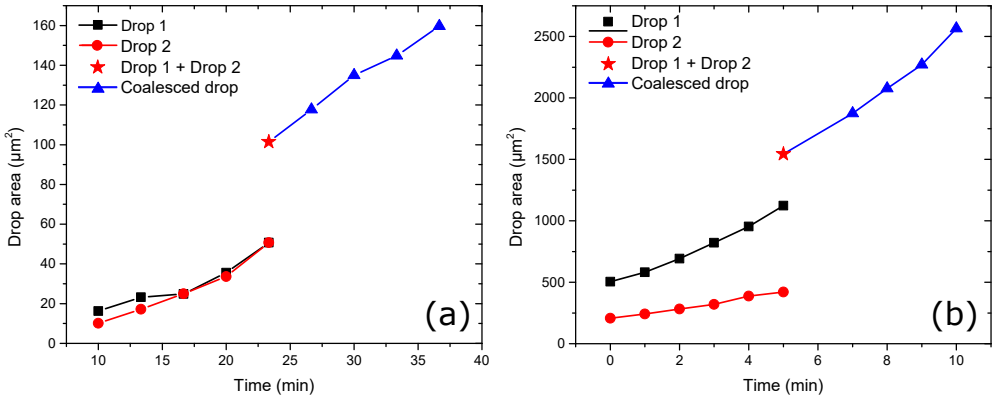

Figure 5.11 *The area of two drops before and after coalescing has been followed over time in two different experiments. The sum of the drops just before coalescing has been represented as a red star. Bath composition as 2,3-dimethylpentane/1-propanol/PMMA (in volume) was 90/10/2 % with larger PMMA particles, whose radius was ≈ 500 nm. (a) corresponds to the experiment depicted in Figure 5.10, whereas (b) starts with significantly bigger droplets (about 25 times larger area).*

coalescence can occur.

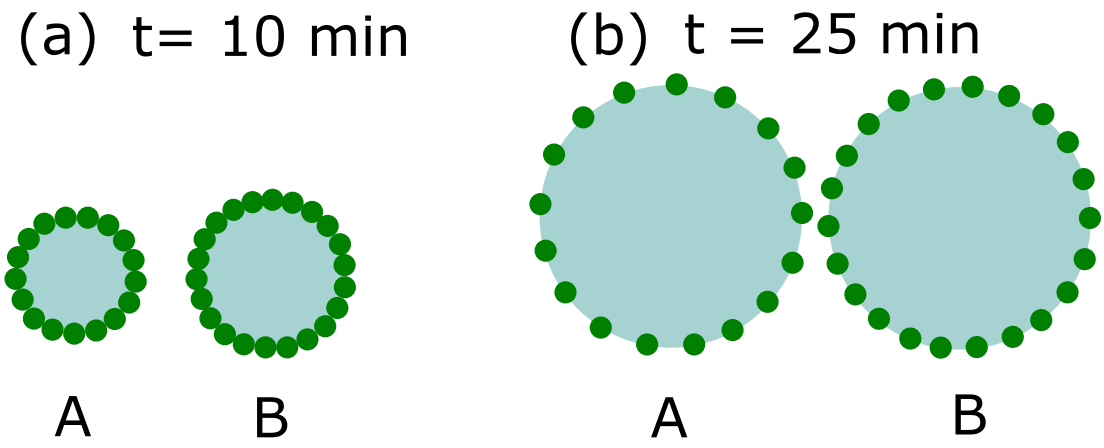

Figure 5.12 *Cartoon showing the area of the two droplets (areas are scaled to the experiment shown in Fig. 5.11 (a)), A and B, (a) when they were first detected (10 minutes after injection) assuming their whole surface is covered by particles (particles' size is not in scale for clarity), and (b) just before coalescence (25 minutes after injection) assuming the number of particles remains unchanged. This oversimplified explanation serves to illustrate how coalescence through the exposed surface in the swollen droplets may occur.*

In some cases, spontaneously formed droplets were observed to share particles on their interface with other droplets. This hindered the coalescence between them up to a certain point, delaying it by minutes. Examples of these have been included in Fig. 5.13. By measuring the thickness of the interfacial layer ($\sim$1 μm) and comparing it with the particles' diameter (d$\sim$1 μm) we could confirm that a single-particle layer between the droplets is present, with both droplets sharing the particles. The rest of the particle-covered interface is able to maintain the previous shape of the droplets after they coalesced.

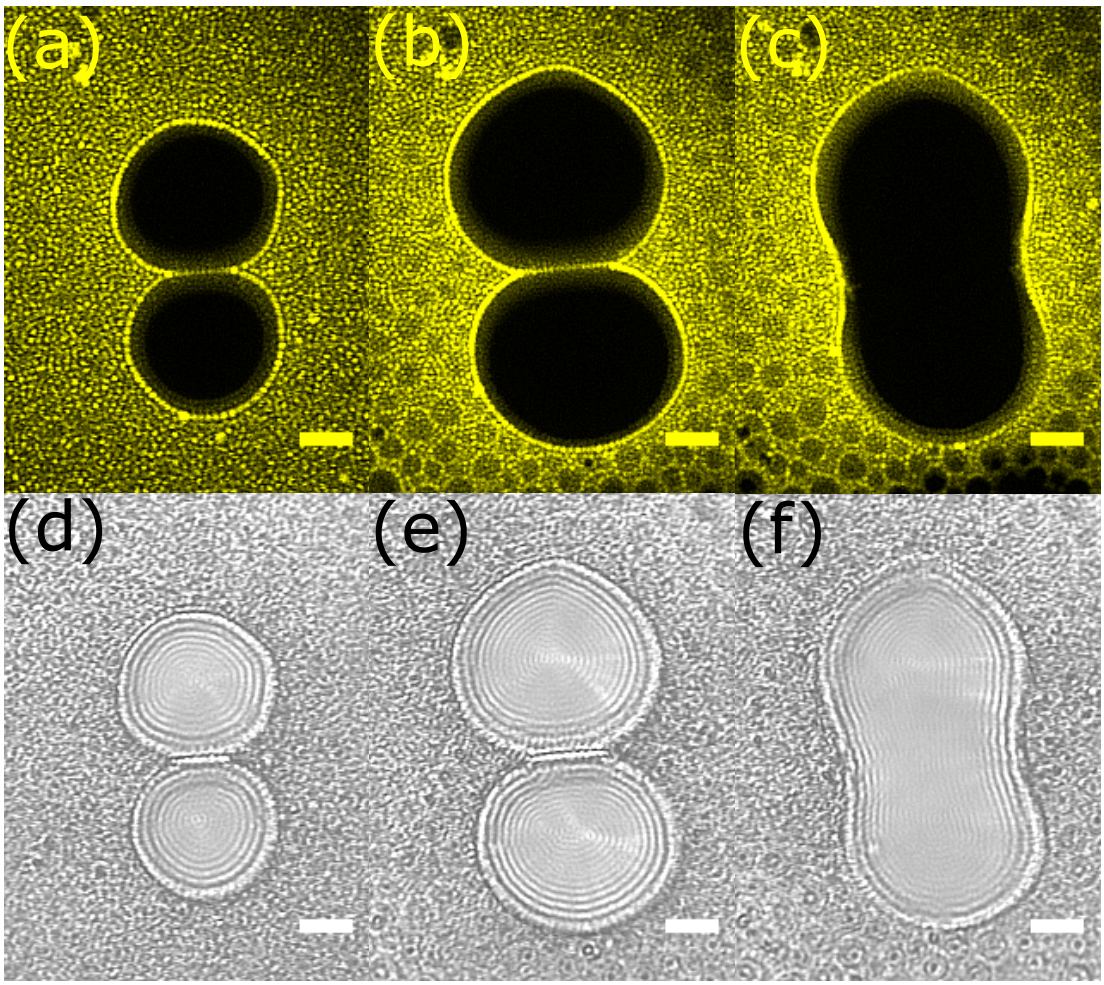

Figure 5.13 *(a,d) show two droplets spontaneously formed at the center surface of the water drop injected 10 minutes before. (b,e) images were taken 25 minutes later and the swollen droplets continue to share a thin layer of particles. (c,f) images, just a minute after (b,e), show the coalesced drop, although their particle-covered interface is able to maintain their previous shape temporarily. Bath composition as 2,3-dimethylpentane/1-propanol/PMMA (in volume) was 90/10/2 % with larger PMMA particles, whose radius was* $\approx$ *500 nm. Scale bars are 10* μm.

As previously mentioned, the particle-covered interfaces are able to maintain their original shape after coalescencing. More examples of these can be found in Fig. 5.14. We believe that, although most of the interface is covered with particles as easily observed in any of the previous confocal images, a partial coverage of the interface is not enough to inhibit coalescence. Nevertheless, it is able to delay that phenomenon and retain the original shape of the droplets momentarily.

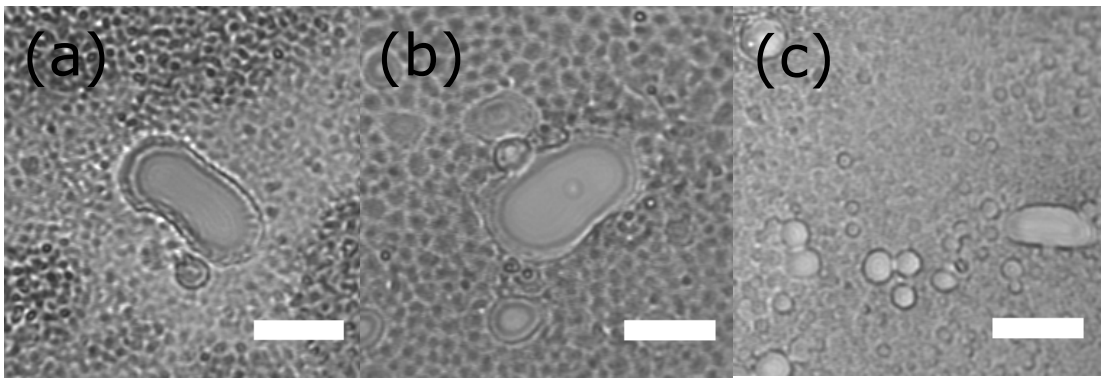

Figure 5.14 *Optical microscopy images shortly after the coalescence of two spontaneously formed droplets at the surface in the center of an injected water drop on three different experiments. For these experiments, the coalesced drop is able to maintain the original shape of the former droplets for a while, lastly achieving an spherical shape. Bath composition as 2,3-dimethylpentane/1-propanol/PMMA (in volume) was 90/10/2 % with larger PMMA particles, whose radius was ≈ 500 nm. Scale bars are 20 µm.*

Besides their ability to delay coalescence between spontaneously formed droplets, the particles seem to be incapable of avoiding droplet dissolution back to the injected water drop from which they spawned. This has been observed repeatedly for different droplet's size on the microscope, which gives the impression that the droplet suddenly "vanished". In some cases the droplet leaves a water-rich patch, identifiable by using confocal microscopy, as in Fig. 5.15, although it is not always the case (Fig. 5.16 (b,c))

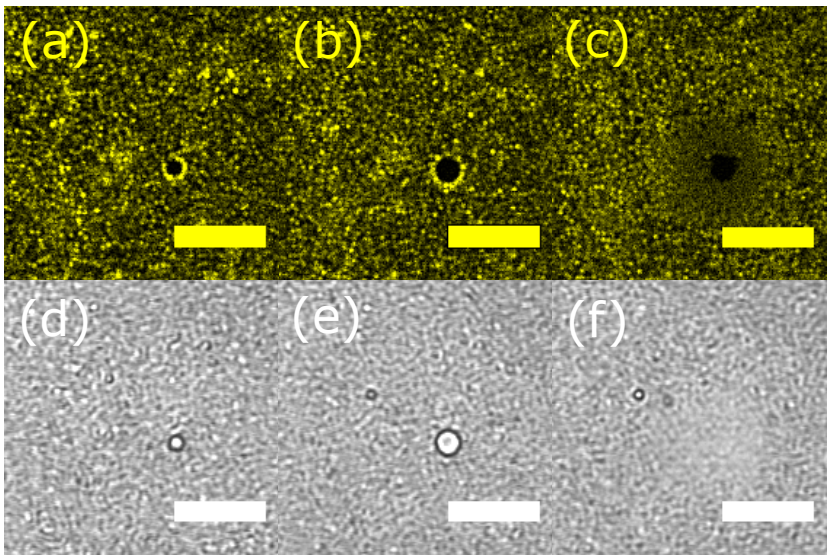

Figure 5.15 *(a,d) show a single spontaneously formed droplet at the center of the surface of the water drop injected earlier. (b,e) after 4 minutes the droplet has grown considerably. (c,f) are just 20 seconds later and a dark patch (a water-rich area) can be observed on the fluorescence channel, showing as a blurry patch on the bright field channel. Bath composition as 2,3-dimethylpentane/1-propanol/PMMA (in volume) was 90/10/2 % with PMMA particles whose radius was ≈ 500 nm. Scale bars are 20 μm.*

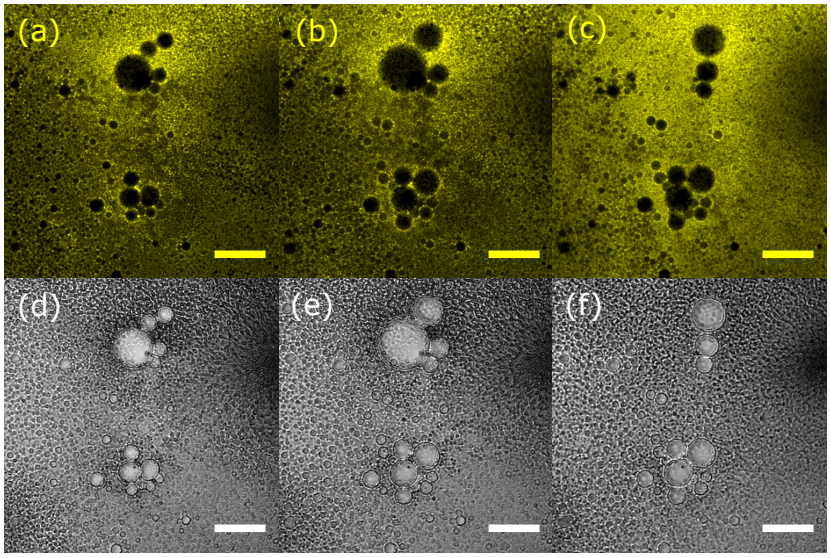

Figure 5.16 *(a,d) show two clusters of spontaneously formed droplets at the center of the surface of a water drop previously injected. (b,e) 54 minutes later show a generalized growth with some coalescence occuring. (c,f) images after 20 seconds indicate that the the biggest top droplet has redissolved. Bath composition as 2,3-dimethylpentane/1-propanol/PMMA (in volume) was 90/10/2 % with PMMA particles whose radius was ≈ 500 nm. Scale bars are 30 μm.*

The projected area of these spontaneously formed droplets and its evolution over time using PMMA particles with different sizes, with no appreciable differences between them, as can be observed in Figure 5.17. The droplets were covered by particles in all cases, with plenty of extra particles in the bath to cover the new exposed, expanded area.

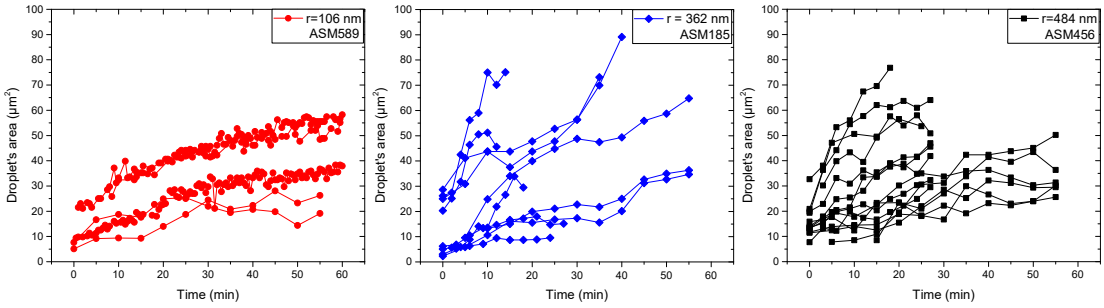

Figure 5.17 *Projected area of 30 spontaneously formed droplets over time recorded at the center of the injected drop. Using the same experimental setup, only the size of the PMMA particles were varied, with radius ranging from 100 to 500 nm.*

5.3.2 Dewetting phenomenon

Another curious phenomenon we found in this system occurred when we removed the alcohol (1-propanol) from our system. Hence having a bath solution formed by the alkane 2,3-dimethylpentane with PMMA particles dissolved in it, we injected a pure water drop in a cuvette filled with said bath solution.

Looking at the interface near the glass (the cuvette has a 1 mm height, thus making our injected drops in contact with both sides of the cuvette, top and bottom) we could observethea curious dewetting pattern shown in Fig. 5.18. These dewetting patterns are very similar to those observed in Hele-Shaw cells, where the fingers advance through tip-splitting themselves. [163] This phenomenon originates from the rim, pointed by a yellow arrow, which indicates the part of the drop in physical contact with the glass. A slight tilting of the cuvette due to experimental constraints produced uneven illumination in some of the fluorescent images when using low magnification objectives ($\times 10$).

This pattern was in some occasions observed only at one surface, usually at the bottom, but at times it was possible to discern the patterns at both interfaces (top and bottom of the cuvette) at the same time. Using a confocal microscope to measure the distance along the Z axis (depth) between those interfaces yielded a

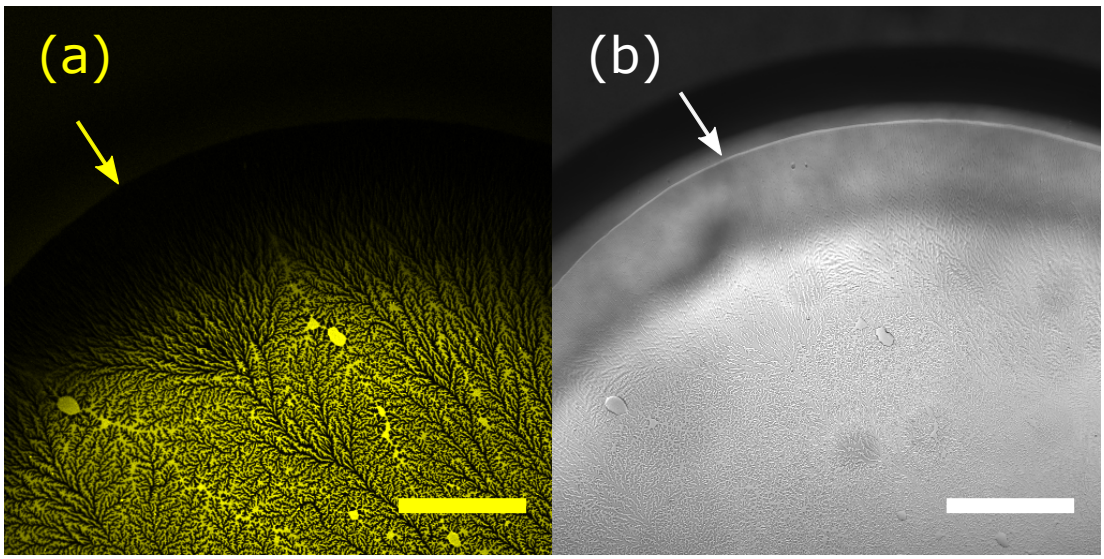

Figure 5.18 *Fluorescent (a) and bright field (b) images of the dewetting phenomenon observed when injecting a water drop in a solution of 2,3-dimethylpentane with 1%vol PMMA particles whose radius was ≈ 100 nm. Arrows point at the rim of the drop in direct contact with the glass surface of the cuvette. The fingering always starts from this rim. Scale bars are 300 µm.*

value approximately the height of the cuvette. In Figure 5.19 dewetting patterns could be observed both at the top and bottom surfaces of the cuvette, with a noticeably larger amount of particles deposited in the bottom.

We have studied how variations in the PMMA particles' size (we have used three different sizes, with a radius ≈ 100, 350 and 500 nm) and its concentrations (ranging from 0.1 to 5% in volume) affects this dewetting phenomenon. First, it is worth noting that these dewetting patterns occur very rapidly after injecting the drop, remaining unchanged afterwards. Smaller concentrations of particles resulted in the observed phenomenon occuring more often than with higher concentrations. This effect was completely suppressed with a 5 vol% particle concentration. This indicates that particle concentration certainly influences this phenomenon by changing the degree of particle coverage of the glass substrate. The glass surface will be more poorly covered by particles when using smaller particle concentrations in the bath. We observed that the dewetting phenomenon occurred with a higher probability for the first injected drop in each bath. This took place shortly after filling the cuvette with the bath solution, hence when the amount of substrate's surface covered by particles is low but steadily increasing by sedimentation. Fractal patterns were more probable if the drops were injected after flipping the cuvette 180°, an action that would also effectively reduce the

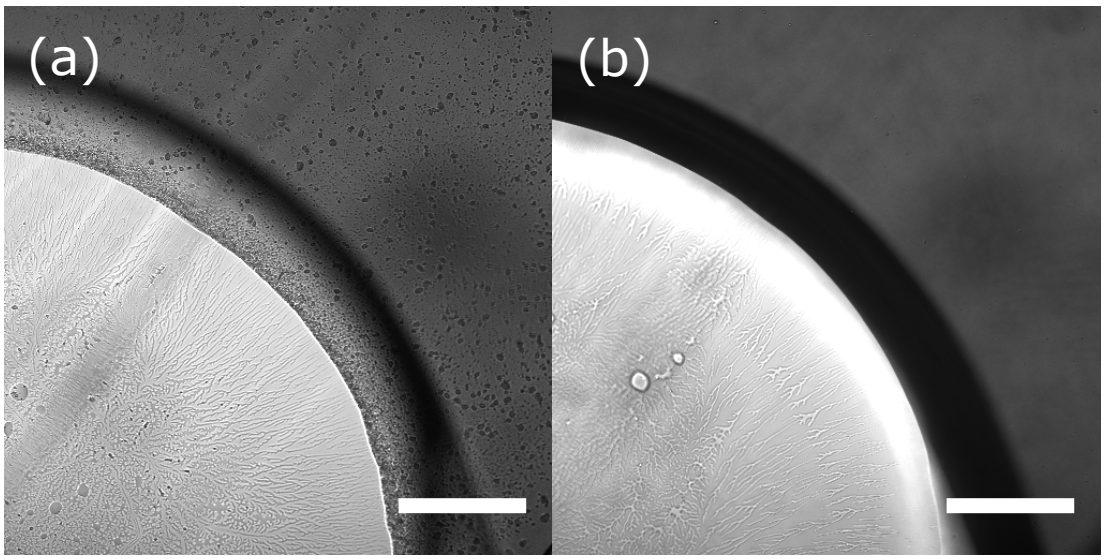

Figure 5.19 *Bright field images focused at the interface between the drop and the bottom (a) or top (b) of the cuvette. The dewetting pattern at both surfaces is simultaneous, with an increased amount of particles at the bottom surface present due to sedimentation. The bath solution in this experiment was 2,3-dimethylpentane with 0.5% vol. of PMMA particles ≈ 100 nm radius and the injected drop was distilled water. Scale bars are 300 μm.*

amount of particles on the glass substrate, because the top and bottom surfaces of the cuvette have different particles concentration due to sedimentation occuring at the bottom of the cuvette.

Our explanation for this effect is as follows: surfaces with a low amount of particles (i.e, for low concentrations - after filling the cuvette or when it has been flipped over) allows the injected water drop to wet the glass, with a following dewetting phenomenon taking place. However, an increase in the amount of PMMA particles sitting at the substrate (e.g, when the bath has a high particle concentration or if it has suffered sedimentation after some time) would make it extremely difficult for the drop to wet the glass substrate in the first place, thus not observing fractal dewetting patterns. A cartoon to show this effect has been included in Fig. 5.20. Here, the relative size of the particles to the drop has been exaggerated, whereas the amount of particles has been underestimated for the purpose of clarity.

We found significant differences in the dewetting pattern formed by varying the particles' size. When using the smallest particles, the fingers created are very thin (≈ 2 μm width) and the structures formed are highly branched. However, for the bigger particles the fingers' width ranges from a few to tens of micrometers,

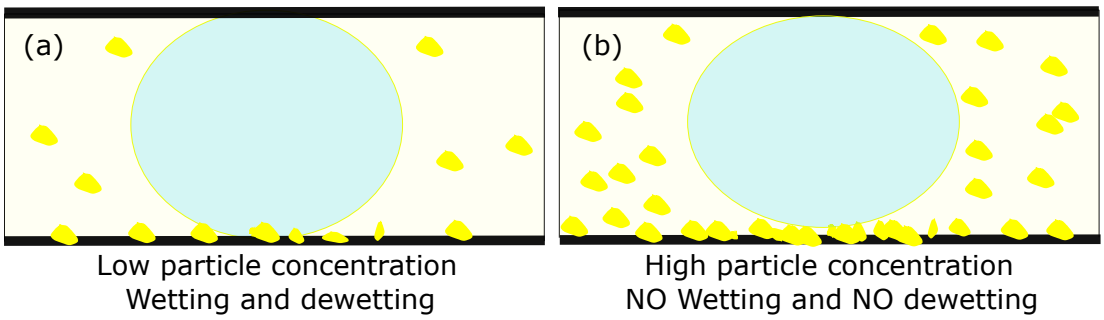

Figure 5.20 *Differences in the particle coverage of the substrate, dependent on the particle concentration, sedimentation and other factors, affect whether wetting (and subsequent dewetting) is possible in the system or not.*

with significantly less branched structures forming. Examples of these have been included in Fig. 5.21.

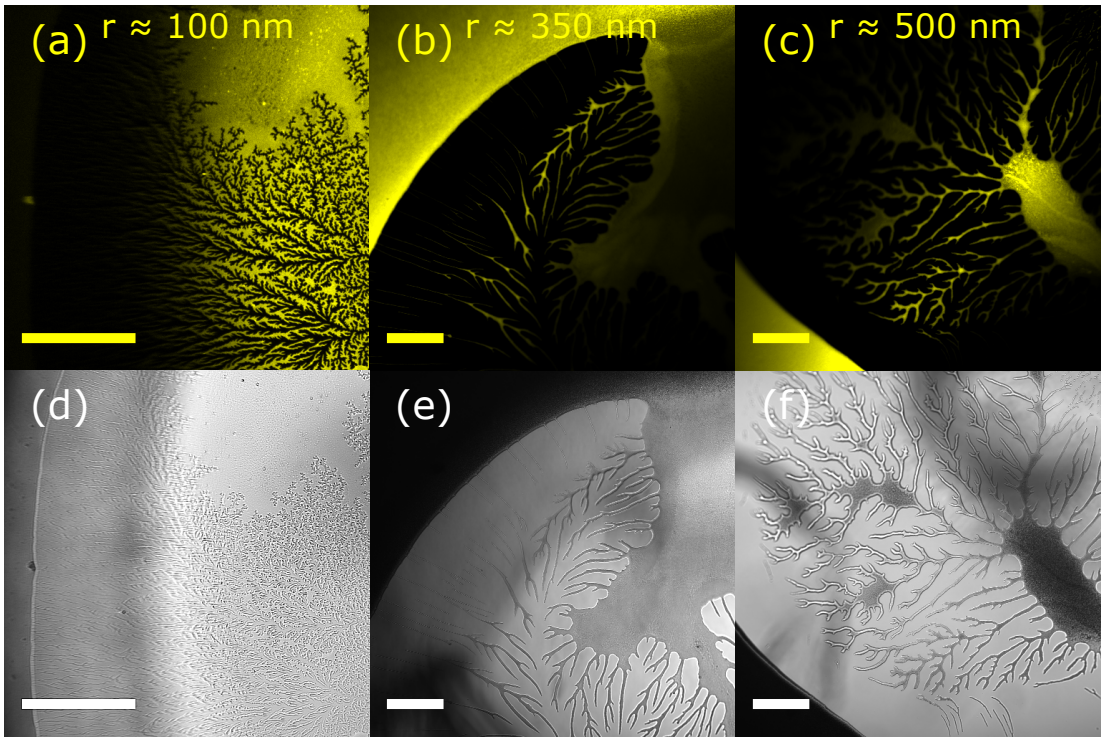

Figure 5.21 *Fluorescent (a-c) and bright field images (d-f) showing the different dewetting patterns observed. Bath solution was 2,3-dimethylpentane with 1% vol. PMMA particles with different sizes, indicated in the pictures. The smallest particles produce thin and highly branched patterns, whereas the bigger particles provoke thicker and less branched fingers. In some cases, big pockets of the alkane can be found (e,f). Scale bars are 200 µm.*

The differences in the dewetting patterns can be attributed to the size of the PMMA particles contained in the bath (oily phase). This can be easily understood

looking at the cartoon in Fig. 5.22. This cartoon tries to explain how the dewetting takes place as the oil penetrates under the drop, separating the drop interface from the glass substrate. For larger particles, the two surfaces would have to be forced further apart, resulting in increased spacing between interfaces which produces thicker fingers.

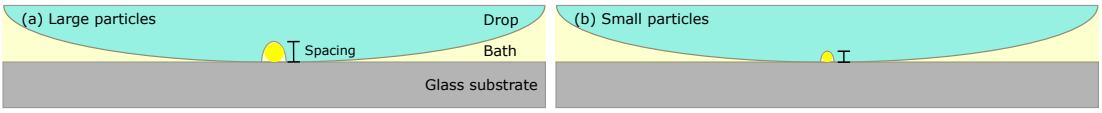

Figure 5.22 *A cartoon to explain visually how the thickness of the fingers forming in the dewetting patterns depends on the size of the particles, which modifies the spacing between the drop and the substrate.*

We have determined the "Minkowski-Bouligand" fractal dimension of the dewetting patterns formed with different particles' size. Their fractal dimension, obtained from 30 different experiments, along with an example of the type of image analyzed can be found in Fig. 5.23. Although its error, taken as the standard deviation of the different images used, is $\approx 5\%$, it seems that the smallest particles achieve the highest fractal dimension, which would correspond to a system with thinner and more branched fingers, which agrees to what we observe experimentally. For the bigger particles, their values are relatively close, and this is again in agreement with our observations, where no differences can be noticeably distinguished.

A different analysis was performed using the "Fast Fourier Transform" (FFT) algorithm and the "Radial Profile Plot" plugin included in the Fiji software (ImageJ distribution) [96]. These two transformations were applied on a rectangle selection of 256×256 pixels (half the image's length, so a quarter of the area) centered at the pattern, to avoid both issues with the thresholding method and the analysis of empty regions (outside of the drop). A profile plot of "normalized integrated intensities around concentric circles as a function of distance [...]" [172] was applied to a FFT image. The axis of abscissas of this profile plot was transformed from the given units (pixels in the FFT domain) to actual wavenumbers. To do so, the pixel size in wavenumber units is given by $2\pi/L$, where L is the size of the rectangle selection in meters. The total length of the axis in wavenumber units is now half the pixels of the selection (due to the Nyquist criterion) times the pixel size.

We have then inversed this x-axis to represent real-space distances directly,

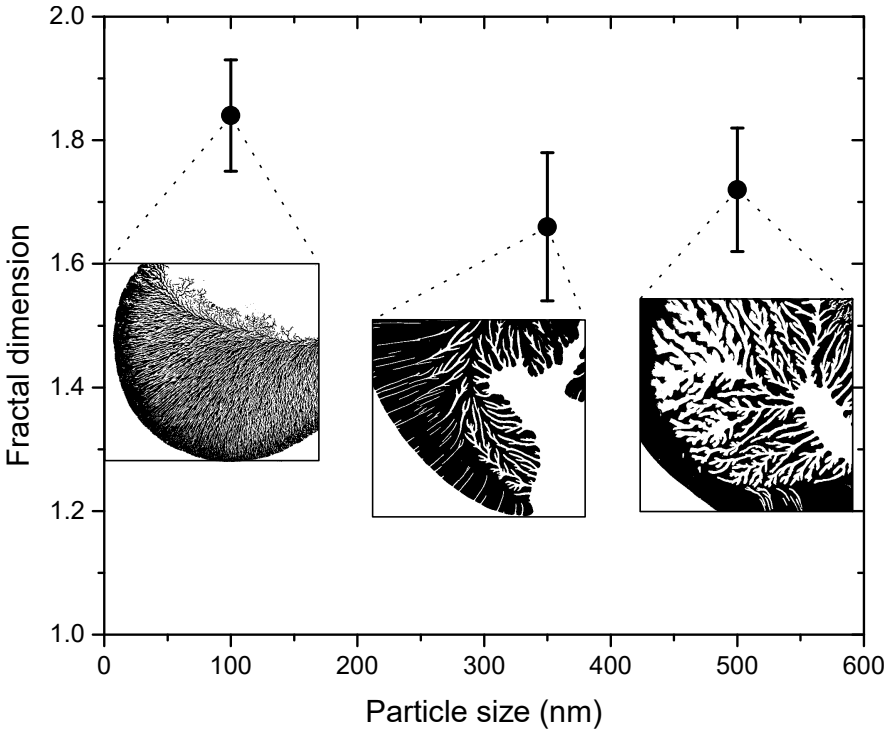

Figure 5.23 *Fractal dimension determined through our script A.3 for a set of different patterns observed for varying particles' size. Error bars represent the standard deviation for different experiments with the same composition. Inset includes representative patterns for each size.*

instead of wavenumbers, the latter being the usual representation. Figure 5.24 (a) contains an example of these plots for each particle size analyzed, whereas Figure 5.24 (b) shows graphically how the analysis to obtain a characteristic length was performed.

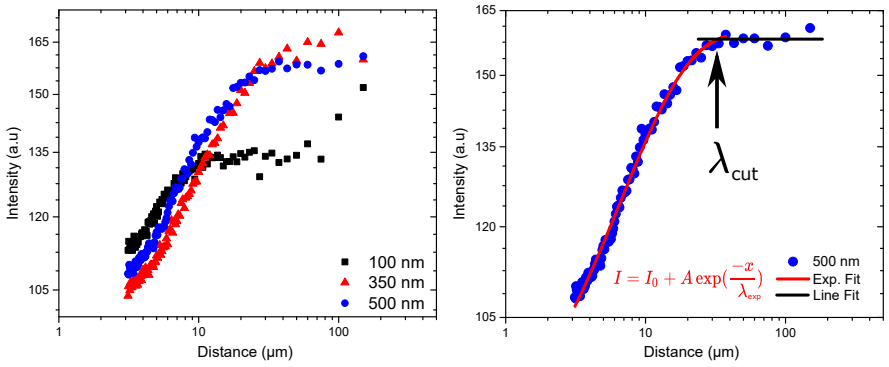

Figure 5.24 *(a) Examples of radial profile plots of Fast Fourier Transformed dewetting patterns for different particles' size. (b) Example of the analysis performed in each individual plot, with an exponential fit for short distances to obtain the λ_{exp} parameter, and a horizontal line to discern its crossing point, termed as "cutpoint" (λ_{cut}).*

For the analysis, an exponential fit to the equation $I = I_0 + A\exp(\frac{-x}{\lambda_{exp}})$ was performed up to a distance of 35 nm. Its crossing point with an horizontal line for the large-size part of the plot (above the 35 nm) has been designated as the "cutpoint", λ_{cut}. The λ_{exp} factor inside the exponential along with the previously defined λ_{cut} are experimentally obtained characteristic lengths that allow us to link the size differences observed in the dewetting patterns to the different PMMA particles size. Both these quantities have been plotted in Figure 5.25, where we can observe a similar trend for these parameters, presenting the smallest value for the smallest particle size. However, similar values, which are about ≈ 2.5 times larger than for the smallest particle size, were obtained for the intermediate and large particle size ($\approx$ 350 and 500 nm.).

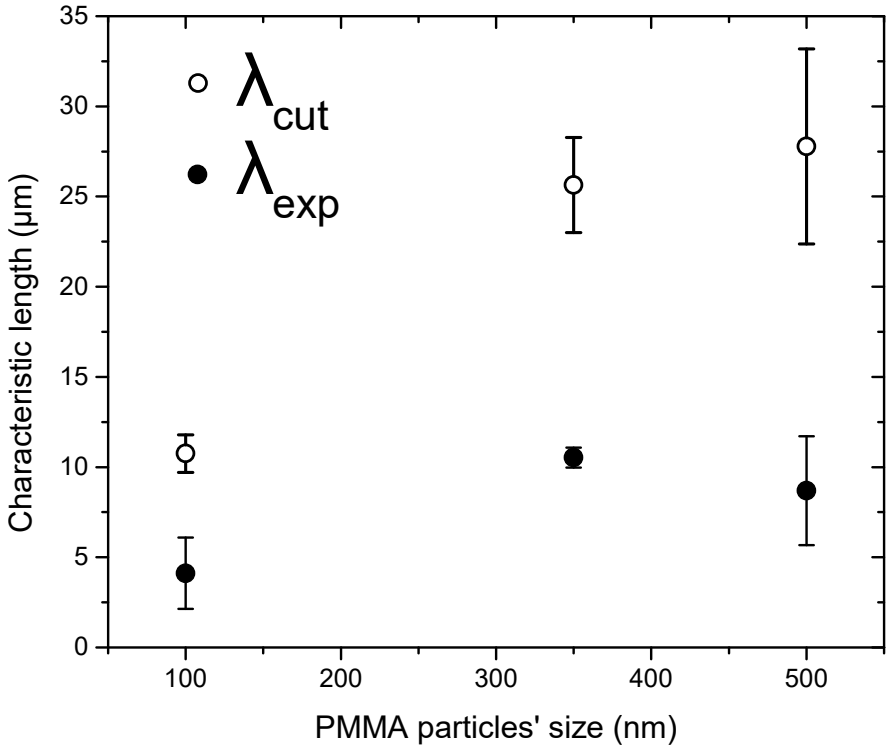

Figure 5.25 *Experimentally obtained parameters λ_{cut} (empty circles) and λ_{exp} (black filled circles) for different PMMA sizes reveal the same trend, with the smallest value corresponding to the smallest particle size, and similar values for the intermediate and largest particle size. These parameters allow us to relate the particle size with the scale of the dewetting patterns obtained.*

Finally, a collection of 18 of the analyzed dewetting pattern experiments have been collected in Fig. 5.26 by columns according to the size of the PMMA particles used. Images were treated to correct uneven background light, binarized and then thresholded to obtain clear pictures of the dewetting patterns. In these images black corresponds to water, and white to the fluorescent alkane-rich

bath solution. Outside the drop confines the colours may not be true due to thresholding artifacts. The amount of drop in contact with the cuvette (which would appear as black) varies, and we have both experiments where the drop stays stuck firmly against the cuvette (black background with white fingers, like in the second column, rows 2, 3 and 4) or those where the drop is only in contact with the cuvette slightly by the dewetting area (white background with black fingers, as in second column, rows 5 and 6).

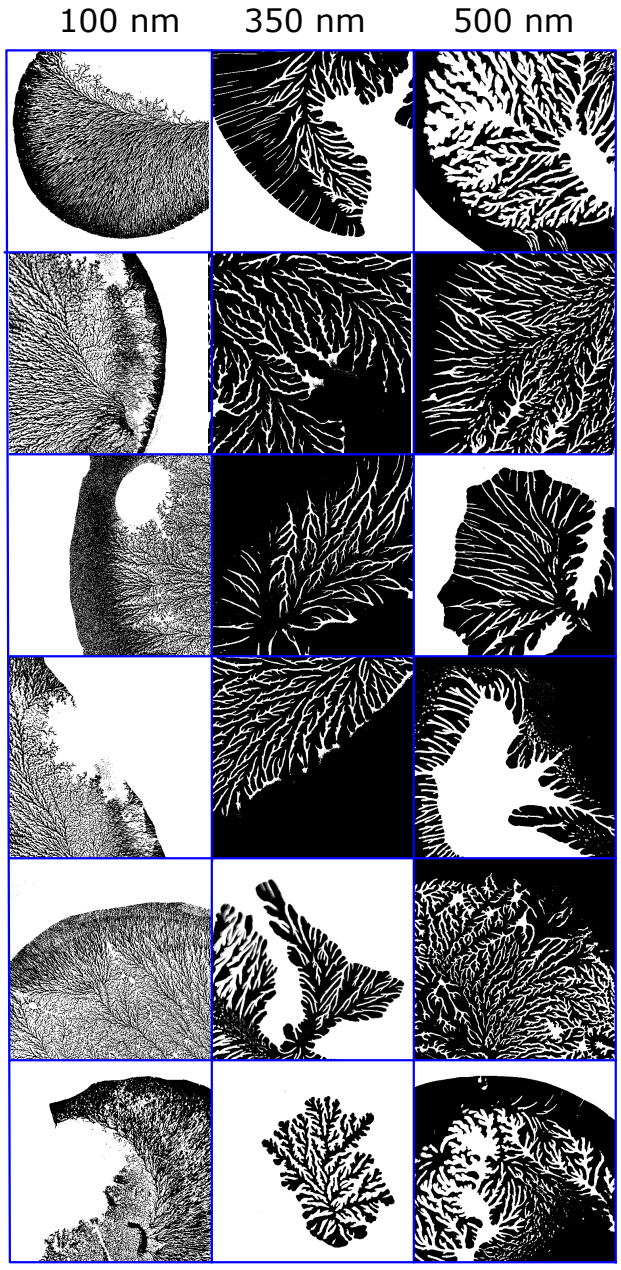

Figure 5.26 *Montage with several of the analyzed images of fractal dewetting, displayed in columns by the particle size employed. Water is represented in black, whereas the bath solution appears white. For scale purposes, a side of an image is 1.28 mm.*

5.4 Conclusions and future work

In this chapter we have used a chemically different system, which exhibits the same type of ternary diagram than in our previous chapters, to discern whether all the previously described features would still apply. Even when effects such as droplet bridging were not observed, we discovered some novel and interesting phenomena such as the "fractal-like" spontaneous formation of droplets onto droplets onto an injected water drop and the fractal dewetting patterns observed at the drop interface in contact with the glass substrate of the cuvette.

We first started by exploring the ternary diagram of this new system and studying the stability of the drop for several compositions. As expected, low alcohol concentrations both in the bath and the drop produced the more stable systems as miscibility is reduced, although alcohol presence is helpful to reduce diffusion times for the same reason.

The spontaneously formed droplets, although covered with particles, experienced ripening and coalescence, with a variety of effects such as particle-sharing ("bridging" between droplets), irregular shapes of coalesced droplets and the sudden redissolution of these droplets into the injected drop.

In the absence of alcohol, the system presented yet another curious phenomenon described in this chapter as fractal dewetting. "Fingers" of bath solution penetrated above and below the drop, creating fractal-type structures. Because this phenomenon relies on a low particle coverage of the substrate, an increase in the amount of particles in the bath solution above 5% suppresses this effect. Altering the surface chemistry of either the particles or the substrate may prove useful to confirm this, or to produce an alternative explanation.

We found these patterns to be different according to the size of the particles present in the bath. Smaller particles produced thinner, more branched structures, whereas larger particles gave wider and less surface-covering fractals. Future work using a wider range of particles, both smaller and bigger, can help understand and confirm some of the explanations laid out in this chapter. The fractal dimension of these structures were determined and by using radial profiling on the Fast Fourier Transformed images we were able to characterize these differences in the patterns according to the size of the particles used.

Chapter 6

Conclusions and future work

Different oil-alcohol-water systems with similar ternary phase diagrams have been studied in this work. The existence of spontaneous emulsification in the three studied systems for our selected compositions produced a range of phenomena, which we have characterized with different experimental techniques to obtain a deeper understanding of its mechanisms.

Chapter 3 starts exploring a system where tube sprouting from water drops was originally reported. [15] By modifying the experimental conditions of the experiment, so as to create a composition gradient by introducing a new drop with different alcohol concentration, we observed a self-assembling structure made of spontaneously formed droplets in the bath caused by the diffusion of water. Solid particles in the bath act both as nucleation sites for these droplets and form a gel which holds the droplets in place. These tiny droplets that form such structures were studied in detail using different microscopies, the time evolution and dependence on particle concentration obtained, and the behaviour related to the ternary phase diagram of the system.

Exploring different gradients between the drops may prove useful to further relate the diffusion dynamics to the existing compositional ripening. The use of different particles, to explore both different sizes and surface chemistries, may produce a more complete explanation of the bridge formation dynamics. Due to the phenomena observed at later times and the gellation of the bath, rheological studies on aging solutions would be a natural step to further characterize the system.

The knowledge of the amount of each element diffusing would enable us to calculate multi-component diffusion coefficients, which are often undetermined due to experimental difficulties obtaining them. For this reason, the best and most important addition to this work as a whole would be to devise a method to measure the three components concentration at the same time. Experimentally, we were unable to determine the toluene concentration, thus finding a suitable alternative oil that produces the same phenomena (spontaneous emulsification) with its Raman spectrum not overlapping with the alcohol signal would be beneficial. Knowing the full composition of either the drop or bath, or both, at different times would be the final confirmation for our proposed diffusion pathways, which would validate our code to simulate further systems.

Chapter 4 uses a slightly modified version of the previous system, by switching the ethanol for methanol. In this chapter we were interested in the diffusion dynamics concerning a single drop, thus obtaining the volume evolution of several drops with different initial compositions. This simple analysis yielded several quantitative parameters that proved useful to, again, relate the observed behaviour to the diffusion paths plotted in its ternary phase diagram. Another simple, yet useful approach was the use of solvatochromic dyes to track the diffusion flows occurring during the experiment. Reichardt's dye proved immensely useful because of its huge colour variations even with small compositions changes (1% changes in solvent resulted in colour changes discernible by the naked-eye for the bath solution, for example). Using this dye in particle-less systems also uncovered the presence of Marangoni flows, which were either concealed or prevented by the presence of the particles.

The use of different alcohols to make a complete picture of the relationship between simulated diffusion paths and experimental observations is the logical next step to extend this work. Inverse systems (oil-in-water emulsions) can broaden the amount of elegible alcohols to the ones that partition preferentially into the oily phase. From an environmental point of view, these type of inverse systems are becoming increasingly important. These type of systems are also preferred from an manufacturing point of view, since water is abundant, cheap, and non toxic. Therefore, the possibility of having emulsions with water as the continuous phase is almost always desirable. Thus, researching whether these inverse systems present the same phenomena as described in our work and if they can be analysed in the same way or not would can increase the applicability of this work hugely.

The application of H. Tan's model (a "one-dimensional multiphase and multicomponent diffusion model, which incorporates thermodynamical equilibrium theory and diffusion path theory" [103]) to our system can help to validate the model and produce comparable quantitative results for our system. Lastly, using a different solvatochromic (less hydrophobic) dye could be helpful to unveil additional features.

Both Chapter 3 and 4 experience strong Marangoni flows. This has been shown both as a "vortex" at the drop's interface at later times through which droplets penetrate (see Figure 3.21), or at the apex of the drop in the single-drop experiments (in Figure 4.13). Time permitting, I would have liked to dwell into this different phenomena that stem from the same effect. For example, by analyzing the relative contributions of buoyancy-driven flows to Marangoni flows (which could be quantified with a type of Bond number).

Chapter 5 presents the work done on a chemically completely different system, where the bridging and extensive emulsification observed in our previous work was not observed. However, a more fascinating spontaneous emulsification results at the interface of the injected water drop, where said interface gets completely covered by spontaneously formed droplets that, although partially stabilized by particles, grow and coalesce over time. Different features of these droplets, which in turn have other droplets spawning on their interfaces, were studied using confocal microscopy. For our range of particles' sizes, no discernible differences were observed. When no alcohol is present in the system, fractal dewetting occurring at the glass surface of the cuvette containing the experiment is observed. This striking phenomenon produced different patterns according to the particles' size employed. These patterns were characterized by its fractal dimension, although differences are small.

Broadening the range of particles' size used may result in larger and easier quantification differences. Modifying the surface chemistry of the particles and/or the substrate could help to explain the dewetting phenomenon.

Appendix A

Python scripts used

A.1 Scripts used for Raman analysis

For the Figures containing drops' concentration of water and alcohol versus time in Chapters 2 and 3, we have used the following scripts to transform our raw inputs to useful concentration values.

The code used to determine the area of the peaks for a set concentration, which will be needed later to obtain a calibration curve is listed in Listing A.1

```
"""
Obtain the area of the ethanol and water peaks for a set
    concentration in the initial drop.
"""
import numpy as np
from scipy.integrate import simps
import matplotlib.pyplot as plt
#Import spectra for a known concentration
a = np.loadtxt("9010concentration.txt")
#Plot Raman spectrum of the imported data
x = a[:,0]
y = a[:,1]
plt.ylabel('Intensities (a.u)')
plt.xlabel('Raman shift (cm-1')
plt.plot(x,y,'r-')
plt.show()

def INTEGRATE(x,y):
```

```
    #Define the backgrounf divided in two parts, before the ethanol
    peak (low) and after the water peak (high)
    ind_bg_low = (x > 2000.0) & (x < 2600.0)
    ind_bg_high = (x > 3750.0) & (x < 4000.0)

    #Redefine x,y as the background values
    x_bg = np.concatenate((x[ind_bg_low],x[ind_bg_high]))
    y_bg = np.concatenate((y[ind_bg_low],y[ind_bg_high]))

    #Fit values to a polynomial degree 2 fit.
    z = np.polyfit(x_bg, y_bg, 2)
    p = np.poly1d(z)
    y_corrected=y-p(x)

    #Define the limits for the ethanol peak
    x_int = (x > 2782.0) & (x < 3020.)
    x_short=x[x_int]
    y_short=y_corrected[x_int]
    plt.title('Ethanol peaks')
    plt.ylabel('Intensities (a.u)')
    plt.xlabel('Raman shift (cm-1')
    plt.plot(x_short,y_short,'r-')
    plt.show()
    #Integrate the area in those limits to obtain the area of the
    peak
    areaEtOH = simps(y_short,x_short)

    #Same for water peak
    x_int = (x > 3089.0) & (x < 3800.0)
    x_short=x[x_int]
    y_short=y_corrected[x_int]
    plt.title('Water peak')
    plt.ylabel('Intensities (a.u)')
    plt.xlabel('Raman shift (cm-1')
    plt.plot(x_short,y_short,'r-')
    plt.show()
    areaH2O = simps(y_short,x_short)
    return areaH2O,areaEtOH;
print(INTEGRATE(x,y))
```

Listing A.1: Code to obtain the area of the alcohol and water peaks on a known concentration drop.

To obtain a calibration curve, we have previously obtained the areas of the water and ethanol peaks, and now we have linearly fitted them versus the known

concentrations at which they were obtain to obtain the slope that relates them. This code is listed the code in Listing A.2

```
"""
Given the ratio of concentrations and integrated areas we obtain a linear fit
to relate them.
"""
import numpy as np
import matplotlib.pyplot as plt
#Values for the integrated areas of the water and ethanol peak at different ratios of initial concentration in the drop.
water=np.asarray([340.96,192.75,105.05,207.07,266.22,320.17,87.55,262.61,46.97])
ethanol=np.asarray([34.452,17.69,15.668,29.16,49.41,93.66,35.53,147.39,67.44])
ratioArea=water/ethanol
ratioConc=np.asarray([9,8,7.5,6,4,2.33,1.5,1.,.25])

#Obtain linear fit, store its values and obtain points to plot the fit
#Fit ratioArea versus ratioConc and save slope [0][0].
newfit=np.linalg.lstsq(ratioArea.reshape(-1,1),ratioConc)[0][0]
#Structure to obtain the r2 value-
A = np.vstack((ratioArea, np.ones(len(ratioConc)))).T
model, resid = np.linalg.lstsq(A, ratioConc)[:2]
r2 = 1 - resid / (ratioConc.size * ratioConc.var())
#Add intercept zero to p1 to have a function to pass values and plot the fit.
z_zero=np.append(np.asarray(newfit),0)
p1 = np.poly1d(z_zero)
#Values of the fit line to represent in a plot.
x_trial=np.arange(-1,12,0.1)
fit1=p1(x_trial)

#Plot ratios of concentration versus integrated areas and annotate R2 and slope values.
fig = plt.figure()
ax = fig.add_subplot(111)
ax.annotate('R2 value is '+str(np.round(r2[0],3)), xy=(0., 8.8))
ax.annotate('Slope is '+str(np.round(newfit,3)), xy=(0., 7.8))
plt.title('Ethanol calibration curve')
plt.xlabel(' Ratio Area(H2O)/Area(EtOH)')
plt.ylabel('Ratio [H2O/EtOH] in drop')
plt.ylim(-1,10)
```

```
plt.xlim(-1,11)
plt.plot(ratioArea,ratioConc,'ro',x_trial,fit1,'r-')
plt.savefig("Ethanol calibration curve.svg",dpi=4000,format='svg')
plt.show()
```

Listing A.2: Code used to obtain a calibration curve to relate area to concentration ratios.

Now, we want to obtain a series of integrated area ratios for our droplets as they evolve over time. We have done so by using the code listed in Listing A.3

```
"""
Given an experimental data file, we decompose it into time and
    position spectra, obtaining the integrated areas for the water
    and ethanol peaks, and storing them properly
"""
import numpy as np
import matplotlib.pyplot as plt
from collections import OrderedDict
from scipy.integrate import simps
import os
from matplotlib import rcParams
rcParams.update({'figure.autolayout': True})

#Function that determines the area under the curve for two X
    intervals (x_int) using Simpson method. It determines the
    background region(int_), fit it to a 2 degree polynomial and
    substract it.
def INTEGRAte(x,y):
    int_bg_low = (x > 2000.0) & (x < 2600.0)
    int_bg_high = (x > 3750.0) & (x < 4000.0)
    x_bg = np.concatenate((x[int_bg_low],x[int_bg_high]))
    y_bg = np.concatenate((y[int_bg_low],y[int_bg_high]))
    z = np.polyfit(x_bg, y_bg, 2)
    p = np.poly1d(z)
    y_corrected=y-p(x)
    #One peak integral#
    x_int = (x > 2782.0) & (x < 3020.0)
    x_short=x[x_int]
    y_short=y_corrected[x_int]
    areaEtOH = simps(y_short,x_short)
    #Another peak integral#
    x_int = (x > 3089.0) & (x < 3800.0)
    x_short=x[x_int]
    y_short=y_corrected[x_int]
    areaH2O = simps(y_short,x_short)
```

```
31      return areaEtOH,areaH2O
32
33 #Open file and save the experimental data in data
34 dir_name='0p 3500m 1800s bath 333'
35 input_name = dir_name+'.txt'
36 os.makedirs((dir_name), exist_ok=True)
37 data=np.genfromtxt(input_name,delimiter=' ',skip_header=0)
38 raman_shift=data[0][2:] #cm-1 X range
39
40 #Create a list with the times and positions (to discern the pure
       from the mixed drop) of the experiments
41 times = list(OrderedDict.fromkeys([round(item[0]) for item in data
       [1:]]))
42 positions = list(OrderedDict.fromkeys([round(item[1]) for item in
       data[1:]]))
43 #d will be a dictionary with the spectra of each (time, position)
44 d = {}
45 #e will be a dictionary containing d, plus the integrated areas of
       the water and ethanol peaks obtained using INTEGRAte().
46 e = {}
47 #Filling the dictionaries.
48 for i in range(1,len(data)):
49      d[round(data[i][0]),round(data[i][1])] = data[i][2:]
50      e[round(data[i][0]),round(data[i][1])] = [data[i][2:],[],[]]
51 x = raman_shift[:]
52 for element in e:
53      e[element][1]=round(INTEGRAte(x,e[element][0])[0])
54      e[element][2]=round(INTEGRAte(x,e[element][0])[1])
55
56 #Initialize plots features and define where to store integral values
       for easy access.
57 integrales=['[Position] [Time Ethanol Water]']
58 #Empty lists to store values
59 etanol=[]
60 water=[]
61 #Create and save figures with the spectra for each time and position
       (droplet), saving the integrated area values.
62 plt.close()
63 for j in positions:
64      integrales.append([j])
65      for i in times:
66          integrales[-1].append([i,e[i,j][1],e[i,j][2]])
67          etanol.append(e[i,j][1])
68          water.append(e[i,j][2])
69          plt.ylabel('Intensities (a.u)')
```

```
70          plt.xlabel('Raman shift (cm-1')
71          plt.title('Time '+str(i)+' seconds. Position '+str(j))
72          plt.plot(raman_shift,d[i,j],'r-')
73          plt.show()
74          np.savetxt(dir_name+"/{}position{}time.txt".format('{:04.0f}
    '.format(j),
75                      '{:04.0f}'.format(i)),np.transpose([raman_shift,d
    [i,j]]),header='Raman_Shift Intensities')
76
77 #Save results to a file.
78 with open(dir_name+'/results.txt', 'w') as file_handler:
79      for item in integrales:
80          file_handler.write("{}\n".format(item))
81
82 #Empty lists to store values of the integrated areas for
    representation
83 pureetanol=[];mixedetanol=[]
84 purewater=[];mixedwater=[]
85 for i in range(1,len(times)+1):
86      purewater.append(integrales[1][i][2])
87      pureetanol.append(integrales[1][i][1])
88      mixedwater.append(integrales[2][i][2])
89      mixedetanol.append(integrales[2][i][1])
90
91 #Calculate the ratios of areas and save them in text files.
92 pureratio=np.asarray(purewater)/np.asarray(pureetanol)
93 mixedratio=np.asarray(mixedwater)/np.asarray(mixedetanol)
94 np.savetxt(dir_name+"/PureResults.txt",
95             np.transpose([times,pureetanol,purewater,pureratio]),
    header='Time Ethanol Water Ratio',fmt='%.f ' '%.f ' '%.f ' '%.2f
    ')
96 np.savetxt(dir_name+"/MixedResults.txt",
97             np.transpose([times,mixedetanol,mixedwater,mixedratio]),
    header='Time Ethanol Water Ratio',fmt='%.f ' '%.f ' '%.f ' '%.2f
    ')
98
99 #Obtain the time values in minutes, and represent the water and
    ethanol ratios for each drop in different plots, saving them.
100 timesmin=np.asarray(times)/60 #time in minutes, not seconds
101 plt.title('Pure drop')
102 plt.xlabel('Time (min)')
103 plt.ylabel('Ethanol Concentration')
104 plt.plot(timesmin,etanol[:len(timesmin)],'r-o',markersize=12)
105 plt.savefig(dir_name+"/Pure drop ethanol.svg",dpi=400,format='svg')
106 plt.show()
```

```
plt.xlabel('Time (min)')
plt.ylabel('Water Concentration')
plt.plot(timesmin,water[:len(timesmin)],'b-o',markersize=12)
plt.savefig(dir_name+"/Pure drop water.svg",dpi=400,format='svg')
plt.show()

plt.title('Mixed drop')
plt.xlabel('Time (min)')
plt.ylabel('Ethanol Concentration')
plt.plot(timesmin,etanol[len(timesmin):],'r-o',markersize=12)
plt.savefig(dir_name+"/Mixed drop ethanol.svg",dpi=400,format='svg')
plt.show()
plt.xlabel('Time (min)')
plt.ylabel('Water Concentration')
plt.plot(timesmin,water[len(timesmin):],'b-o',markersize=12)
plt.savefig(dir_name+"/Mixed drop water.svg",dpi=400,format='svg')
plt.show()
```

Listing A.3: Code employed to extract the ratio of integrated areas values from the experimental Raman spectrum.

To transform our ratio of areas obtained through the previous code to concentrations we use the code contained in the Listing A.4

```
"""
Given the calibration parameters set in z obtained from linear
    fitting the  calibration spectrum, we change those values to
    concentrations through waterfromratio(x) function.
Those values are then plot for each droplet versus time.
"""
import numpy as np
import matplotlib.pylab as plt

#Comes from two equations. W/OH=X. W+OH=100.
#Switches from ratio (x) to absolute value in % (H)
def waterfromratio(x):
    H=100*x/(x+1)
    print(H)
    return H
#Change ratio of areas to ratio of concentrations through  linear
    fit
#z(slope,intercept) obtained from calibration curve
z=np.asarray([.7511,0])
fit=np.poly1d(z)

#Input ratio for pure drop and mixed drop as the ratio of integrated
```

```
    peaks.
#Obtained from running Fit Back.py in calibration experiments.
pureRatio=np.asarray([ 1.22,0.92,0.76,0.67,0.61,0.56,0.51])
mixedRatio=np.asarray([ .13,.1,.11,.11,.11,.11,.11])
times=np.asarray([223,553,883,1212,1542,1872,2204])
times=times/60 #to obtain values in minutes

#Change from ratio of areas to ratio of concentrations through
    calibration fit
pureConc=fit(pureRatio)
mixedConc=fit(mixedRatio)
#Change from ratio of concentrations to concentrations in % (
    waterfromratio)
pureWaterConc=waterfromratio(pureConc)
mixedWaterConc=waterfromratio(mixedConc)
pureEthanolConc=100-pureWaterConc
mixedEthanolConc=100-mixedWaterConc

#Plot and save graphs for both droplets as Concentration vs time
    plots.
errtimes=0
plt.xlabel('Time (min)')
plt.ylabel('Concentration (%)')
#plt.axis([0,35,-15,115])
plt.title('Pure water droplet')
plt.errorbar(times, pureWaterConc,xerr=errtimes,label='Water',fmt='-
    bo')
plt.errorbar(times,pureEthanolConc,xerr=errtimes,fmt='-ro',label='
    Ethanol')
plt.legend()
plt.tight_layout(pad=0)
plt.savefig("Pure water drop.svg",dpi=4000,format='svg')
plt.show()

plt.xlabel('Time (min)')
plt.ylabel('Concentration (%)')
plt.title('Mixed droplet')
plt.errorbar(times, mixedWaterConc,xerr=errtimes,label='Water',fmt='
    -bo')
plt.errorbar(times,mixedEthanolConc,xerr=errtimes,fmt='-ro',label='
    Ethanol')
plt.legend()
plt.savefig("Mixed drop water.svg",dpi=4000,format='svg')
```

```
plt.show()
```

Listing A.4: Code that transforms the integrated area ratios to concentration values.

A.2 Scripts used to determine diffusion paths

We have first written a script that calculates more tie-line points (see Listing A.5, which will be needed later to produce a large number of possible diffusion paths.

```
"""
Program to obtain Hand constants and tie line compositions.
Input file structure is three columns with a name header for
    components.
Water-Ethanol-Toluene (first and last immiscible substances).
X,Y transform concentrations into the Cartesian coordinates.
U,V transform Cartesian in the Hand system coordinates.
c33,c22,c11 represent concentrations in U,V coordinates.
AL32,31 are natural logarithms of c33/c22 and c33/c11.
"""
#Import libraries
import numpy as np
import matplotlib.pyplot as plt
import ternary
from scipy import stats
#Setting the value for the range of the tie lines, ranging between 0
    to 1.
R=0.7

#Open file containing the ternary diagram and save its points in
    arrays.
input_name = 'inputs/MethanolData.txt'
data=np.genfromtxt(input_name,delimiter=' ',skip_header=1)
c1=b=data[:,0]/100#water
c3=a=data[:,1]/100#methanol
c2=c=data[:,2]/100#toluene

#Save data on a list(3,1), needed to represent it on a ternary
    diagram.
points = []
for i in range(data.shape[0]):
    points.append((data[i][0],data[i][1],data[i][2]))
points3=[]
```

```
points4=[]

#Reading left and right slope estimates.
LeftSlopeEstimate=np.sqrt(3)
RightSlopeEstimate=-np.sqrt(3)
#Calculating constants for coordinate conversions.
NP=c1.shape[0];NPM1=NP-1
XX=LeftSlopeEstimate-RightSlopeEstimate;XA=-2*c1[0]+1.-c3[0];YA=np.
    sqrt(3)*c3[0];XB=-2*c1[NP-1]+1.-c3[NP-1];YB=np.sqrt(3)*c3[NP-1]
#Related constants.
B3=(XA+XB)/2.;B6=(YA+YB)/2.;B1=B3-XA;B4=B6-YA;B2=(2.*B4-B1*(
    LeftSlopeEstimate+RightSlopeEstimate))/np.sqrt(3)/XX;B5=((B1+B2*
    np.sqrt(3))*LeftSlopeEstimate-B4)/np.sqrt(3);B7=B3*B5-B2*B6;B8=B1
    *B6-B3*B4;D=B2*B4-B1*B5

#Create lists to store conversions.
X=[];Y=[];U=[];V=[];C33=[];C22=[];C11=[];AL32=[];AL31=[];

#Converting to Hand coordinates and concentrations.
for i in range(1,NPM1):
    X.append(-2.*c1[i]+1.-c3[i])
    Y.append(np.sqrt(3)*c3[i])
    U.append((B2*Y[i-1]-B5*X[i-1]+B7)/D)
    V.append((B4*X[i-1]-B1*Y[i-1]+B8)/D)
    C33.append(V[i-1]/np.sqrt(3))
    C22.append(0.5*(1+U[i-1]-C33[i-1]))
    C11.append(1.-C22[i-1]-C33[i-1])
    #Calculating natural logarithms of concentration ratios.
    AL32.append(np.log(C33[i-1]/C22[i-1]))
    AL31.append(np.log(C33[i-1]/C11[i-1]))

#Make linear fit of the natural logarithms of concentrations,
    cleaning NaN values and plotting the fit.
AL32array=np.asarray(AL32)
AL31array=np.asarray(AL31)
mask = ~np.isnan(AL31array) & ~np.isnan(AL32array)
B, lnA, r_value, p_value, std_err = stats.linregress(AL31array[mask
    ],AL32array[mask])
A=np.exp(lnA)
plt.title('Linear fit to ln(Concentrations)')
plt.plot(AL31array[mask],AL32array[mask],'ro')

#Reading Q1(ln c3/c1 in Hand cooncentrations). Goes by pairs of
    points to form a tie-line.
Q1=np.array([1.,2,3,4])
```

```
Q1[0]=np.exp(AL31[2])
Q1[1]=np.exp(AL31[-3])
Q1[2]=np.exp(AL31[3])
Q1[3]=np.exp(AL31[-4])

#Calculating actual equilibrium concentrations from tie lines.
G=[];W11=[];W31=[];W12=[];W32=[];AQ31=[];AQ32=[];
W1=[];W3=[];X1=[];Y1=[];U1=[];V1=[];W21=[];
for i in range(0,4):
    G.append((1.+1./Q1[i]+1./A/np.real(np.power(Q1[i],B))))
    U1.append(1.-(1.+2./Q1[i])/G[i])
    V1.append(np.sqrt(3)/G[i])
    X1.append(B1*U1[i]+B2*V1[i]+B3)
    Y1.append(B4*U1[i]+B5*V1[i]+B6)
    W1.append(.5*(1.-X1[i]-Y1[i]/np.sqrt(3)))#water
    W3.append(1.-2.*W1[i]-X1[i])#ethanol
    AQ31.append(np.log(Q1[i]))
    AQ32.append(np.log(A)+B*AQ31[i])\

#Calculating Hand constant E and F and c3/1 at plait point.
F=(AQ32[1]-AQ32[3])/(AQ31[0]-AQ31[2]);E=np.exp(AQ32[1]-F*AQ31[0]);QP
    =np.exp(np.log(A/E)/(F-B))
G2=[];X2=[];Y2=[];U2=[];V2=[];Q2=[];Q3=[];G3=[];X3=[];Y3=[];U3=[];V3
    =[];

#Calculating equibrium composition for # tielines (change # at range
    )
for j in range(1,15):
    #Water-rich phase points
    Q2.append(R**(j-1)*QP)
    G2.append(1.+1./Q2[j-1]+1./A/Q2[j-1]**B)
    U2.append(1.-(1.+2./Q2[j-1])/G2[j-1])
    V2.append(np.sqrt(3)/G2[j-1])
    X2.append(B1*U2[j-1]+B2*V2[j-1]+B3)
    Y2.append(B4*U2[j-1]+B5*V2[j-1]+B6)
    W11.append(.5*(1.-X2[j-1]-Y2[j-1]/np.sqrt(3)))#water
    W31.append(1.-2.*W11[j-1]-X2[j-1])#ethanol

    #Oil-rich phase
    Q3.append(((E/A)*Q2[j-1]**F)**(1./B))
    G3.append(1.+1./Q3[j-1]+1./A/Q3[j-1]**B)
    U3.append(1.-(1.+2./Q3[j-1])/G3[j-1])
    V3.append(np.sqrt(3)/G3[j-1])
    X3.append(B1*U3[j-1]+B2*V3[j-1]+B3)
    Y3.append(B4*U3[j-1]+B5*V3[j-1]+B6)
```

```
110     W12.append(.5*(1.-X3[j-1]-Y3[j-1]/np.sqrt(3)))#water
111     W32.append(1.-2.*W12[j-1]-X3[j-1])#ethanol
112 
113 #Create the third component by difference from the other two
114 W2=[1-x - y for (x,y) in zip(W1,W3)] #toluene
115 W21=[1-x - y for (x,y) in zip(W11,W31)]
116 W22=[1-x - y for (x,y) in zip(W12,W32)]
117 
118 #Add concentrations as (Water, Ethanol, Toluene) to a list so that
    it can be represented on a ternary diagram.
119 for i in range(len(W31)):
120     points3.append((100*W11[i],100*W31[i],100*W21[i]))
121 for i in range(len(W32)):
122     points4.append((100*W12[i],100*W32[i],100*W22[i]))
123 
124 #Plot original ternary diagram and tie-lines
125 scale = 100
126 fontsize = 20
127 figure, tax = ternary.figure(scale=scale)
128 figure.set_size_inches(10, 10)
129 tax.boundary(linewidth=3.0)
130 tax.gridlines(multiple=25, color="black")
131 tax.ticks(axis='lbr', linewidth=1, multiple=25)
132 tax.clear_matplotlib_ticks()
133 tax.left_corner_label("Toluene",fontsize=fontsize)
134 tax.right_corner_label("Water",fontsize=fontsize)
135 tax.top_corner_label("Ethanol",fontsize=fontsize)
136 ax = tax.get_axes()
137 ax.axis('off')
138 tax.scatter(points, marker='.', color='blue', label="Original")
139 tax._redraw_labels()
140 tax.scatter(points3, marker='o', color='red', label="Water-rich
    phase")
141 tax.scatter(points4, marker='o', color='green', label="Oil-rich
    phase")
142 for i in range(len(points3)):
143     tax.line(points3[i],points4[i], linewidth=3., marker='', color='
    pink', linestyle=":")
144 tax.legend()
145 tax.show()
146 
147 #Renaming and keeping existing files
148 import os
149 i = 0
```

```
while os.path.exists('{}{:d}.jpeg'.format('Outputs/
    CalculatedTieLines', i)):
    i += 1
tax.savefig('{}{:d}{}{:.1f}.jpeg'.format('Outputs/CalculatedTieLine'
    ,i,'with R',R))
```

Listing A.5: Code used to produce tie-lines along a given ternary diagram.

The code in Listing A.6 calculates all the possible diffusion paths occurring when contacting our fixed bath composition (no water) with binary mixtures of alcohol-water.

```
"""
Given a fixed composition, this program calculates the possible
    diffusion paths when contacting the fixed composition with
    another composition laying in a edge.
NOMENCLATURE: W,E,T refers to Water, Ethanol and Toluene.
0 refers to one bulk phase, p0 to the other and s to subsurface (tie
    -lines)
We contact our bath solution(suffix 0) with a mixture of ethanol and
     water (suffix p0).
We determine alpha for a chosen tie-line given by [(wS,eS) and (wpS,
    epS)] using the App. E program.
"""
from scipy import optimize
import numpy as np
from math import erf,sqrt,exp,pi
import ternary
import App_E
import os

#Initial conditions when contacting phase (0,t0,me0) with (wp0,mep0
    ,0).
t0=0.7904;me0=0.2096;mep0=None;tp0=0;
#Using given ternary diagram contained in App_E program, we divide
    the tie-lines in two.
upperpoints=App_E.points[:6]
lowerpoints=App_E.points[6:]
lowerpoints.reverse()

#points contains the original input data, points3 is the water-rich
    phase (top right) and points4 the oil-rich phase (bottom left).
#We obtain the original+App_E created tie-lines for each phase.
tS=np.zeros(len(App_E.points3)+len(upperpoints));tpS=np.zeros(len(tS
    ))
meS=np.zeros(len(tS));mepS=np.zeros(len(tS))
```

```
for i in range(len(App_E.points3)):
    tS[i]=App_E.points3[i][2]/100
    meS[i]=App_E.points3[i][1]/100
    tpS[i]=App_E.points4[i][2]/100
    mepS[i]=App_E.points4[i][1]/100
for i in range(len(App_E.points3),len(App_E.points3)+len(upperpoints)):
    tS[i]=upperpoints[i-len(App_E.points3)][2]/100
    meS[i]=upperpoints[i-len(App_E.points3)][1]/100
    tpS[i]=lowerpoints[i-len(App_E.points3)][2]/100
    mepS[i]=lowerpoints[i-len(App_E.points3)][1]/100
t=[];me=[]
t.append(t0);t.append(tp0);t.append(tS);t.append(tpS)
me.append(me0);me.append(mep0);me.append(meS);me.append(mepS)

#Function to determine alpha from known concentrations.
def f(alpha):
    return ((1+erf(alpha))/(1-erf(alpha)))*(t0-tS*(1-alpha*sqrt(pi)*exp(alpha**2)\
            *(1-erf(alpha))) -tpS*(1+alpha*sqrt(pi)*exp(alpha**2)*(1+erf(alpha)))+tp0)

#Function to determine mep0 using alpha solutions previously obtained
def f2(mep0):
    return ((1+erf(alphasol))/(1-erf(alphasol)))*(me0-meS*(1-alphasol*sqrt(pi)*exp(alphasol**2)\
            *(1-erf(alphasol))) -mepS*(1+alphasol*sqrt(pi)*exp(alphasol**2)*(1+erf(alphasol)))+mep0)

#Create lists to store values and initial estimate for alpha (x0)
alphaRoot=np.zeros(len(t[3]))
mep0Root=np.zeros(len(me[3]))
x0=0.1

#Solve the functions for all the concentrations given in t
for i in range(len(t[3])):
    tS=t[2][i]
    tpS=t[3][i]
    alphasol = optimize.fsolve(f, x0)
    alphaRoot[i]=alphasol
    meS=me[2][i]
    mepS=me[3][i]
    mep0sol = optimize.fsolve(f2, x0)
    mep0Root[i]=mep0sol
```

```
65 #Calculate water solutions by difference because toluene
       compositions are zero.
66 watsol=1-mep0Root
67
68 #Add and transpose solutions.
69 saved_data=[]
70 saved_data.append(100*(1-t[2]-me[2]))
71 saved_data.append(100*me[2])
72 saved_data.append(100*t[2])
73
74 saved_data.append(100*(1-t[3]-me[3]))
75 saved_data.append(100*me[3])
76 saved_data.append(100*t[3])
77
78 saved_data.append(100*watsol)
79 saved_data.append(100*mep0Root)
80
81
82 saved_data=np.transpose(saved_data)
83 print ('Alpha values are',alphaRoot)
84 print ('mep0(Methanol) value is',mep0Root,'and water value is',
       watsol)
85
86 #Concentrations in %, format is (W,MeOH,T).
87 finalpoints = []
88 for i in range(mep0Root.shape[0]):
89         finalpoints.append((100*watsol[i],100*mep0Root[i],0))
90
91 #Plot the ternary diagram, same as in App_E.
92 scale = 100
93 fontsize = 20
94 figure, tax = ternary.figure(scale=scale)
95 figure.set_size_inches(10, 10)
96 tax.boundary(linewidth=3.0)
97 tax.gridlines(multiple=25, color="black")
98 tax.ticks(axis='lbr', linewidth=1, multiple=25)
99 tax.clear_matplotlib_ticks()
100 tax.left_corner_label("Toluene",fontsize=fontsize)
101 tax.right_corner_label("Water",fontsize=fontsize)
102 tax.top_corner_label("Methanol",fontsize=fontsize)
103 ax = tax.get_axes()
104 ax.axis('off')
105 tax.scatter(App_E.points, marker='o',color='blue', label="Original")
106 tax.scatter(App_E.points3, marker='o', color='b', label="Water-rich
       phase")
```

```
tax.scatter(App_E.points4, marker='o', color='b', label="Oil-rich
    phase")
#To determine the range of tie-lines you want to plot.
rang=(0,len(finalpoints))

#Adds tie-lines from App_E to new tie-lines obtained.
RightLobe=App_E.points3+upperpoints
LeftLobe=App_E.points4+lowerpoints

#Plot diffusion paths (green lines) and tie-lines (pink lines)
    connecting initial compositions (green dots)
for i in range(rang[0],rang[1]):
    #Condition to plot only real valued concentrations (between 0
    and 1)
    if(mep0Root[i]<=1 and mep0Root[i]>=0):
        tax.line(finalpoints[i],RightLobe[i], linewidth=3., marker='
    s', color='green', linestyle="-")
        tax.line(LeftLobe[i],(0,me0*100,t0*100), linewidth=3.,
    marker='s', color='green', linestyle="-")
        tax.line(LeftLobe[i],RightLobe[i], linewidth=3., marker='s',
     color='pink', linestyle=":")
        tax.show()

tax.legend()
tax._redraw_labels()
tax.show()
print('Drop composition is '+str(finalpoints[i]))
print('Bath composition is '+str((0,me0*100,t0*100)))
print('Left Tieline composition is '+str(LeftLobe[i]))
print('Right Tieline composition is '+str(RightLobe[i]))

#Output values in text files(Dataout) and save plots ()
i = 0
while os.path.exists('{}{:d}.jpeg'.format('Outputs/Plot', i)):
    i += 1
tax.savefig('{}{:d}.jpeg'.format('Outputs/Plot', i))
k = 0
while os.path.exists('{}{:d}.txt'.format('Outputs/DataOut', k)):
    k += 1
np.savetxt('{}{:d}.txt'.format('Outputs/DataOut', k),saved_data,fmt=
    '%.3f',delimiter='  ',header=\
'wS    MeS    tS    wpS    MepS    tpS    wp0    Mep0')
```

Listing A.6: Code able to calculate all the possible diffusion paths connecting a fixed oil-alcohol mixture with a binary water-alcohol solutions.

A.3 Script used to determine the fractal dimension

To calculate the fractal dimension plotted in Chapter 3, we have run the script contained in the Listing A.7 for our thresholded dewetting pattern images.

```
"""
Determine the fractal dimension of a 2D thresholded image using the
    box-counting method.
Adapted from https://gist.github.com/rougier/
    e5eafc276a4e54f516ed5559df4242c0.
"""
import numpy as np
import imageio
import matplotlib.pyplot as plt

#Method to count the number of boxes containing a part of the image.
def boxcount(Z, k):
    S = np.add.reduceat(
        np.add.reduceat(Z, np.arange(0, Z.shape[0], k), axis=0),
                            np.arange(0, Z.shape[1], k), axis=1)

    return len(np.where((S > 0) & (S < k*k))[0])

#Save the image as an array of values between 0-1 (they're divided
    by 256).
Z = imageio.imread("filename")/256.0
#Set threshold to convert image into a binary array, where True
    means white and False black values.
threshold=0.9
Z = (Z < threshold)

# Obtain the number of pixels in the smaller axis)
p = min(Z.shape)
#floor returns the down-rounded value. 1.2 = 1; 1.9=1:-0.1=-1.
#We get the greatest power of 2 less than or equal to the size of
    the image and extract the exponent
n = 2**np.floor(np.log(p)/np.log(2))
n = int(np.log(n)/np.log(2))
# Build successive box sizes (from 2**n down to 2**1), saving the
    size of each box
sizes = 2**np.arange(n, 1, -1)
# Fill the boxs starting from the biggest size
counts = []
for size in sizes:
```

```
34      counts.append(boxcount(Z, size))
35
36 #Plots inverse of sizes versus counts.
37 plt.title('Size versus counts)')
38 plt.plot(np.log((1/sizes)),np.log(counts),'ro')
39
40 #Linear fit of the successive log(sizes) versus log (counts)
41 coeffs = np.polyfit(np.log(sizes), np.log(counts), 1)
42 print("Fractal dimension is: ", -coeffs[0])
```

Listing A.7: Code used to determine the fractal dimension of a thresholded image.

Bibliography

[1] J. Otero, S. Meeker, and P. S. Clegg. Compositional ripening of particle-stabilized drops in a three-liquid system. *Soft matter*, 14(19):3783–3790, 2018.

[2] K. A. Rumble. *Mechanical Properties of Particle-Stabilised Liquid-Liquid Interfaces*. PhD thesis, The University of Edinburgh, Edinburgh, United Kingdom, 2017.

[3] W. F. Magie. *A source book in physics*. Harvard Univ. Press, 1969.

[4] A. Einstein. *Investigations on the Theory of the Brownian Movement*. Courier Corporation, 1956.

[5] N. L. Sitnikova, R. Sprik, G. Wegdam, and E. Eiser. Spontaneously formed trans-anethol/water/alcohol emulsions: mechanism of formation and stability. *Langmuir*, 21(16):7083–7089, 2005.

[6] Al. Kabalnov. Ostwald ripening and related phenomena. *Journal of Dispersion Science and Technology*, 22(1):1–12, 2001.

[7] A. Kabalnov, A. Pertzov, and E. Shchukin. Ostwald ripening in two-component disperse phase systems: application to emulsion stability. *Colloids and Surfaces*, 24(1):19–32, 1987.

[8] P. W. Voorhees. The theory of ostwald ripening. *Journal of Statistical Physics*, 38(1-2):231–252, 1985.

[9] L. Lindfors, P. Skantze, U. Skantze, M. Rasmusson, A. Zackrisson, and U. Olsson. Amorphous drug nanosuspensions. 1. Inhibition of ostwald ripening. *Langmuir*, 22(3):906–910, 2006.

[10] J. Weiss and D. J. McClements. Mass transport phenomena in emulsions containing surfactants. In *Encyclopedia of Surface and Colloid Science, Second Edition*, pages 3518–3536. 2006.

[11] B. Binks, J. Clint, P. Fletcher, S. Rippon, S. Lubetkin, and P. Mulqueen. Kinetics of swelling of oil-in-water emulsions. *Langmuir*, 14(19):5402–5411, 1998.

[12] B. Binks, P. Fletcher, and B. Holt. Compositional ripening of particle- and surfactant-stabilised emulsions: a comparison. *Physical Chemistry Chemical Physics*, 12:2219–2226, 2010.

[13] L. Bai and D. J. McClements. Extending emulsion functionality: Post-homogenization modification of droplet properties. *Processes*, 4(2):17, 2016.

[14] B. Buchannan. Dish soap on a q-tip drops the local surface tension of dyed milk. course on flow visualization at the University of Colorado, Boulder. `http://vimeo.com/65932908`, 2013. Online; accessed 14-January-2018.

[15] M. Grauzinyte, J. Forth, K. Rumble, and P. Clegg. Particle-stabilized water droplets that sprout millimeter-scale tubes. *Angewandte Chemie - International edition*, 54:1456–1460, 2015.

[16] R. Shimizu and H. Tanaka. A novel coarsening mechanism of droplets in immiscible fluid mixtures. *Nature communications*, 6:7407, 2015.

[17] B. P. Binks. Particles as surfactants – similarities and differences. *Current Opinion in Colloid & Interface Science*, 7(1):21–41, 2002.

[18] E. Herzig, K. White, A. Schofield, W. Poon, M. Cates, and P. Clegg. The bijel: a bicontinuous interfacially jammed emulsion gel. In *NSTI Nanotech 2008, Nanotechnol. Conf. Trade Show, Tech. Proc*, pages 657–660, 2008.

[19] M. Haase, K. Stebe, and D. Lee. Continuous fabrication of hierarchical and asymmetric bijel microparticles, fibers, and membranes by solvent transfer-induced phase separation (strips). *Advanced Materials*, 27(44):7065–7071, 2015.

[20] H. Stephen and T. Stephen. *Solubilities of Inorganic and Organic Compounds. Vol. 2: Ternary and Multicomponent Systems, Part II.* Pergamon, Oxford, 1964.

[21] K Shinoda and H Saito. The effect of temperature on the phase equilibria and the types of dispersions of the ternary system composed of water, cyclohexane, and nonionic surfactant. *Journal of Colloid and Interface Science*, 26(1):70–74, 1968.

[22] M. Lawrence and G. D. Rees. Microemulsion-based media as novel drug delivery systems. *Advanced drug delivery reviews*, 64:175–193, 2012.

[23] P. Walstra. *Encyclopedia of emulsion technology: Emulsion Stability*, volume 1. Marcel Decker Inc., 1983.

[24] F. Leal-Calderon, V. Schmitt, and J. Bibette. *Emulsion science: basic principles*. Springer Science & Business Media, 2007.

[25] J. C. López-Montilla, P. E. Herrera-Morales, S. Pandey, and D. Shah. Spontaneous emulsification: mechanisms, physicochemical aspects, modeling, and applications. *Journal of dispersion science and technology*, 23(1-3): 219–268, 2002.

[26] C. Solans, D. Morales, and M. Homs. Spontaneous emulsification. *Current Opinion in Colloid & Interface Science*, 22:88–93, 2016.

[27] S. Bochner de Araujo, M. Merola, D. Vlassopoulos, and G. G. Fuller. Droplet Coalescence and Spontaneous Emulsification in the Presence of Asphaltene Adsorption. *Langmuir*, 33(40):10501–10510, 2017.

[28] E. Rideal and J. Davies. Interfacial phenomena. *London: Academic Press*, 1963.

[29] G. Quincke. Ueber periodische ausbreitung an flüssigkeitsoberflächen und dadurch hervorgerufene bewegungserscheinungen. *Annalen der Physik*, 271 (12):580–642, 1888.

[30] J. Davies and D. Haydon. Spontaneous emulsification. In *2nd International Congress of Surface Activity I*, pages 417–418, 1957.

[31] G. Kaptay. On the negative surface tension of solutions and on spontaneous emulsification. *Langmuir*, 33(40):10550–10560, 2017.

[32] A.Z. Patashinski, R. Orlik, K. Paclawski, M. A. Ratner, and B. A. Grzybowski. The unstable and expanding interface between reacting liquids: theoretical interpretation of negative surface tension. *Soft Matter*, 8(5):1601–1608, 2012.

[33] M. Stackelberg, E. Klockner, and P. Mohrhauer. Spontane emulgierung infolge negativer grenzflächenspannung. *Colloid & Polymer Science*, 115 (1):53–66, 1949.

[34] J. T. Davies. Surface active substances. *Proc. Intern. Congr. 2nd Ed.*, 1: 426, 1957.

[35] M. Stackelberg, E. Klockner, and P. Mohrhauer. Spontane emulgierung infolge negativer grenzflächenspannung. *Colloid & Polymer Science*, 115 (1):53–66, 1949.

[36] R. Granek, R. C. Ball, and M. E. Cates. Dynamics of spontaneous emulsification. *Journal de Physique II*, 3(6):829–849, 1993.

[37] M.V. Ostrovskii, Barenbau. R. K., and A. A. Abramzon. Conditions for formation of an emulsion during mass transfer. *Colloid Journal-USSR*, 32 (4):472, 1970.

[38] C. A. Miller. Spontaneous emulsification produced by diffusion — a review. *Colloids and Surfaces*, 29(1):89–102, 1988.

[39] S. A. Vitale and J. L. Katz. Liquid droplet dispersions formed by homogeneous liquid-liquid nucleation: "the Ouzo effect". *Langmuir*, 19 (10):4105–4110, 2003.

[40] X. Zhang, Z. Lu, H. Tan, L. Bao, Y. He, C. Sun, and D. Lohse. Formation of surface nanodroplets under controlled flow conditions. *Proceedings of the National Academy of Sciences*, 112(30):9253–9257, 2015.

[41] Z. Lu, H. Xu, H. Zeng, and X. Zhang. Solvent effects on the formation of surface nanodroplets by solvent exchange. *Langmuir*, 31(44):12120–12125, 2015.

[42] Z. Lu, M. Schaarsberg, X. Zhu, L. Yeo, D. Lohse, and X. Zhang. Universal nanodroplet branches from confining the Ouzo effect. *Proceedings of the National Academy of Sciences*, 114(39):10332–10337, 2017.

[43] H. Gamsjäger, J. Lorimer, P. Scharlin, and D. Shaw. Glossary of terms related to solubility (IUPAC Recommendations 2008). *Pure and applied chemistry*, 80(2):233–276, 2008.

[44] H. Tan, C. Diddens, M. Versluis, H. Butt, D. Lohse, and X. Zhang. Self-wrapping of an ouzo drop induced by evaporation on a superamphiphobic surface. *Soft Matter*, 13(15):2749–2759, 2017.

[45] H. Tan, C. Diddens, P. Lv, J. Kuerten, X. Zhang, and D. Lohse. Evaporation-triggered microdroplet nucleation and the four life phases of an evaporating Ouzo drop. *Proceedings of the National Academy of Sciences*, 113(31):8642–8647, 2016.

[46] R. Deegan, O. Bakajin, T. Dupont, G. Huber, S. Nagel, and T. Witten. Capillary flow as the cause of ring stains from dried liquid drops. *Nature*, 389(6653):827, 1997.

[47] J. Stauber, S. K. Wilson, B. R. Duffy, and K. Sefiane. Evaporation of droplets on strongly hydrophobic substrates. *Langmuir*, 31(12):3653–3660, 2015.

[48] N. Shahidzadeh, D. Bonn, and J. Meunier. A new mechanism of spontaneous emulsification: Relation to surfactant properties. *Europhysics Letters*, 40(4):459, 1997.

[49] H. Kunieda, Y. Fukui, H. Uchiyama, and C. Solans. Spontaneous formation of highly concentrated water-in-oil emulsions (gel-emulsions). *Langmuir*, 12 (9):2136–2140, 1996.

[50] A. Forgiarini, J. Esquena, C. Gonzalez, and C. Solans. Formation of nano-emulsions by low-energy emulsification methods at constant temperature. *Langmuir*, 17(7):2076–2083, 2001.

[51] A. Forgiarini, J. Esquena, C. González, and C. Solans. Studies of the relation between phase behavior and emulsification methods with nanoemulsion formation. In *Trends in colloid and interface science XIV*, pages 36–39. Springer, 2000.

[52] R. Greiner and D. Evans. Spontaneous formation of a water-continuous emulsion from a w/o microemulsion. *Langmuir*, 6(12):1793–1796, 1990.

[53] J. McBain, T. Woo, et al. Spontaneous emulsification, and reactions overshooting equilibrium. *Proc. R. Soc. Lond. A*, 163(913):182–188, 1937.

[54] M. Rang, C. A. Miller, H. H. Hoffmann, and C. Thunig. Behavior of hydrocarbon/alcohol drops injected into dilute solutions of an amine oxide surfactant. *Industrial & engineering chemistry research*, 35(9):3233–3240, 1996.

[55] K. Ruschak and C. Miller. Spontaneous emulsification in ternary systems with mass transfer. *Industrial & Engineering Chemistry Fundamentals*, 11: 534–540, 1972.

[56] J. Kirkaldy and L. C. Brown. Diffusion behaviour in ternary, multiphase systems. *Canadian Metallurgical Quarterly*, 2(1):89–115, 1963.

[57] S. E. Friberg. Potential correlation between spontaneous emulsification and the plait point in the system water/benzene/ethanol: A phase diagram approach. In *Soft*, volume 2, pages 1–6. Scientific Research Publishing, 2013.

[58] A. Bozeya, A. Al-Bawab, S. E. Friberg, and C. A. Miller. Spontaneous emulsification and phase equilibria in the system water, ethanol, and benzene. *Journal of Dispersion Science and Technology*, 34(10):1429–1436, 2013.

[59] D. Carteau, D. Bassani, and I. Pianet. The "Ouzo effect": Following the spontaneous emulsification of trans-anethole in water by NMR. *Comptes Rendus Chimie*, 11(4-5):493–498, 2008.

[60] A. Tehrani-Bagha, A. Viladot, K. Holmberg, and L. Nordstierna. An Ouzo emulsion of toluene in water characterized by NMR diffusometry and static multiple light scattering. *Colloids and Surfaces A: Physicochemical and Engineering Aspects*, 494:81–86, 2016.

[61] R. Krishna. Serpentine diffusion trajectories and the Ouzo effect in partially miscible ternary liquid mixtures. *Physical Chemistry Chemical Physics*, 17 (41):27428–27436, 2015.

[62] M. J. Groves. Spontaneous emulsification. *Chemistry & Industry*, 12:417–423, 1978.

[63] M. J. Rosen. *Surfactants and interfacial phenomena*. Wiely, 1989.

[64] E. A. Simion, M. S. Starch, P.S. Witt, J. D. Woodford, and K. J. Edgett. Hand and body lotions. In *Textbook of Cosmetic Dermatology*, pages 309–316. Martin Dunitz, 1998.

[65] H. Batamer, C. Dicharry, J. Lachaise, and A. Graciaa. Formulation of model cutting-oil water emulsions using paraffinic oil and ionic/nonionic surfactant mixture. *Journal of dispersion science and technology*, 21(5): 571–588, 2000.

[66] E. O. Egbogah and R. A. Dawe. Spontaneous emulsification aspect of enhanced oil recovery. *Journal of Chemical Technology and Biotechnology*, 35(3):132–144, 1985.

[67] D. O. Shah. Introduction. In *Surface Phenomena in Enhanced Oil Recovery*, pages 1–12. Plenum Press, 1981.

[68] W. T. Minehan and G. L. Messing. Synthesis of spherical silica particles by spontaneous emulsification. *Colloids and surfaces*, 63(1-2):181–187, 1992.

[69] J. Aubry, F. Ganachaud, J. Cohen, and B. Cabane. Nanoprecipitation of polymethylmethacrylate by solvent shifting: 1. Boundaries. *Langmuir*, 25 (4):1970–1979, 2009.

[70] S. Nigam and S. Rutan. Principles and applications of solvatochromism. *Applied Spectroscopy*, 55(11):362A–370A, 2001.

[71] Kluth, J. Reichardt's dye solves in different solvents. `https://en.wikipedia.org/wiki/Reichardt%27s_dye#/media/File:Solvatochromismusbetain.jpg`, 2006. Online; accessed 16-October-2018.

[72] C. Reichardt. Empirical parameters of the polarity of solvents. *Angewandte Chemie International Edition in English*, 4(1):29–40, 1965.

[73] C. Reichardt. Solvatochromic dyes as solvent polarity indicators. *Chemical Reviews*, 94(8):2319–2358, 1994.

[74] B. Wahl, P. Van Roy, M. Larson, and E. Kampman. *Exploring fractals on the Macintosh*. Addison-Wesley Publishing Company, 1995.

[75] J. Rehmeyer. Fractals: Infinity, contained. *Discover Magazine*, (July/August Issue), 2018.

[76] Prokofiev. Minkowski–bouligand dimension. `https://en.wikipedia.org/wiki/Minkowski%E2%80%93Bouligand_dimension`, 2010. Online; accessed 16-October-2018.

[77] T. A. Witten Jr and L. M. Sander. Diffusion-limited aggregation, a kinetic critical phenomenon. *Physical review letters*, 47(19):1400, 1981.

[78] H. Kesten. Upper bounds for the growth rate of DLA. *Physica A: Statistical Mechanics and its Applications*, 168(1):529–535, 1990.

[79] T. C. Halsey. Diffusion-limited aggregation: a model for pattern formation. *Physics Today*, 53(11):36–41, 2000.

[80] H. Song, D. L Chen, and R. F. Ismagilov. Reactions in droplets in microfluidic channels. *Angewandte chemie international edition*, 45(44): 7336–7356, 2006.

[81] S. Lindström and H. Andersson-Svahn. Overview of single-cell analyses: microdevices and applications. *Lab on a Chip*, 10(24):3363–3372, 2010.

[82] Á. Marín, W. van Hoeve, P. García-Sánchez, L. Shui, Y. Xie, M. Fontelos, J. Eijkel, A. van den Berg, and D. Lohse. The microfluidic kelvin water dropper. *Lab on a Chip*, 13(23):4503–4506, 2013.

[83] N. Binh-Khiem, K. Matsumoto, and I. Shimoyama. Polymer thin film deposited on liquid for varifocal encapsulated liquid lenses. *Applied physics letters*, 93(12):124101, 2008.

[84] A. Ebrahimi, P. Dak, E. Salm, S. Dash, S. V. Garimella, R. Bashir, and M. A. Alam. Nanotextured superhydrophobic electrodes enable detection of attomolar-scale DNA concentration within a droplet by non-faradaic impedance spectroscopy. *Lab on a Chip*, 13(21):4248–4256, 2013.

[85] S. Lach, S. Yoon, and B. A. Grzybowski. Tactic, reactive, and functional droplets outside of equilibrium. *Chem. Soc. Rev.*, 45:4766–4796, 2016.

[86] P. G. Moerman, H. W. Moyses, E. B. van der Wee, D. G. Grier, A. van Blaaderen, W. K. Kegel, J. Groenewold, and J. Brujic. Solute-mediated interactions between active droplets. *Physical Review E*, 96:032607, 2017.

[87] K. A. Rumble, I. D. Stoev, D. J. French, A. Abou-Hassan, and P. S. Clegg. Sprouting Droplets Driven by Physical Effects Alone. *Langmuir*, 33(17): 4235 – 4241, 2017.

[88] Reade. Fumed silica powder (SiO2) information webpage. `https://www.reade.com/products/fumed-silica-powder-sio2`, 2018. Online; accessed 21-March-2018.

[89] D. Vella, P. Aussillous, and L. Mahadevan. Elasticity of an interfacial particle raft. *Europhysics Letters*, 68(2):212, 2004.

[90] D. Vella, H. Kim, P. Aussillous, and L. Mahadevan. Dynamics of surfactant-driven fracture of particle rafts. *Physical review letters*, 96(17):178301, 2006.

[91] C. Planchette, E. Lorenceau, and A. Biance. Rupture of granular rafts: effects of particle mobility and polydispersity. *Soft Matter*, 2018.

[92] E. Jambon-Puillet, C. Josserand, and S. Protière. Drops floating on granular rafts: a tool for liquid transport and delivery. *Langmuir*, 34(15): 4437–4444, 2018.

[93] K. A. White, A. B. Schofield, P. Wormald, J. W. Tavacoli, B. P. Binks, and P. S. Clegg. Inversion of particle-stabilized emulsions of partially miscible liquids by mild drying of modified silica particles. *Journal of colloid and interface science*, 359(1):126–135, 2011.

[94] A. Imhof, M. Megens, J. J Engelberts, D. T. N. De Lang, R. Sprik, and W. L. Vos. Spectroscopy of fluorescein (fitc) dyed colloidal silica spheres. *The Journal of Physical Chemistry B*, 103(9):1408–1415, 1999.

[95] Saint Petersburg State University. Raman spectrometer Horiba Jobin-Yvon LabRam HR800. http://laser.spbu.ru/en/equipment-eng/hr800-eng.html. Online; accessed 24-November-2018.

[96] J. Schindelin, I. Arganda-Carreras, E. Frise, V. Kaynig, M. Longair, T. Pietzsch, S. Preibisch, C. Rueden, S. Saalfeld, B. Schmid, et al. Fiji: an open-source platform for biological-image analysis. *Nature methods*, 9(7): 676–682, 2012.

[97] M. Zou, Y. Han, L. Qi, and Y. Chen. Fast and accurate measurement of diffusion coefficient by taylors dispersion analysis. *Chinese Science Bulletin*, 52(24):3325–3332, 2007.

[98] Y. Song, Z. Lu, H. Yang, S. Zhang, and X. Zhang. Dissolution of sessile microdroplets of electrolyte and graphene oxide solutions in an ouzo system. *Langmuir*, 32(40):10296–10304, 2016.

[99] H. Tanaka and T Araki. Surface effects on spinodal decomposition of incompressible binary fluid mixtures. *EPL (Europhysics Letters)*, 51(2): 154, 2000.

[100] J. H. Gouda and P. Joos. Application of longitudinal wave theory to describe interfacial instability. *Chemical Engineering Science*, 30(5-6):521–528, 1975.

[101] Surface tension values of some common test liquids for surface energy analysis. http://www.dataphysics.de/fileadmin/user_upload/pdf/DataPhysics_Surface_Tension_Energy.pdf. Online; accessed 01-August-2018.

[102] Wiki anton-paar for dynamic viscosities. https://wiki.anton-paar.com/en/tables/. Online; accessed 01-August-2018.

[103] H Tan. *Evaporation and dissolution of droplets in ternary systems*. PhD thesis, University of Twente, Enschede, The Netherlands, 2018.

[104] J. Thijssen and J. Vermant. Interfacial rheology of model particles at liquid interfaces and its relation to (bicontinuous) Pickering emulsions. *Journal of Physics: Condensed Matter*, 30(2):023002, 2017.

[105] C. Gu and L. Botto. Direct calculation of anisotropic surface stresses during deformation of a particle-covered drop. *Soft matter*, 12(3):705–716, 2016.

[106] T. N. Hunter, R. J. Pugh, G. V. Franks, and G. J. Jameson. The role of particles in stabilising foams and emulsions. *Advances in colloid and interface science*, 137(2):57–81, 2008.

[107] E. Vignati, R. Piazza, and T. P. Lockhart. Pickering emulsions: interfacial tension, colloidal layer morphology, and trapped-particle motion. *Langmuir*, 19(17):6650–6656, 2003.

[108] T. N. Hunter, E. J. Wanless, G. J. Jameson, and R. J. Pugh. Non-ionic surfactant interactions with hydrophobic nanoparticles: Impact on foam stability. *Colloids and Surfaces A: Physicochemical and Engineering Aspects*, 347(1-3):81–89, 2009.

[109] A. Drelich, F. Gomez, D. Clausse, and I. Pezron. Evolution of water-in-oil emulsions stabilized with solid particles: Influence of added emulsifier. *Colloids and Surfaces A: Physicochemical and Engineering Aspects*, 365(1-3):171–177, 2010.

[110] A. P. Kotula and S. L. Anna. Probing timescales for colloidal particle adsorption using slug bubbles in rectangular microchannels. *Soft Matter*, 8 (41):10759–10772, 2012.

[111] S. Levine, B. D. Bowen, and S. J. Partridge. Stabilization of emulsions by fine particles II. Capillary and van der Waals forces between particles. *Colloids and surfaces*, 38(2):345–364, 1989.

[112] S. Kutuzov, J. He, R. Tangirala, T. Emrick, T. P. Russell, and A. Böker. On the kinetics of nanoparticle self-assembly at liquid/liquid interfaces. *Physical Chemistry Chemical Physics*, 9(48):6351–6358, 2007.

[113] A. Stocco, W. Drenckhan, E. Rio, D. Langevin, and B. P. Binks. Particle-stabilised foams: an interfacial study. *Soft Matter*, 5(11):2215–2222, 2009.

[114] R. Aveyard, J. H. Clint, D. Nees, and V. N. Paunov. Compression and structure of monolayers of charged latex particles at air/water and octane/water interfaces. *Langmuir*, 16(4):1969–1979, 2000.

[115] E. Fleige, B. Ziem, M. Grabolle, R. Haag, and U. Resch-Genger. Aggregation phenomena of host and guest upon the loading of dendritic core-multishell nanoparticles with solvatochromic dyes. *Macromolecules*, 45(23):9452–9459, 2012.

[116] J. Thipperudrappa, H. R. Deepa, U. P. Raghavendra, S. M. Hanagodimath, and R. M. Melavanki. Effect of solvents, solvent mixture and silver nanoparticles on photophysical properties of a ketocyanine dye. *Luminescence*, 32(1):51–61, 2017.

[117] A. S. Klymchenko. Solvatochromic and fluorogenic dyes as environment-sensitive probes: design and biological applications. *Accounts of chemical research*, 50(2):366–375, 2017.

[118] S. Herminghaus, C. C. Maass, C. Krüger, S. Thutupalli, L. Goehring, and C. Bahr. Interfacial mechanisms in active emulsions. *Soft Matter*, 10(36): 7008–7022, 2014.

[119] W. Francis, C. Fay, L. Florea, and D. Diamond. Self-propelled chemotactic ionic liquid droplets. *Chemical Communications*, 51(12):2342–2344, 2015.

[120] M. M. Hanczyc, T. Toyota, T. Ikegami, N. Packard, and T. Sugawara. Fatty acid chemistry at the oil-water interface: self-propelled oil droplets. *Journal of the American Chemical Society*, 129(30):9386–9391, 2007.

[121] T. Toyota, N. Maru, M. M. Hanczyc, T. Ikegami, and T. Sugawara. Self-propelled oil droplets consuming "fuel" surfactant. *J. Am. Chem. Soc.*, 131 (14):5012–5013, 2009.

[122] I. Lagzi, S. Soh, P. J. Wesson, K. P. Browne, and B. A. Grzybowski. Maze solving by chemotactic droplets. *Journal of the American Chemical Society*, 132(4):1198–1199, 2010.

[123] K. Ichimura, S. Oh, and M. Nakagawa. Light-driven motion of liquids on a photoresponsive surface. *Science*, 288(5471):1624–1626, 2000.

[124] L. Florea, K. Wagner, P. Wagner, G. G. Wallace, F. Benito-Lopez, D. L. Officer, and D. Diamond. Photo-chemopropulsion–light-stimulated movement of microdroplets. *Advanced Materials*, 26(43):7339–7345, 2014.

[125] J. R. Dorvee, A. M. Derfus, S. N. Bhatia, and M. J. Sailor. Manipulation of liquid droplets using amphiphilic, magnetic one-dimensional photonic crystal chaperones. *Nature materials*, 3(12):896, 2004.

[126] E. Bormashenko, R. Pogreb, Y. Bormashenko, A. Musin, and T. Stein. New investigations on ferrofluidics: ferrofluidic marbles and magnetic-field-driven drops on superhydrophobic surfaces. *Langmuir*, 24(21):12119–12122, 2008.

[127] Y. Zhao, J. Fang, H. Wang, X. Wang, and T. Lin. Magnetic liquid marbles: manipulation of liquid droplets using highly hydrophobic Fe3O4 nanoparticles. *Advanced materials*, 22(6):707–710, 2010.

[128] R. W. Style, Y. Che, S. Park, B. M. Weon, J. H. Je, C. Hyland, G. K. German, M. P. Power, L. A. Wilen, J. S. Wettlaufer, et al. Patterning droplets with durotaxis. *Proceedings of the National Academy of Sciences*, 110(31):12541–12544, 2013.

[129] D. Quéré. Surface chemistry: Fakir droplets. *Nature materials*, 1(1):14, 2002.

[130] A. Biance, C. Clanet, and D. Quéré. Leidenfrost drops. *Physics of Fluids*, 15(6):1632–1637, 2003.

[131] P. Bachmann, P. Walde, P. Luisi, and J. Lang. Self-replicating reverse micelles and chemical autopoiesis. *Journal of the American Chemical Society*, 112(22):8200–8201, 1990.

[132] P. Walde, R. Wick, M. Fresta, A. Mangone, and P. Luisi. Autopoietic self-reproduction of fatty acid vesicles. *Journal of the American Chemical Society*, 116(26):11649–11654, 1994.

[133] M. M. Hanczyc, S. M. Fujikawa, and J. W. Szostak. Experimental models of primitive cellular compartments: encapsulation, growth, and division. *Science*, 302(5645):618–622, 2003.

[134] T. F. Zhu and J. W. Szostak. Coupled growth and division of model protocell membranes. *Journal of the American Chemical Society*, 131(15): 5705–5713, 2009.

[135] J. W. Taylor, J. Gutierrez, K. Yanev, L. Cronin, and T. Hinkley. Evolution of oil droplets in a chemorobotic platform. *Nature communications*, 5:5571, 2014.

[136] T. M. Letcher and P. M. Siswana. Liquid-liquid equilibria for mixtures of an alkanol + water + a methyl substituted benzene at 25 C. *Fluid phase equilibria*, 74:203–217, 1992.

[137] D. Hand. Dineric distribution. *The Journal of Physical Chemistry*, 34(9): 1961–2000, 1930.

[138] K. E. Bennett, C. Phelps, H. Davis, L.E. Scriven, et al. Microemulsion phase behavior observations, thermodynamic essentials, mathematical simulation. *Society of Petroleum Engineers Journal*, 21(06):747–762, 1981.

[139] K. H. Raney. *Studies of nonequilibrium behavior in surfactant systems using videomicroscopy and diffusion path analysis*. PhD thesis, Rice University, Houston, TX (USA), 1986.

[140] P. Joos. *Dynamic surface phenomena*. VSP, 1999.

[141] C. H. Giles and A. H. Soutar. Surface tension of ionised dye solutions. *Journal of the Society of Dyers and Colourists*, 87(9):301–304, 1971.

[142] A. B. Kharge, Y. Wu, and C. E. Perlman. Sulforhodamine B interacts with albumin to lower surface tension and protect against ventilation injury of flooded alveoli. *Journal of applied physiology*, 118(3):355–364, 2014.

[143] K. Namura, K. Nakajima, K. Kimura, and M. Suzuki. Microfluidic control on nanoplasmonic thin films using Marangoni effect. *Journal of Nanophotonics*, 10(3):033006, 2016.

[144] C. Buffone, A. Cecere, R. Savino, R. Rioboo, J. De Coninck, and S. Van Vaerenbergh. Onset of Marangoni convection in low viscosity silicon oil inside a heated capillary tube. *International journal of thermal sciences*, 84:158–163, 2014.

[145] J. Crank et al. *The mathematics of diffusion*. Oxford university press, 1979.

[146] A. B. Pawar, M. Caggioni, R. Ergun, R. W. Hartel, and P. T. Spicer. Arrested coalescence in Pickering emulsions. *Soft Matter*, 7(17):7710–7716, 2011.

[147] A. Schröder, J. Sprakel, K. Schroën, J. N. Spaen, and C. C. Berton-Carabin. Coalescence stability of Pickering emulsions produced with lipid particles: A microfluidic study. *Journal of Food Engineering*, 234:63–72, 2018.

[148] L. A. Chacon and J. C. Baret. Microfluidic angle of repose test for Pickering emulsions. *Journal of Physics D: Applied Physics*, 50(39):39LT04, 2017.

[149] A. J. Dzieciol and S. Mann. Designs for life: protocell models in the laboratory. *Chemical Society reviews*, 41(1):79–85, 2012.

[150] P. Luisi, F. Ferri, and P. Stano. Approaches to semi-synthetic minimal cells: a review. *Naturwissenschaften*, 93(1):1–13, 2006.

[151] S. Mann. Systems of creation: the emergence of life from nonliving matter. *Accounts of chemical research*, 45(12):2131–2141, 2012.

[152] M. Li, X. Huang, and S. Mann. Spontaneous growth and division in self-reproducing inorganic colloidosomes. *Small*, 10(16):3291–3298, 2014.

[153] Y. Song, T. Michaels, Q. Ma, Z. Liu, H. Yuan, S. Takayama, T. Knowles, and H. Shum. Budding-like division of all-aqueous emulsion droplets modulated by networks of protein nanofibrils. *Nature communications*, 9 (1):2110, 2018.

[154] P. G. Saffman and G. I. Taylor. The penetration of a fluid into a porous medium or Hele-Shaw cell containing a more viscous liquid. *Proc. R. Soc. Lond. A*, 245(1242):312–329, 1958.

[155] S. K. Thamida, P. V. Takhistov, and H. Chang. Fractal dewetting of a viscous adhesive film between separating parallel plates. *Physics of Fluids*, 13(8):2190–2200, 2001.

[156] J. Nase, D. Derks, and A. Lindner. Dynamic evolution of fingering patterns in a lifted Hele-Shaw cell. *Physics of Fluids*, 23(12):123101, 2011.

[157] P. Pelcé and A. Libchaber. *Dynamics of curved fronts*. Academic Press, 1988.

[158] B. Sandnes, E. G. Flekkøy, H. A. Knudsen, K. J. Måløy, and H. See. Patterns and flow in frictional fluid dynamics. *Nature communications*, 2:288, 2011.

[159] A. Bahadorimehr, M. Damghanian, and M. Burhanuddin Yeop. A static micromixer inspired from fractal-like natural flow systems. In *Advanced Materials Research*, volume 254, pages 25–28. Trans Tech Publications, 2011.

[160] D. Heymann, D. Pence, and V. Narayanan. Optimization of fractal-like branching microchannel heat sinks for single-phase flows. *International journal of thermal sciences*, 49(8):1383–1393, 2010.

[161] D. Pence. The simplicity of fractal-like flow networks for effective heat and mass transport. *Experimental Thermal and Fluid Science*, 34(4):474–486, 2010.

[162] D. Lim, Y. Kamotani, B. Cho, J. Mazumder, and S. Takayama. Fabrication of microfluidic mixers and artificial vasculatures using a high-brightness diode-pumped Nd:YAG laser direct write method. *Lab on a Chip*, 3(4): 318–323, 2003.

[163] T. ul Islam and P. S. Gandhi. Viscous fingering in multiport Hele Shaw cell for controlled shaping of fluids. *Scientific reports*, 7(1):16602, 2017.

[164] L. Paterson. Radial fingering in a Hele Shaw cell. *Journal of Fluid Mechanics*, 113:513–529, 1981.

[165] M. Kawaguchi, A. Shibata, K. Shimomoto, and T. Kato. Effect of geometry and anisotropy of a Hele-Shaw cell on viscous fingering of polymer solutions. *Physical Review E*, 58(1):785, 1998.

[166] F. Haudin, V. Brasiliense, J. Cartwright, F. Brau, and A. De Wit. Genericity of confined chemical garden patterns with regard to changes in the reactants. *Physical Chemistry Chemical Physics*, 17(19):12804–12811, 2015.

[167] L. Antl, J. W. Goodwin, R. D. Hill, R. H. Ottewill, S. M. Owens, S. Papworth, and J. A. Waters. The preparation of poly (methyl methacrylate) latices in non-aqueous media. *Colloids and Surfaces*, 17(1): 67–78, 1986.

[168] W. Poon. The physics of a model colloid–polymer mixture. *Journal of Physics: Condensed Matter*, 14(33):R859, 2002.

[169] S. M. Underwood, J. R. Taylor, and W. Van Megen. Sterically stabilized colloidal particles as model hard spheres. *Langmuir*, 10(10):3550–3554, 1994.

[170] S. S Velankar. A non-equilibrium state diagram for liquid/fluid/particle mixtures. *Soft Matter*, 11(43):8393–8403, 2015.

[171] S. J. Heidlebaugh, T. Domenech, S. V. Iasella, and S. S. Velankar. Aggregation and separation in ternary particle/oil/water systems with fully wettable particles. *Langmuir*, 30(1):63–74, 2014.

[172] P. Baggethun. Radial profile plot plugin webpage. `https://imagej.nih.gov/ij/plugins/radial-profile.html`. Online; accessed 07-November-2018.